Triplons in the excitonic Kitaev-Heisenberg model on the honeycomb lattice: condensation, interactions and topology

Von der Fakultät Mathematik und Physik der Universität Stuttgart
zur Erlangung der Würde eines Doktors der Naturwissenschaften
(Dr. rer. nat.) genehmigte Abhandlung

Vorgelegt von

Pavel S. Anisimov

aus Pereswet

Hauptberichter:	Prof. Dr. Maria Daghofer
Mitberichter:	Prof. Dr. Hans Peter Büchler
Vorsitzender:	Prof. Dr. Martin Dressel

Tag der mündlichen Prüfung: 26.02.2019

Universität Stuttgart
Institut für Funktionelle Materie und Quantentechnologien

2019

Inhaltsangabe

Diese Dissertation betrachtet Mott-Isolatoren vom Van-Vleck Typ, bei denen starke Spin-Bahn-Kopplung den nicht magnetischen $J = 0$ Zustand einer unvollständig besetzten d-Schale bevorzugt. Magnetismus tritt dann durch Singulett-Triplett Anregungen in Erscheinung (z.B. Verbindungen mit den Übergangsmetallen (ÜM) Ru^{4+}, Os^{4+} oder Ir^{5+} Ionen). Wir konzentrieren uns auf Materialien, bei denen die Aufspaltung der zwei tiefsten Energieniveaus mit der Superaustauschenergieskala $\sim 4t^2/U$ vergleichbar ist, was die Bose-Einstein-Kondensation von magnetischen Anregungen (Exzitonen) ermöglicht.

Wir betrachten ein Gitter, das aus Oktaedern mit gemeinsamen Kanten besteht (90° ÜM-O-ÜM Bindungsgeometrie), wobei die Übergangsmetalle in der Mitte der Oktaeder platziert und von sechs Sauerstoffatomen umgeben sind. Wir leiten effektive mikroskopische Theorie für die t_{2g}^4 Elektronenkonfiguration her, wobei wir sowohl durch Sauerstoff vermittelten Superaustausch, als auch direkten Austausch benachbarter d-Orbitale berücksichtigen. Im Rahmen eines Formalismus mit Bondoperatoren, führen wir eine Projektion auf den Niederenergieunterraum durch, der aus einem $J = 0$ Singulett und einem $J = 1$ Triplett besteht. Daraus resultiert eine effektive Theorie von Triplonen (bosonische Quasiteilchen mit hard-core Zwangsbedingung). In diesem Modell konkurrieren zwei Beiträge, eine Heisenbergwechselwirkung von Vektor-Triplonen und ein richtungsabhängiger Kitaev Term, was an das $J = 1/2$ Kitaev-Heisenberg Modell auf dem Sechseckgitter erinnert. Wir untersuchen das Modell sowohl klassisch als auch quantenmechanisch, analysieren die entsprechenden magnetischen Phasen und vergle-

ichen mit dem konventionellen Kitaev-Heisenberg Modell. Die maßgeblichen Unterschiede sind ein paramagnetischer Sektor (für dominante Spin-Bahn-Kopplung) und eine neue Phase im Parameterbereich der Kitaev Spinflüssigkeit, eine durch 'order-by-disorder' erzeugte Triplonflüssigkeit.

Darüber hinaus finden wir topologisch nicht triviale Anregungen in magnetischen Feldern. Trotz großer Freiheiten im Parameterraum scheint es kaum möglich, topologisch triviale Phasen zu produzieren, solange das Magnetfeld eine zur Ebene orthogonale Komponente besitzt. Des Weiteren treten die Chernzahlen der Bänder in einer Vielzahl von Kombinationen auf. Wir klassifizieren diese Vielfalt an 'topologische Phasen' für ausgezeichnete Parameterbereiche der Theorie. Der hier betrachtete Mechanismus für topologisch nicht triviale Bänder in Triplonsystemen scheint vielversprechender als der auf Dzyaloshinskii-Moriya-Wechselwirkung basierende Ansatz und könnte eine experimentelle Beobachtung von Triplonbänder mit Chernzahlen bis zu $C = 8$ ermöglichen.

Das Modell sollte auf Materialien wie Li_2RuO_3 oder Ag_3LiRuO_6 anwendbar sein, wobei der Transport von triplonischen Randzuständen durch die Messung der thermischen Hall-Leitfähigkeit nachgewiesen werden könnte.

Abstract

This work deals with Van Vleck-type d^4 Mott insulators, i.e. transition metal (TM) oxides with partially filled d shell, where strong spin-orbit coupling imposes a nonmagnetic ground state with total angular momentum $J = 0$. Magnetism is represented only by singlet-triplet excitations (e.g. compounds with Ru^{4+}, Os^{4+} or Ir^{5+} ions). We focus on such materials, where the splitting between two lowest energy levels is comparable to the superexchange energy scale $\sim 4t^2/U$, giving rise to the Bose-Einstein condensation of excitons and leading to a finite staggered magnetization.

We consider the edge-sharing octahedra lattice (90° TM-O-TM bonding geometry), where transition metal ions are placed into the octahedra centers and are surrounded by six oxygen atoms. We derive an effective microscopic theory for t_{2g}^4 electronic configuration, including both superexchange electron transport mediated by oxygens and direct overlap between two neighbouring d orbitals. In terms of the bond operator formalism we perform a projection onto the low-energy subspace spanned by a $J = 0$ singlet and a $J = 1$ triplet and thus get an effective theory expressed in triplons (hard-core boson quasiparticles). Within the resulting model on the honeycomb lattice, the Heisenberg vector-triplon interaction competes with the single-flavour bond-dependent Kitaev one, which is reminiscent of the $J = 1/2$ Kitaev-Heisenberg model. We study the model using both classical and quantum mechanical techniques, obtain its magnetic phase diagram and compare it to the conventional Kitaev-Heisenberg model. Main differences can be represented by a spin-orbit coupling dominated paramagnetic sector

and by a new order-by-disorder triplon liquid phase, observed in the Kitaev spin liquid parameter space.

In addition to the phase diagram, we find that in magnetic fields the model exhibits topologically nontrivial excitations. Despite the total parameter space being broad, it appears difficult to find topologically trivial triplon bands if the magnetic field has a finite out-of-plane component. Furthermore, Chern numbers acquired by the bands can take many values under parameter variation and arise in various combinations. They thus form a rich variety of 'topological phases', which we classify for particularly important regimes of the theory. The introduced mechanism inducing nontrivial topology in triplon systems appears to be more promising than the Dzyaloshinskii-Moriya-interaction based approach, and suggests a possible experimental observation of triplon bands with Chern numbers up to $C = 8$.

The model should be appropriate to compounds like Li_2RuO_3 or Ag_3LiRuO_6, where triplonic edge transport might then be evidenced by measuring the thermal Hall conductivity.

Contents

1 Introduction

Transition metal oxides are known to incarnate strongly correlated systems, where two principal interactions compete – delocalizing hoppings and the localizing Coulomb repulsion. If the latter dominates, metallic properties of the material vanish, it becomes a Mott insulator and exhibits intriguing properties [1–3]. In particular, in recent years Mott insulators with partially filled d shells got a lot of attention both from theorists [4–21] and experimentalists [22–34]. Indeed, the first possible realization of the Kitaev-model [35] was proposed for d^5 Mott insulators with a strong spin-orbit coupling [4]. Such materials are considered promising candidates for an experimental probing of Majorana fermions and Z_2 gauge fields, quantum spin-liquids, and can be potentially useful for topological quantum computing [35, 36].

In [4] one considers a d^5 system, where the spin-orbit coupling locally entangles spins and angular momenta. An effective Hamiltonian is given by a projection of a superexchange theory onto the low-energy subspace, spanned by an effective Kramers pseudospin doublet. Pseudospins inherit the orbital spacial dependencies and frustrations, thus resulting Hamiltonians possess a nontrivial structure and are lattice dependent. For 90° bonding geometry the isotropic part of the effective Hamiltonian exactly cancels and the Kitaev anisotropic interaction is defined by bond-directional character of orbitals.

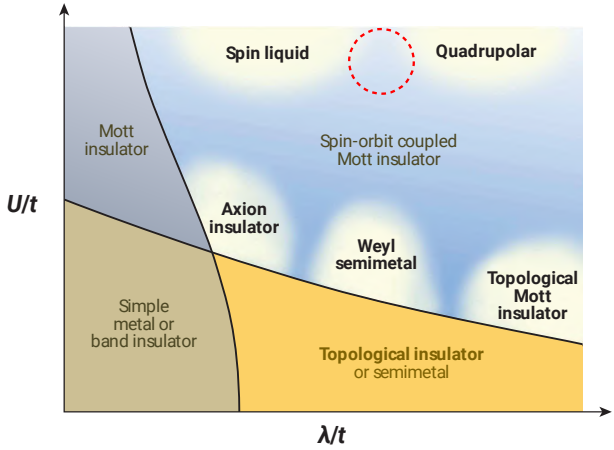

Figure 1.1.: (Taken from [52]) Figurative phase diagram for electronic materials expressed through Coulomb repulsion U and spin-orbit coupling λ. Red circle approximately indicates the region considered within the scope of this work.

Superexchange, considered together with the direct overlap of the d orbitals, provides a model applicable to iridium oxides A_2IrO_3, where Ir^{4+} ions form a honeycomb lattice. The resulting effective Hamiltonian determines a $J = 1/2$ Kitaev-Heisenberg model [5]. A compelling feature of this theory is a striking interplay between isotropic Heisenberg and bond-dependent Kitaev interactions. This model, with extensions, was widely used to describe materials like Na_2IrO_3, Li_2IrO_3 or α-$RuCl_3$ [37].

In contrast to d^5 models, magnetism in d^4 Mott insulators of Van-Vleck type (e.g. transition metal ions with t_{2g}^4 electronic configuration: Re^{3+}, Ru^{4+}, Os^{4+}, Ir^{5+}) is driven by the Bose-Einstein condensation of excitonic bosonic quasiparticles (triplons) [20, 21, 38], which is one the examples of exciton condensation in condensed matter physics [39–51].

The low-energy subspace of such systems is given by a nonmagnetic $J = 0$ singlet and a $J = 1$ triplet [20]. It turns out to be convenient to use a bond-operator formalism, originally developed for coupled dimers (on each spins form a singlet). The ground state singlet, triplet excitations and transitions between them are expressed in the language of hard-core triplons. The prefix 'hard-core' refers to a so-called hard-core constraint, which postulates that not more than one (out of three) excitation can be found on a given site. Projecting a corresponding superexchange Hamiltonian onto this subspace yields an effective theory. The triplons have gapped dispersions, however, since the spin-orbit coupling energy scale is comparable to (or greater than) that of superexchange $\sim 4t^2/U$, the gap can close yielding a finite staggered magnetisation [20]. Its length fluctuations represent a gapped amplitude Higgs mode, while the remaining two components become gapless Goldstone magnons [53].

Based on the superexchange Hamiltonians, this theory is strongly lattice dependent, thus two common bonding geometries are considered separately (see for example Fig. 3.3). The corner-sharing octahedra (180°-bonding geometry) applies to perovskites ABO_3 or A_2BO_4. The Higgs mode and its decay into two Goldstone modes at the antiferromagnetic ordering vector was experimentally observed in Ca_2RuO_4 [34].

However, the 90° case, which is applicable to a honeycomb lattice (e.g. Li_2RuO_3, Ag_3LiRuO_6), is a completely different story. The bond-directional interaction character of triplons tends to organize a set of three single-flavoured one-dimensional zigzag chains. The linear spin-wave studies of a Hamiltonian quadratic in triplons do not provide any reasonable answer about the order, since in the momentum space condensation is expected to happen along the edges of the First Brillouin zone.

Furthermore, topological effects in bosonic systems currently gain high interest, e.g. photons [54–60], phonons [61–63], magnons on py-

rochlore [64–66], kagome [67–76], honeycomb [77–87] lattices and the most relevant for this work – topologically nontrivial bands in triplonic systems [88–90].

A prominent example of realization of the triplon Hall effect was proposed for a frustrated quantum magnet $SrCu_2(BO_3)_2$ [88] described by a Shastry-Sutherland model [91]. This material has a gapped dimer-singlet ground state with triplet excitations. The authors included symmetry allowed small Dzyaloshinskii-Moriya anisotropic interactions [92, 93] and a small magnetic field perpendicular to the $SrCu_2(BO_3)_2$ plane. They found appropriate fields, which provide topological transitions of the bands with resulting Chern numbers $C = 0, \pm 2$. A further investigation with an arbitrary field direction revealed other topological characters of the bands $C = 0, \pm 1$ [89]. Neutron scattering data support topologically nontrivial bandstructures [90].

In contrast to electronic systems, triplon edge modes cannot be probed by doping. In the first case topological properties can be detected by integer quantum Hall measurements (the quantized transverse conductivity is evidenced if the Fermi level lies in the gap and signifies the presence of edge states) but triplons are electrically neutral and are not affected by any voltage. Therefore, for detecting edge modes in bosonic systems another approach is used. It is called thermal Hall effect [94]. One can show that magnon wave packets in Chern bands exhibit rotational motion [95]. Applying a thermal gradient populates the edge states differently, so the magnon rotational motion becomes unbalanced and yields a transversal current. This scheme turns out to be valid for triplons as well [88, 89].

In this thesis we consider d^4 Mott insulators of Van Vleck type with the 90° geometry. Similar to [5] we include the direct overlap between d orbitals. Reproducing calculations from [20] we develop a superexchange theory, project the corresponding Hamiltonian onto the low-energy subspace and obtain an effective theory in the bond operator

representation. We investigate magnetic properties of the system both classically and quantum mechanically and obtain magnetic phase diagrams. Additionally, we apply external magnetic fields and find out, whether topologically nontrivial excitations occur in the scope of d^4 Mott Insulators of Van-Vleck type.

2

Theoretical basis

In this Chapter we briefly review main concepts from atomic physics and use them discussing the crystal field splitting, the Hubbard model, Mott insulators and the Kitaev model.

2.1 Classification of single atom electronic states

We start with a free hydrogen atom, i.e. one electron in a central potential. Since the system is rotationally invariant, we introduce spherical coordinates and the time-independent Schrödinger equation reads as

$$H\Psi(r,\theta,\phi) = E\Psi(r,\theta,\phi), \qquad H = -\frac{\hbar^2}{2m}\nabla^2 - \frac{e^2}{r}. \tag{2.1}$$

We notice two conserved quantities in the system, namely the square of the orbital angular momentum and its projection onto the quantization axis (we choose the z direction), i.e.

$$[H, L^2] = 0, \qquad [H, L_z] = 0, \tag{2.2}$$

where

$$L_z = -i\hbar\partial_\phi, \qquad L^2 = -\hbar^2\Delta_{\theta\phi}, \tag{2.3}$$
$$\Delta = \frac{1}{r}\partial_r^2 r + \frac{1}{r^2}\Delta_{\theta\phi}, \qquad \Delta_{\theta\phi} = \frac{1}{\sin\theta}\partial_\theta\big(\sin\theta\partial_\theta\big) + \frac{1}{\sin^2\theta}\partial_\phi^2,$$
$$[L_i, L_j] = i\hbar\varepsilon_{ijk}L_k, \qquad [L^2, L_i] = 0.$$

The latter line means that we may find eigenvalues of only one $\mathbf{L}$ component and of its square at the same time. The eigenvectors and eigenvalues of these operators are

$$L_z = m\hbar, \qquad \Psi_m = \frac{1}{\sqrt{2\pi}}e^{im\phi}, \quad m \in \mathbb{Z}, \tag{2.4}$$

and

$$L^2 Y_{lm} = \hbar^2 l(l+1)Y_{lm}, \qquad Y_{lm}(\theta,\phi) = P_l^{(m)}(\cos\theta)e^{im\phi}, \tag{2.5}$$

with $l = 0, 1, 2, \ldots$ and $m = 0, \pm1, \pm2, \ldots, \pm l$. Furthermore, Y_{lm} are eigenfunctions of L_z with eigenvalues $m\hbar$. One calls l the *azimuthal* or *orbital quantum number* whereas m is called *magnetic quantum number*. Wave functions with different values of l are called *orbitals* and have a historical notation

l=	0	1	2	3	4
	s	p	d	f	g

The value $|Y_{lm}(\theta,\phi)|^2$ defines the angular distribution of electron density in the state with a given l and are axially-symmetric. Moreover, substituting $\mathbf{r} \to -\mathbf{r}$ or, in other words, $(r,\theta,\phi) \to (r,\pi-\theta,\phi+\pi)$ and using $Y_{l,m}(\pi-\theta,\phi+\pi) = (-1)^l Y_{lm}(\theta,\phi)$, one concludes that all states with an even (odd) value of l have the positive (negative) parity.

Another important property of the system is the *orbital degeneracy*. Since appropriate values for m are $m = 0, \pm1, \pm2, \ldots, \pm l$, there are $2l+1$

levels characterized by the same l (hence $(2l+1)$-fold degenerate). For example, in the case of a d-shell $l = 2$, which yields $2l + 1 = 5$-fold degeneracy.

The angular momentum operator is an analogue of the classical rotational momentum of a particle moving along its trajectory in the central field. Still, electrodynamics postulates that any such particle with a charge e possesses a magnetic moment

$$\boldsymbol{\mu} = \frac{j}{c}\boldsymbol{\Sigma}, \tag{2.6}$$

where $j = -e/T$ is a current, $T = 2\pi/\omega$ is a period and $\boldsymbol{\Sigma} = \pi r^2 \mathbf{n}$ is an infinitesimal oriented surface element. Using $\mathbf{L} = \mathbf{r} \times m\dot{\mathbf{r}}$ one obtains

$$\boldsymbol{\mu} = \frac{-e}{2mc}\mathbf{L}. \tag{2.7}$$

The same holds for quantum mechanics as well:

$$\mu_z = -\frac{e\hbar}{2mc}m_l, \qquad |\mu_l| = \mu_\mathrm{B}\sqrt{l(l+1)}, \tag{2.8}$$

where $\mu_\mathrm{B} = e\hbar/2mc$ is the Bohr magneton.

At first glance, we already have enough tools to describe magnetic properties of a single atom within the quantum paradigm. However, there is another contribution into the magnetic moment, first pointed out by Stern and Gerlach in 1922.

It is known that every particle with a magnetic moment $\boldsymbol{\mu}$ moving in a magnetic field $\mathbf{H}$ gets an energy shift $\Delta E = -\boldsymbol{\mu}\mathbf{H}$. Without loss of generality we set the field $\mathbf{H} = (0, 0, H)$ and hence the corresponding energy reads as $\Delta E = -\mu_z H = m_l \mu_\mathrm{B} H$, where $m_l = 0, \pm 1, \ldots, \pm l$. Thus, one expects the energy to be split into an odd number of components, but various experiments demonstrate that an even number takes place as well. This contradiction was resolved by means of an intrinsic angular momentum, called *spin*, and associated with it intrinsic magnetic momentum. An essential property of every quantum particle, it

may provide a quantum particle classification: those with an integer spin are called bosons, while those with a half-integer are fermions, e.g. electrons with $s = 1/2$. By analogy with L^2 one obtains

$$S^2 = \hbar^2 s(s+1) = \frac{3}{4}\hbar^2, \qquad S_z = m_s\hbar = \pm\frac{1}{2}\hbar^2, \tag{2.9}$$

where s is called *the spin quantum number* and $m_s = -s, -s+1, \ldots, s-1, s$ (for electrons $m_s = \pm 1/2$) are new quantum numbers. Analogously to (2.8) the corresponding magnetic moment reads as

$$\boldsymbol{\mu}_S = \frac{-e}{mc}\mathbf{S} \tag{2.10}$$

and the spin-associated energy splitting becomes $\Delta E = -\mu_{S_z} H = \pm\mu_{\mathrm{B}} H$.

Now we consider an atom and two non-interacting electrons with quantum numbers $|l_1, m_1\rangle$ and $|l_2, m_2\rangle$. A two-electron state can be described by

$$\psi(1,2) = \psi_{l_1,m_1}(1)\psi_{l_2,m_2}(2) \equiv |l_1, m_1\rangle|l_2, m_2\rangle, \tag{2.11}$$

where 1 and 2 represent sets of coordinates of the first and second particles correspondingly. In total there are $(2l_1 + 1)(2l_2 + 1)$ such states. We introduce the total angular momentum $\mathbf{L} = \mathbf{l}_1 + \mathbf{l}_2$, its projection onto the quantization axis $L_z = l_{1,z} + l_{2,z}$ and find some important commutation rules:

$$\begin{aligned} &[l_i^2, l_j^2] = [l_{i,z}, l_{j,z}] = [l_i^2, l_{j,z}] = 0, \qquad i,j = 1,2, \\ &[L^2, l_i^2] = 0, \qquad [L^2, l_{i,z}] \neq 0. \end{aligned} \tag{2.12}$$

Instead of $|l_1, m_1\rangle|l_2, m_2\rangle$ the two-electron system can be characterized by another equivalent quantum number set $|l_1, l_2, L, M_L\rangle$, where

M_L can be easily defined from

$$\begin{cases} L_z|l_1, l_2, L, M_L\rangle = \hbar M_L |l_1, l_2, L, M_L\rangle, \\ L_z|l_1, m_1\rangle|l_2, m_2\rangle = (l_{1,z} + l_{2,z})|l_1, m_1\rangle|l_2, m_2\rangle \end{cases} \tag{2.13}$$
$$\Rightarrow L_z|l_1, m_1\rangle|l_2, m_2\rangle = \hbar(m_1 + m_2)|l_1, m_1\rangle|l_2, m_2\rangle$$
$$\Rightarrow M_L = m_1 + m_2.$$

One can see that $L_{max} = l_1 + l_2$ and $L_{min} = |l_1 - l_2|$, hence $L_{min} < L < L_{max}$ with integer steps. Additionally

$$\sum_{L=|l_1-l_2|}^{l_1+l_2} (2L+1) = (2l_1+1)(2l_2+1). \tag{2.14}$$

In this manner one can introduce a so-called *total angular momentum* $\mathbf{j} = \mathbf{l} + \mathbf{s}$. In the absence of interactions between $\mathbf{l}$ and $\mathbf{s}$, the bases $|n, l, m_l, m_s\rangle$ and $|n, l, j, m_j\rangle$ are equivalent.

Filling of the atomic levels with the lowest energy has to fulfil the *Hund's rules*. The first rule postulates that for less-than-half-filled shells the electrons fill it with maximal possible spin, while for more-than-half-filled shells the total spin decreases (follows from the Pauli principle).

In order to discuss the second rule, we introduce another important effect originating from the presence of the spin degree of freedom, namely the relativistic interaction between the spin and angular magnetic moments. It is makes two spin directions (along the angular momentum and the opposite one) unequal and the difference is governed by the *spin-orbit coupling*. The spin-orbit coupling contribution for a single particle is given by

$$H_{\mathrm{SOC}} = \xi(r)\mathbf{ls}, \qquad \xi(r) = \frac{-e}{2mc}\frac{1}{r}\frac{\partial V(r)}{\partial r}, \tag{2.15}$$

where $V(r)$ is a central field potential.

Considering this operator as a perturbation for the main contribution of the Coulomb field yields the so-called *spin-orbit coupling constant*

$$\xi_{nl} = \frac{Ze^2\hbar^3}{2m^2c^2a_0^3}\int r^{-3}R_{nl}r^2dr = \frac{e^2\hbar^2}{2m^2c^2a_0^2}\frac{Z^4}{n^3l(l+1)(l+\frac{1}{2})}, \quad (2.16)$$

where a_0 is the Bohr radius, R_{nl} refers to the radial wave function and Z is the atomic number. We assume that $l \neq 0$ otherwise $H_{SOC} = 0$.

The Eq. (2.16) shows that the value of the spin-orbit coupling constant strongly depends on the atomic number Z, i.e. for heavy atoms (ions) the Hamiltonian H_{SOC} cannot be considered as a perturbation anymore. Consequently, the total wave function is not a product of the orbital wave function and the spin associated one.

A multi electron atomic wave function is characterized by the following set of quantum numbers: L - the total moment, $M = \sum_i m_i$, which may take $2L+1$ values from $-L, \ldots 0, \ldots, L$ and the same holds for the spin. The set of states with the same L and S (but with different M_L and M_S) is called the atomic *term symbol* and is labelled $S,\ P,\ D,\ F, \ldots$ according to ${}^{2S+1}L$ as for $L = 0, 1, 2, 3, \ldots$ correspondingly.

The spin-orbit coupling splits the terms into components described by the total orbital momentum $\mathbf{J} = \mathbf{L} + \mathbf{S}$ with quantum numbers $J = L+S,\ L+S-1, \ldots,\ |L-S|$. For not 'too heavy' atoms (the middle part of the periodic table) spin-orbit coupling weaker than the electron-electron interaction. This case is called the LS or *Russell-Saunders* scheme, in which one implies an interaction between the corresponding total angular momentum $\mathbf{L}$ (the sum of those of all electrons) and total spin $\mathbf{S}$. One can find the splitting energy values according to standard perturbation theory calculations, which in the LS- scheme read as

$$H_{\mathrm{SOC}} = \lambda \mathbf{LS} \quad (2.17)$$

where the spin-orbit coupling constant of an ion λ is given by a combination of radial integrals. This constant unlike ξ can be both negative

or positive and can be estimated by means of the following expressions:

$$J^2 = L^2 + S^2 + 2\mathbf{LS}, \qquad \text{where} \tag{2.18}$$
$$J^2 = J(J+1), \qquad L^2 = L(L+1), \qquad S^2 = S(S+1).$$

Then the splitting energy difference is

$$\Delta E_J = \frac{1}{2}\lambda\big(J(J+1) - L(L+1) - S(S+1)\big), \tag{2.19}$$
$$E_{J+1} - E_J = \lambda(J+1).$$

The last expression is called *Landé interval rule*. This difference allows measurement of λ[1]. For heavy ions its value grows drastically and in this case one follows the so called *jj-scheme*, which implies first summation of all the orbital and spin moments into total ones, and consequently the whole atom is described by a sum of all the total moments. Within the scope of this work we consider the *LS*-interaction, as it is applicable for many transition metals.

Therefore, we may formulate the second Hund's rule: for $\lambda > 0$ the lowest energy of less-than-half-filled shells corresponds to the smallest value of J and increases with it (regular multiplet), while for $\lambda < 0$ the lowest level is defined by the maximal J (inverted multiplet).

2.2 Transition metal ions in solids

Now we put a single transition metal ion in a solid. The ion does not possess a rotational symmetry anymore but obeys the local symmetry of the crystal [99, 100]. We consider an ion, surrounded by an O_6 octahedron of oxygen atoms (ligands), which is typical for many transition metal compounds. The first effect to be observed is the splitting of the

[1] Additionally, for rare-earth metals one can estimate $\lambda = 200(Z-55)$ cm^{-1} [98].

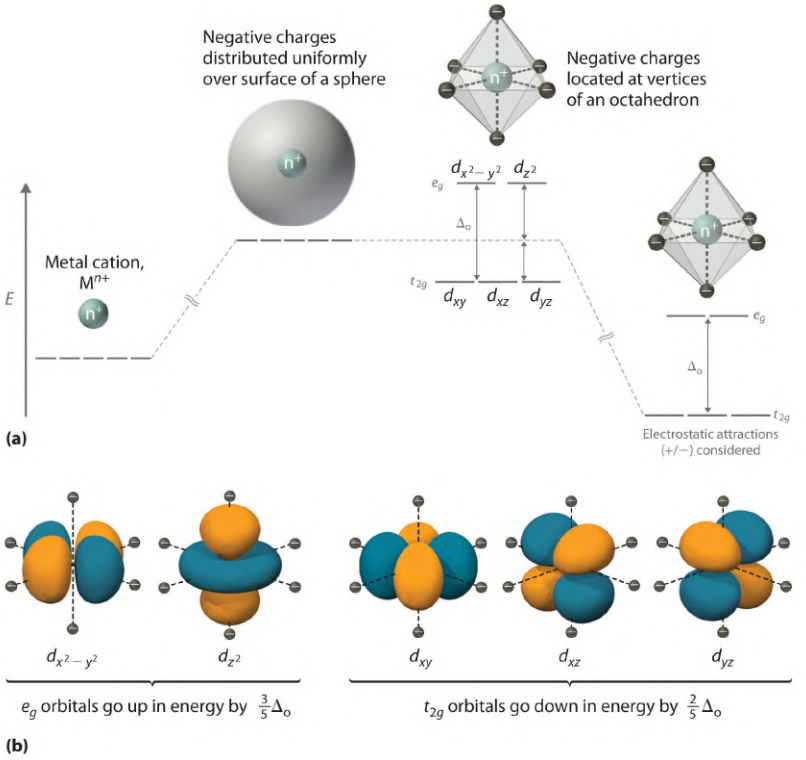

Figure 2.1.: (Taken from [99]) (a) Illustration of d-levels for different surrounding charge distributions. One can see that including the electrostatic attractive interactions does not affect the splitting but only shifts all d-levels down in energy. (b) e_g (t_{2g}) orbitals orientation with orbital lobes pointing towards (between) the ligands, increasing (decreasing) their energy relative to the original spherically symmetric case.

fivefold degenerate d-levels into two subsets: a lower threefold degenerate t_{2g} and an upper doublet e_g (see Fig. 2.1(a)). This phenomenon is called *crystal field splitting*. In general, such splittings are classified by the corresponding irreducible representations of the symmetry groups [101][2].

There are two processes behind this effect. First, the surrounding oxygens create the electric field and thus negatively charged ligands and d-orbitals repel. In Fig. 2.1(b) one can see that the d-levels (i.e. electron density distributions) have a specific spatial orientation and hence they do not interact with the ligand field equivalently, namely lobes of the e_g (t_{2g}) levels point towards (inbetween) the oxygens, which by means of the Coulomb repulsion increases (decreases) the energy of the orbitals. This contribution is called *point-charge contribution* [100].

The second process responsible for the splitting is a hybridization with the oxygen p-orbitals. That refers to a nonzero overlap of the ionic d and ligand p-orbitals. This covalency makes the d and p levels (lying much lower) mixed and repelled, and as a result shifts the corresponding d levels (see Section 2.4).

The resulting states can be expressed as (in the real basis) [100]

$$e_g \quad \begin{cases} |z^2\rangle \equiv |3z^2 - r^2\rangle = |l^z = 0\rangle \sim \frac{1}{2}(3z^2 - r^2) = \frac{1}{2}(2z^2 - x^2 - y^2), \\ |x^2 - y^2\rangle = \frac{1}{\sqrt{2}}(|2\rangle + |-2\rangle) \sim \frac{\sqrt{3}}{2}(x^2 - y^2), \end{cases}$$

$$t_{2g} \quad \begin{cases} |xy\rangle = -\frac{i}{\sqrt{2}}(|2\rangle - |-2\rangle) \sim \sqrt{3}xy, \\ |xz\rangle = -\frac{1}{\sqrt{2}}(|1\rangle - |-1\rangle) \sim \sqrt{3}xz, \\ |yz\rangle = \frac{i}{\sqrt{2}}(|1\rangle - |-1\rangle) \sim \sqrt{3}yz. \end{cases}$$

It is often convenient to map the t_{2g} triplet onto triplet states with

[2]Consequently the labels t_{2g} and e_g are originating from group theory: t stands for a triply degenerate representation of the O_h cubic point group, e for a doubly degenerate one, while g refers to the fact that the wave function is even under the spatial inversion.

an effective moment $\tilde{l} = 1$. Then the spin-orbit coupling takes the form [100]

$$H_{\mathrm{SO}}(t_{2g}) = \tilde{\lambda}\tilde{\mathbf{l}} \cdot \mathbf{S}, \tag{2.20}$$

where the new constant $\tilde{\lambda}$ is proportional to the original one. But it should be taken with the opposite sign [102], which changes the second Hund's rule for the t_{2g} levels to the opposite.

In Chapter 3 we consider the t_{2g}^5 system (one t_{2g} hole) with total degeneracy $(2\tilde{l}+1)(2S+1) = 6$. The spin-orbit coupling splits these levels into $\tilde{J} = \tilde{l} + S = 3/2$ quartet and $\tilde{J} = \tilde{l} - S = 1/2$ doublet, which lies lower and yields, in consonance with the so-called *Kramers theorem*, a Kramers degenerate ground state.

Kramers theorem. In the absence of a magnetic field (or a magnetic order in crystals) degeneracy of the energy levels of an atom (ion) with an odd number of electrons cannot be less than two. Thus, if the atomic (ionic) shells are filled with an odd number of electrons, the maximal possible multiplet splitting leads to a system with twofold degenerate energy levels or Kramers doublets.

2.3 Hubbard model and Mott insulators

The Hubbard model is the most prominent approach in studying of strongly-correlated electronic systems. In spite of its visual simplicity, it cannot be solved analytically in the general case. Following Ref. [103] we consider electrons in an ionic crystal with a periodic structure, where the lattice sites are static compared to the electrons. The one dimensional Hubbard model reads as

$$H = -t \sum_{\langle ij \rangle} c_{i\sigma}^{\dagger} c_{j\sigma} + U \sum_{i} n_{i\sigma} n_{i\sigma'}, \tag{2.21}$$

where $c^\dagger_{i\sigma}$, $c_{j\sigma}$, $n_{i\sigma}$ are electrons creation, annihilation and number operators at site i with spin σ, $\langle ij\rangle$ refers to nearest-neighbours pairs, t is the overlap integral, and U represents the Coulomb repulsion. Structurally it can be separated into two principal parts

$$\begin{aligned} H &= H_0 + UD, \\ H_0 &= -t\sum_{\langle ij\rangle} c^\dagger_{i,\sigma}c_{j,\sigma}, \qquad D = \sum_i n_{i,\sigma}n_{i,\sigma'}. \end{aligned} \tag{2.22}$$

We notice that these terms compete: H_0 tends to delocalize electrons, while D favours the localization. The Hamiltonian H_0 is diagonal in the Bloch basis $|\mathbf{k},\boldsymbol{\sigma}\rangle = c^\dagger_{k_N,\sigma_N}\dots c^\dagger_{k_1,\sigma_1}|\text{vac}\rangle$, where $\mathbf{k} = (k_1,\dots,k_N)$, $\boldsymbol{\sigma} = (\sigma_1,\dots,\sigma_N)$ and describes non-interacting electrons. The D-part is diagonal in the Wannier basis $|\mathbf{x},\boldsymbol{\sigma}\rangle = c^\dagger_{x_N,\sigma_N}\dots c^\dagger_{x_1,\sigma_1}|\text{vac}\rangle$, with $\mathbf{x} = (x_1,\dots,x_N)$ and counts the number of doubly occupied sites in the state $|\mathbf{x},\boldsymbol{\sigma}\rangle$. These two operators do not commute and thus the Hubbard Hamiltonian (2.21) can neither be diagonalized in the Wannier nor in the Bloch basis.

If $U = 0$, one is left with non-interacting electrons, i.e. $H = H_0$

$$H = -t\sum_{\langle ij\rangle} c^\dagger_{i,\sigma}c_{j,\sigma}. \tag{2.23}$$

By means of Fourier transformation

$$c_{i,\sigma} = \frac{1}{\sqrt{N}}\sum_{\mathbf{k}} e^{i\mathbf{k}\mathbf{x}_i}c_{\mathbf{k},\sigma}, \tag{2.24}$$

we get

$$H = \sum_{\mathbf{k},\sigma}\varepsilon(\mathbf{k}), \qquad \text{with} \qquad \varepsilon(\mathbf{k}) = -2t(\cos k_x + \cos k_y + \cos k_z). \tag{2.25}$$

A N-site lattice corresponds to N levels, which for $N\to\infty$ gives a continuum spectrum. If there is only one electron per site, the band

becomes half-filled and the crystal is metallic. These results do not depend on the lattice spacing, rather on the hopping constant t and on the number of the nearest-neighbours ζ yielding the bandwidth $W = 2\zeta t$ (in 1D $\zeta = 2$, in 2D $\zeta = 4$, etc.).

The opposite case $t \to 0$ is called the atomic limit and corresponds to a system with localized electrons. Considering the total Hamiltonian (2.21) we see that due to the on-site repulsion, creation of an electron-hole pair costs energy U. The only gain in energy occurs in the kinetic term, when the electron and the hole start moving in the crystal, and is equal to $W = 2\zeta t$. On the other hand, the energy loss is driven by the Coulomb repulsion U. Hence, if $U > W$, the electrons are not itinerant and the system remains insulating. Thus, for a half-filled system with rather small values of t (compared to U), the on-site repulsion makes the system insulating, despite the system seemingly being a conventional metal. Such insulators are called *Mott insulators* (or *Mott-Hubbard insulators*), which in contrast to the band insulators become insulating due to strong electron-electron interactions. Moreover, the localized electrons in Mott insulators lead to the presence of localized magnetic moments and spin and orbital degrees of freedom remain active.

In the limit $U \gg t$ in second order perturbation theory in t/U one obtains the *t-J Model*, which describes interesting physics of high-T_c superconductivity in cuprates [104]. Its derivation can be performed either by means of Hubbard X operators [105–107] or by introducing projectors onto the subspace comprising no doubly-occupied states [103]. We follow the latter scheme and define

$$P_0 = \prod_{i=1}^{N} (1 - n_{i,\downarrow} n_{i,\uparrow}), \tag{2.26}$$

where the corresponding index stands for zero doubly-occupied states.

The degenerate perturbation theory technique [103, 108] states that

$$H^{(2)} = P_0 T P_0 - \frac{1}{U} \sum_{m=1}^{N} \frac{P_0 T P_m T P_0}{m}, \tag{2.27}$$

where

$$P_m = \frac{(-1)^m}{m!} \frac{\partial^m}{\partial \alpha^m} \prod_{i=1}^{N} (1 - \alpha n_{i,\downarrow} n_{i,\uparrow})$$

projects onto the subspace with m double occupancies. The resulting Hamiltonian reads as [103]

$$H_{t-J} = \sum_{\substack{i,j=1 \\ i \neq j}}^{N} t_{ij} c_{i,\sigma}^{\dagger} c_{j,\sigma} (1 - n_i) + \sum_{\substack{i,j=1 \\ i \neq j}}^{N} \frac{2|t_{ij}|^2}{U} \Big(\mathbf{S}_i \mathbf{S}_j - \frac{n_i n_j}{4} \Big) \tag{2.28}$$

$$+ \frac{1}{U} \sum_{\substack{i,j,k=1 \\ i \neq j \neq k}}^{N} t_{ij} t_{jk} \Big(c_{i,\sigma}^{\dagger} \boldsymbol{\sigma}_{\sigma,\sigma'} c_{k,\sigma'} \mathbf{S}_j - \frac{1}{2} c_{i,\sigma}^{\dagger} c_{k,\sigma} n_j \Big) (1 - n_i)$$

with

$$\mathbf{S} = \frac{1}{2} \sum_{\sigma,\sigma'} c_{i,\sigma}^{\dagger} \boldsymbol{\sigma}_{\sigma,\sigma'} c_{i,\sigma'}, \tag{2.29}$$

where $\boldsymbol{\sigma}$ is the Pauli vector. Close to half-filling the three-site term becomes irrelevant. Introducing $J_{ij} \equiv 2|t_{ij}|^2/U$ we rewrite the t-J Hamiltonian

$$H_{t-J} = \sum_{\substack{i,j=1 \\ i \neq j}}^{N} t_{ij} c_{i,\sigma}^{\dagger} c_{j,\sigma} (1 - n_i) + \sum_{\substack{i,j=1 \\ i \neq j}}^{N} J_{ij} (\mathbf{S}_i \mathbf{S}_j - \frac{n_i n_j}{4}). \tag{2.30}$$

Setting $n_i = 1$, i.e. the half-filling case, we notice that the first term vanishes and we are left with

$$H_{\text{Heis}} = \sum_{\langle ij \rangle}^{N} J_{ij} \Big(\mathbf{S}_i \mathbf{S}_j - \frac{1}{4} \Big), \tag{2.31}$$

which is known as the *Heisenberg model*. It represents the exchange interactions between two neighbouring spins and its ground state is strongly dependent on the dimension of the system. In particular for $\mathrm{D} > 2$ the ground state is the long-range antiferromagnetic (AF) order, whereas for $\mathrm{D} = 1$ ($\mathrm{D} = 2$) this scenario is not possible at $T > 0$ ($T \geq 0$) [109].

One can keep the higher order corrections $\sim t^4/U^3$ and obtain a *biquadratic exchange* and a *four-spin-interaction* terms, given by

$$H_{4-\mathrm{spin}} = A_{ijkl}\Big\{(\mathbf{S}_i\mathbf{S}_j)(\mathbf{S}_k\mathbf{S}_l) + (\mathbf{S}_i\mathbf{S}_l)(\mathbf{S}_j\mathbf{S}_k) + (\mathbf{S}_i\mathbf{S}_k)(\mathbf{S}_j\mathbf{S}_l)\Big\}$$
$$H_{\mathrm{biq}} = B_{ij}(\mathbf{S}_i\mathbf{S}_j)^2,$$

which regarded together with (2.31) give rise to nontrivial physics (e.g. [110, 111]).

2.4 Orbital degrees of freedom

Orbitals define electron density distributions, which connects the material structure with its magnetic properties. If orbital degeneracy is lifted, some states (and hence associated with them orbital quantum numbers) become more favourable, which makes it possible to observe a long-range orbital pattern called *orbital ordering*. In the dense systems of magnetic ions the orbital degeneracy tends to be lifted and there are three conventional mechanisms for that – the dynamic Jahn-Teller effect, spin-orbital superexchange interaction and the spin-orbit coupling [3].

The first one is driven by the so-called *Jahn-Teller theorem* [112], which states: any non-linear molecular system in a degenerate electronic state (except Kramers degeneracy) will be unstable and will undergo distortion to form a system of lower symmetry and lower energy

thereby removing the degeneracy. Hence, systems with an even number of electrons have a singlet ground state.

The second scheme is represented by *superexchange interactions*. In contrast to the direct exchange, they imply a mediator, which could transfer electrons between two transition metal ions. This role in transition metal oxides is played by oxygens, i.e. anions, located between two ions (see Fig.3.3). In Mott insulators a corresponding effective hopping is defined by the energy difference between the involved oxygen p and ionic d orbitals and reads as $t = t_{pd}^2/\Delta_{\mathrm{CT}}$ [100], where Δ_{CT} is the so-called *charge transfer gap*.

As we mentioned above, orbitals are spacial distributions and their interactions are strongly dependent on their relative orientation, i.e. on the lattice geometry, which should be explicitly specified (e.g. in this thesis we consider two types of TM-O-TM bonding geometries, see Fig.3.3).

If superexchange dominates, one gets a group of Kugel-Khomskii-like theories [113–115]. These Hamiltonians can be obtained in the second order perturbation theory and in general they are of the form [3, 116]

$$H^{(\gamma)} = -\sum_n \frac{t^2}{\varepsilon_n} \sum_{\langle ij\rangle\gamma} \Pi_{ij}(\mathcal{S})\mathcal{O}_{ij}^{(\gamma)}, \tag{2.32}$$

where ε_n is the n^{th} virtual process excitation energy and $\Pi_{ij}(\mathcal{S})$ ($\mathcal{O}_{ij}^{(\gamma)}$) is the spin (orbital) projection operator. Such Hamiltonians are material dependent and require a detailed analysis of the virtual processes occur, calculation of the corresponding excitation energies, etc. For example, the prominent Kugel-Khomskii model for $KCuF_3$ [113] describes a system, where Cu^{2+} has a d^9 electronic configuration, while charge excitations are given by $d_i^9 d_j^9 \rightleftharpoons d_i^{10} d_j^8$. The t_{2g} levels are filled, while two-fold degenerate e_g orbitals remain active and analogous to spins can be associated with $\tau = 1/2$ pseudospin. The corresponding

Hamiltonian (2.32) then reads as [116]

$$H^{(\gamma)} = \sum_{\langle ij\rangle\gamma} \Big\{ -\frac{t^2}{U-3J_{\mathrm{H}}}\Big(\mathbf{S}_i\mathbf{S}_j + \frac{3}{4}\Big)\mathcal{P}_{ij}^{(\gamma)} + \frac{t^2}{U-J_{\mathrm{H}}}\Big(\mathbf{S}_i\mathbf{S}_j - \frac{1}{4}\Big)\mathcal{P}_{ij}^{(\gamma)} + \Big(\frac{t^2}{U-J_{\mathrm{H}}} + \frac{t^2}{U+J_{\mathrm{H}}}\Big)\Big(\mathbf{S}_i\mathbf{S}_j - \frac{1}{4}\Big)\mathcal{O}_{ij}^{(\gamma)} \Big\} + E_z \sum_i \tau_i^c, \quad (2.33)$$

with

$$\mathcal{P}_{ij}^{(\gamma)} \equiv \Big(\frac{1}{2} + \tau_i^{(\gamma)}\Big)\Big(\frac{1}{2} - \tau_j^{(\gamma)}\Big) + \Big(\frac{1}{2} - \tau_i^{(\gamma)}\Big)\Big(\frac{1}{2} + \tau_j^{(\gamma)}\Big), \quad (2.34)$$
$$\mathcal{O}_{ij}^{(\gamma)} \equiv 2\Big(\frac{1}{2} + \tau_i^{(\gamma)}\Big)\Big(\frac{1}{2} + \tau_j^{(\gamma)}\Big),$$

where E_z is the crystal field splitting of e_g orbitals.

The most relevant scenario for this work is the spin-orbit coupling being comparable to or larger than the superexchange energy scale. The spin and orbital degrees of freedom become locally entangled, which can be included within ionic multiplets of an effective pseudospin J [117, 118][3].

Generally, the low-energy magnetic interactions can be described by effective Hamiltonians, obtained by projecting the corresponding superexchange Hamiltonians onto the low-energy subspace. This subspace is usually spanned by the lowest $2J+1$ multiplet (e.g. in Chapter 3 this multiplet is a twofold Kramers degenerate $J = 1/2$ doublet). However, via the spin-orbit coupling the new pseudospin degree of freedom inherits the bond-directional structure and frustrations of the orbital interactions, which provides the resulting Hamiltonians a nontrivial structure. Moreover, any pseudospin ordering involves both **S**- and **L**-orderings.

The main principles, remarkable features and modern tendencies or effects governed by the orbital degrees of freedom can be found in reviews [3, 113, 116, 119, 120].

[3] In literature the term *isospin* is used as well. It should not be confused with the orbital pseudospin τ.

2.5 Kitaev model

It is known that at low temperatures solids with localized electrons exhibit spin ordering, which allows them to minimize their energy. Still, there are states of matter, called spin liquids, where spins do not order down to $T = 0\,\mathrm{K}$ but remain fluctuating [121]. If these fluctuations are of the thermal origin, the spin liquid is called *classical spin liquid*, whereas quantum spin liquids are highly entangled and are influenced by quantum fluctuations (see for example Review [122]). Quantum spin liquids imply no broken symmetries and hence are not predicted by the Landau-Ginzburg theory.

Quantum spin liquids are usually associated with valence bond solids [123, 124] or with the model of $SU(2)$ spins with a bond-dependent interaction character proposed by Kitaev [35]. The Hamiltonian of the *Kitaev model* on the honeycomb lattice reads as[4]

$$H_{\mathrm{Kitaev}} = -K_x \sum_{\langle ij\rangle a} S_i^x S_j^x - K_y \sum_{\langle ij\rangle b} S_i^y S_j^y - K_z \sum_{\langle ij\rangle c} S_i^z S_j^z, \qquad (2.35)$$

where $\gamma = a, b, c$ refers to a given bond (see Fig. 2.2). The ground state of this model is exactly solvable in terms of Majorana fermions[5] [126] and Z_2 gauge field degrees of freedom. It is represented either by a gapless or a gapped spin liquid (see Fig. 2.2(c)).

An experimental realization of this model could be of paramount importance, since the Kitaev model is argued to have possible applications in the field of topological quantum computing [35, 36]. Furthermore, apart from the quantum spin liquid states, with help of such materials one could experimentally probe Majorana fermions and the Z_2 gauge

[4] Caused by the directional charater of orbitals, a model with pseudospin Ising-like anysotropic exchange was proposed in [113], which is known today as *compass model* [125].

[5] These the fermions are their own antiparticles.

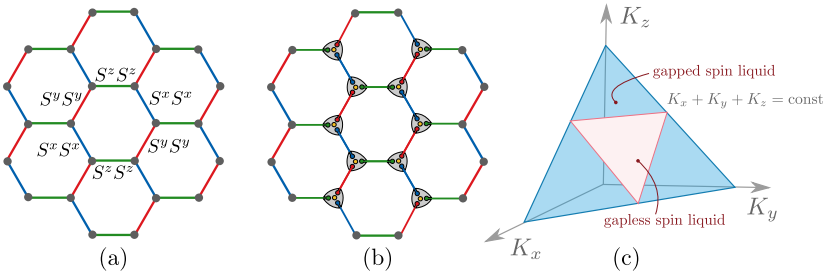

Figure 2.2.: (Reproduced from [127]) (a) A honeycomb lattice with bond-dependent spin interactions. Three inequivalent bond flavours are highlighted with colours. (b) The same lattice, reflecting Majorana fermions representation of spins (each Majorana is labelled with coloured circles). (c) Phase diagram of the Kitaev model. If any $K_{x/y/z}$ coupling dominates, a gapped spin-liquid is formed. The parameter space given by the red-shaded triangle corresponds to a gapless spin liquid, also known as *Majorana metal*.

fields driven physics. Luckily, there are possible candidates for realization of the Kitaev model [4]. We discuss it in more detail in the next Chapter.

3

Mott insulators in presence of the strong spin-orbit coupling

In this chapter we consider Mott insulators with the strong spin-orbit coupling, i.e. spin-orbit entangled $J = 1/2$ Mott insulators. We introduce the spin-1/2 *Kitaev-Heisenberg* model [5–19], discuss its principal properties and phase diagram. Supported by various experimental investigations [25–33] this theory represents a minimal adequate model for describing honeycomb iridates or ruthenates, e.g. Na_2IrO_3, Li_2IrO_3 or α-$RuCl_3$.

Then we focus on $J = 1$ Van-Vleck type ions and provide a short overview of the excitonic magnetism in such crystals [20, 21]. Finally, we derive an excitonic Kitaev-Heisenberg model.

3.1 Kitaev and Kitaev-Heisenberg models in Mott insulators

High values of SOC constant λ are typical for late TM ions, like Ru^{4+} ($\lambda \sim 84$meV), Os^{4+} ($\lambda \sim 186$meV) or Ir^{4+} ($\lambda \sim 380$meV) [97], which exceeds the t_{2g} intersite interactions. Therefore, as we discussed above, we expect the total angular momentum to be formed locally. Here we

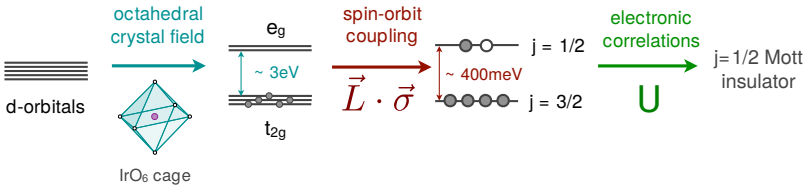

Figure 3.1.: (Taken from [127]). The general scheme illustrating formation of a $J = 1/2$ Mott insulator, where spin and angular momentum are locally entangled into pseudospin doublets.

provide the original derivation of a superexchange theory for a single hole in a threefold degenerate t_{2g} level (a low spin d^5 configuration) in a strong octaheral field, performed in [4]. Furthermore, we demonstrate that in such systems at low energies one can obtain compass-like Hamiltonians, which can serve as a possible material realization of the Kitaev model [4].

We consider a single hole on the d_{xy}, d_{xz} and d_{yz} orbitals and introduce the effective angular momentum $\tilde{l} = 1$ (see Eq. (2.20)):

$$|l_z = 0\rangle \equiv |d_{xy}\rangle, \qquad |l_z = \pm 1\rangle = -\frac{1}{\sqrt{2}}(i|d_{xz}\rangle \pm |d_{yz}\rangle). \tag{3.1}$$

The total magnetic moment reads as $\mathbf{M} = 2\mathbf{s} - \mathbf{l}$, where $\mathbf{s}$ refers to a hole spin operator. We include a tetragonal splitting $\Delta > 0$ of t_{2g} orbitals, which elongates octahedrons along the z-axis. The single ion Hamiltonian on the site i reads as

$$H_i^0 = \lambda \mathbf{l}_i \mathbf{s}_i + \Delta l_{z,i}^2. \tag{3.2}$$

Its ground state is given by a Kramers pseudospin doublet

$$|\tilde{\uparrow}\rangle = \sin\theta|0,\uparrow\rangle - \cos\theta|+1,\downarrow\rangle, \tag{3.3}$$
$$|\tilde{\downarrow}\rangle = \sin\theta|0,\downarrow\rangle - \cos\theta|-1,\uparrow\rangle, \qquad \text{with} \qquad \tan 2\theta = \frac{2\sqrt{2}\lambda}{\lambda - 2\Delta}.$$

The structure of the doublet leads to a nontrivial real space distribution (see Fig. 3.2) forming the bond geometry dependence of the exchange Hamiltonian.

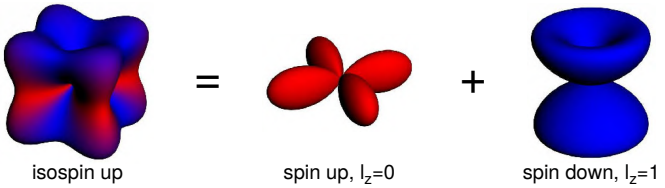

Figure 3.2.: (Taken from [4]) Hole density cartoon in the pseudospin up state, which is a superposition of a spin up in $|xy\rangle$ orbital (i.e. $|l_z = 0,\uparrow\rangle$) and a spin down in $(|yz\rangle + i|xz\rangle)$ with $\Delta = 0$.

There are two principal TM-O-TM bonding geometries (see Figs. 3.3 (a),(b)): a 180°-bond (corner-sharing octahedra) and a 90° one (edge-shared geometry). In order to get the effective theory, one projects the corresponding exchange models onto the pseudospin subspace (3.3). For 180° we have [4]

$$H_{ij}^{180^\circ} = J_1 \mathbf{S}_i \mathbf{S}_j + J_2 (\mathbf{S}_i \mathbf{r}_{ij})(\mathbf{r}_{ij} \mathbf{S}_j), \tag{3.4}$$

where $\mathbf{S}$ is the $S = 1/2$ pseudospin operator, $\mathbf{r}_{ij}$ is the unit vector along a given bond and $J_1 = 4/9$ and $J_2 = 2\eta/9U$ if $\eta = J_H/U$ is small . This means that we obtain an isotropic Heisenberg-like Hamiltonian (2.31) with a negligibly small dipolar-like anisotropy interaction.

In the 90°- case the isotropic part of the Hamiltonian exactly vanishes and, as a result, the exchange interaction depends on the orientation. Thus, we are left with

$$H_{ij}^{\gamma,90^\circ} = -JS_i^\gamma S_j^\gamma \tag{3.5}$$

where γ refers to a bond. This is precisely the compass-model Hamiltonian [113] with only one certain spin (pseudospin) component active on the given bond. Figs. 3.3(c),(d) display two possible lattices for the ABO_2 and A_2BO_3 structures (with alkali A and a transition metal B). The second one coincides with the Kitaev model on the honeycomb lattice with the spin-liquid ground state.

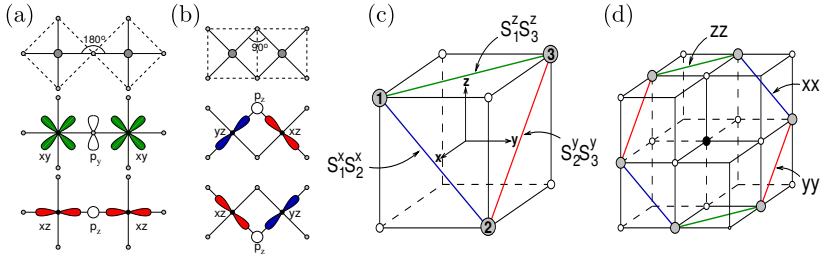

Figure 3.3.: (Taken from [4]) Two principal bonding geometries: (a) the 180° corner-sharing octahedra and (b) the 90° edge-sharing one. The large (small) dots represent the TM (oxygen) ions. (c) Triangular and (d) honeycomb unit cells realizable in ABO_2 and A_2BO_3 compounds correspondingly. The big circles stand for the TM ions and small ones refer to oxygens.

Further investigations were performed for A_2IrO_3 (with A = Li, Na) in [5]. The background remains the same: the Ir^{4+} ions with a single hole residing on the threefold degenerate t_{2g} levels with the effective angular momentum $\tilde{l} = 1$. The strong spin-orbit coupling lifts this

degeneracy and the ground state is the Kramers 1/2- doublet of pseudospins (which is further called 'spins'). In the layered iridates of the type A_2IrO_3, the IrO_6 octahedra share edges but now two interaction channels between Ir are active: the direct orbital overlap between t_{2g} levels and Ir-O-Ir superexchange. Projecting the corresponding multiorbital Hubbard Hamiltonian onto the low-energy subspace yields

$$H_{ij}^{(\gamma)} = -J_1 S_i^\gamma S_j^\gamma + J_2 \mathbf{S}_i \mathbf{S}_j. \tag{3.6}$$

where J_1 and J_2 are governed by three different virtual processes [5]. We introduce the parametrization $J_1 = 2\alpha$, $J_2 = 1-\alpha$, $0 \leq \alpha \leq 1$ and discuss properties of

$$H_{ij}^{(\gamma)} = -2\alpha\, S_i^\gamma S_j^\gamma + (1-\alpha)\mathbf{S}_i \mathbf{S}_j. \tag{3.7}$$

The $\alpha = 0$ regime describes the pure Heisenberg model with a Néel ordered ground state. The opposite limit $\alpha = 1$ reflects the Kitaev model, thus realizing a spin-liquid ground state. Besides, the model is exactly solvable for the intermediate value $\alpha = 1/2$. We consider $\gamma = z$ bond with the Hamiltonian (3.7)

$$H_{ij}^{(z)} = \frac{1}{2}(S_i^x S_j^x + S_i^y S_j^y - S_i^z S_j^z). \tag{3.8}$$

As the next step we divide the lattice into four sublattices and introduce a new rotated operator $\tilde{\mathbf{S}}$. It coincides with the original $\mathbf{S}$ in one of the sublattices (see Fig.3.5(b)) and in the remaining ones two appropriate components of $\tilde{\mathbf{S}}$ differ from $\mathbf{S}$ by the sign (components should be chosen with respect to the given sublattice). That leads to the Hamiltonian

$$\tilde{H}_{ij}^{(\gamma)} = -2(2\alpha-1)\tilde{S}_i^\gamma \tilde{S}_j^\gamma - (1-\alpha)\tilde{\mathbf{S}}_j \tilde{\mathbf{S}}_j. \tag{3.9}$$

Setting $\alpha = 1/2$ we are left with the ferromagnetically (FM) coupled Heisenberg Hamiltonian $\tilde{H}_{ij}^{(\gamma)} = -\frac{1}{2}\tilde{\mathbf{S}}_j \tilde{\mathbf{S}}_j$. The inverse rotation yields a *Stripy* ordering shown in Fig. 3.5(c).

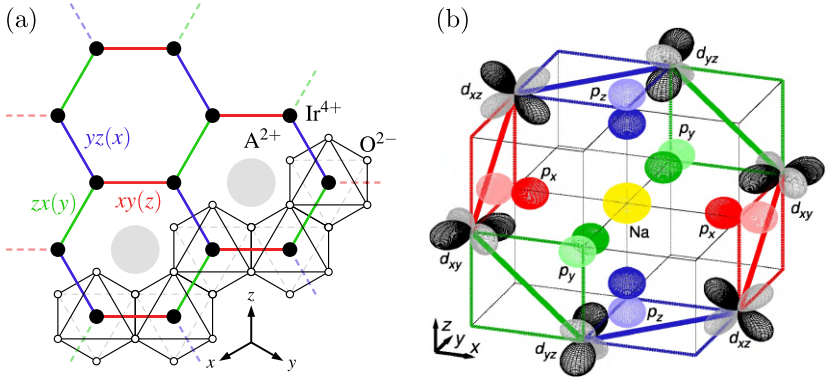

Figure 3.4.: A general overview of the A_2IrO_3 (with $A = Na^{2+}, Li^{2+}$) honeycomb structure from [15]. (b) In particular, a picture of Na_2IrO_3 orbitals from [128]. For each kind of Ir-Ir bond only two appropriate hoppings between t_{2g} levels are possible.

The numerical studies are represented by the Lanczos exact diagonalization[1] of a 24-site cluster (see Fig.3.5(b)), which accepts the previously discussed four-sublattice transformation. The results revealing the phase transitions are given in Fig.3.5.

Nevertheless, neutron scattering experiments in Na_2IrO_3 [31, 32] revealed that another candidate for the ground state of the Kitaev-Heisenberg model is realized - the *zigzag* magnetic order. In fact, one can easily show that the α-parametrization introduced above leads to an oversight [12]. To demonstrate it, we consider the Hamiltonian (3.6) and introduce new parameters: energy scale A and J-K-tuning angle

[1] Details on this technique can be found in Chapter 6

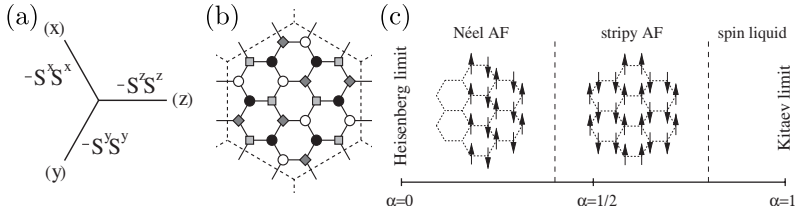

Figure 3.5.: (Figure from [5]) (a) Three bond flavours on the honeycomb lattice labelled with the corresponding Kitaev anisotropic interaction. (b) The four-sublattice system supercell used in numerical simulations and in the transformation (3.9). (c) Schematic phase diagram depending on the exchange couplings parameter α. Exact diagonalization results of the 24-site cluster given in Fig.(b), using Lanczos algorithm (see Chapter 6).

φ as follows

$$H_{ij}^{(\gamma)} = A(2\sin\varphi\, S_i^\gamma S_j^\gamma + \cos\varphi\, \mathbf{S}_i\mathbf{S}_j), \qquad (3.10)$$
$$A = \sqrt{J^2+K^2}, \qquad J = A\cos\varphi, \qquad K = A\sin\varphi.$$

The sublattice transformation $\mathbf{S} \to \tilde{\mathbf{S}}$ performed for the stripy phase leads to the Hamiltonian $\tilde{H}$ of the same structure but with new couplings

$$\tilde{K} = K + J, \qquad \tilde{J} = -J \qquad \Leftrightarrow \qquad \tan\tilde{\varphi} = -\tan\varphi - 1. \qquad (3.11)$$

Exact diagonalization yields the phase diagram of the model, given in Fig. 3.6(a). The whole parameter space $\varphi \in [0, 2\pi]$ can be divided into six different phases – two kinds of Kitaev spin-liquid and four ordered FM, AF, Stripy and Zigzag phases. Remarkably, we observe

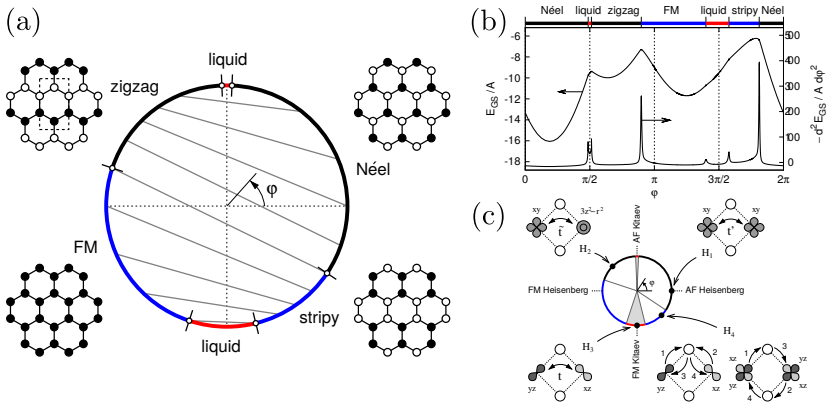

Figure 3.6.: (Taken from [12]) (a) The phase diagram of the Kitaev-Heisenberg model (3.10). Grey lines display the points connected by (3.11). (b) The second derivative $-d^2E_{GS}/d\varphi^2$ of the ground state energy, whose peaks indicate phase transitions. (c) Four different exchange processes that contribute to K and J.

two different φ-intervals corresponding to the opposite Kitaev phases, i.e. FM and AF spin liquids are variously sensible to the J-perturbation.

However, ab initio calculations show that the model (3.10) for the honeycomb iridates is not complete [15]. Introducing N_i, S_i and L_i, which are the total number, spin and angular momentum operators, the Coulomb interaction U and Hund's coupling J_{H}, we start with an atomic Hamiltonian of Kanamori form [129]

$$H_i^{(0)} = \frac{U - 3J_{\mathrm{H}}}{2}(N_i - 5)^2 - 2J_{\mathrm{H}}S_i^2 - \frac{J_{\mathrm{H}}}{2}L_i^2, \tag{3.12}$$

The perturbative kinetic terms are

$$H_{ij}^{\mathrm{kin}} = t_1(d_{i\alpha}^\dagger d_{j\alpha} + d_{i\beta}^\dagger d_{j\beta}) + t_2(d_{i\alpha}^\dagger d_{j\beta} + d_{i\beta}^\dagger d_{j\alpha}) + t_3 d_{i\gamma}^\dagger d_{j\gamma}, \tag{3.13}$$

where operators $d^{\dagger}_{i\alpha}$ denote the creation operators for the t_{2g} orbital α at site i and t_1-t_3 are functions of Slater-Koster parameters ($t_{dd\sigma}$, $t_{dd\pi}$, $t_{dd\delta}$, $t_{pd\pi}$) [130] and of the charge transfer gap Δ_{pd} [100]. The effective Hamiltonian reads as [15]

$$H_{ij}^{(\gamma)} = J\mathbf{S}_i\mathbf{S}_j + KS_i^{\gamma}S_j\gamma + \Gamma(S_i^{\alpha}S_j^{\beta} + S_i^{\beta}S_j^{\alpha}),$$

where

$$\begin{aligned} J &= \frac{4}{27}\Big[\frac{6t_1(t_1+2t_3)}{U-J_H} + \frac{2(t_1-t_3)^2}{U-J_h} + \frac{(2t_1+t_3)^2}{U+2J_H}\Big], \\ K &= \frac{8J_H}{9}\Big[\frac{(t_1-t_3)^2-3t_2^2}{(U-3J_H)(U-J_H)}\Big], \\ \Gamma &= \frac{16J_H}{9}\Big[\frac{t_2(t_1-t_3)}{(U-3J_H)(U-J_H)}\Big]. \end{aligned} \tag{3.14}$$

By analogy with (3.10) we introduce

$$J = \cos\phi\,\sin\theta, \qquad K = \sin\phi\,\sin\theta, \qquad \Gamma = \cos\theta, \tag{3.15}$$

and want to obtain the corresponding phase diagram in the form of a filled circle. Its boundary must represent the previous Kitaev-Heisenberg diagram Fig. (3.6)(a), while the unknown inner part is regulated by θ-angle describing the influence of the cross-terms (Γ). The classical diagram Fig. 3.7(a) is obtained by means of Luttinger-Tisza approximation [131] and a single-$\mathbf{Q}$ ansatz, i.e. considering spin configurations

$$\mathbf{S}_i = \sin\eta_i\big(\mathbf{e}_i^x\cos(\mathbf{Q}\mathbf{r}_i) + \mathbf{e}_i^y\sin(\mathbf{Q}\mathbf{r}_i)\big) + \cos\eta_i\mathbf{e}_i^z \tag{3.16}$$

where the canting angles η_i and local vectors $\mathbf{e}_i^{\gamma}$ are treated as independent variational parameters. Performing minimization with respect to these parameters and $\mathbf{Q}$, one obtains the ground state energy for the given point (ϕ, θ). In Fig. 3.7(a) we find two new phases: 120° ordering and a coplanar incommensurate spiral one.

The Lanczos exact diagonalization provides a quantum phase diagram of the model, given in Fig. 3.7, whose rim reflects the same physics as Fig. 3.6(a) for the given value of ϕ. All the phases, except the incommensurate one, can be similarly established by means of the static spin structure factor

$$S_Q = \frac{1}{N} \sum_{ij} e^{i\mathbf{Q}(\mathbf{r}_i - \mathbf{r}_j)} \langle \mathbf{S}_i \mathbf{S}_j \rangle. \tag{3.17}$$

Classically defined as incommensurate, the IS - labelled phase cannot be correctly treated by exact diagonalization, since the cluster size is too small. As a result, in Fig. 3.7 one does not observe sharp peaks, hence distinct phase transitions around the spiral phase IS are not clearly defined.

3.2 Van-Vleck ions

There is a class of transition metal ions called *Van Vleck ions* or *Van Vleck paramagnets*. In these systems the ground state does not possess a magnetic moment but their paramagnetic susceptibility exceeds the diamagnetic one. This group is represented by rare-earth ions with an even number of electrons on the partially filled $4f$ orbital: Pr^{3+}, Eu^{3+}, Tb^{3+}, Ho^{3+}, Tm^{3+} or $4d$ and $5d$ transition metals with t_{2g}^4 electron configurations, such as Re^{3+}, Ru^{4+}, Os^{4+} or Ir^{5+}. The crystal field splits their multiplets $^{2S+1}L_J$ so that the lowest energy level is a singlet or a non-magnetic doublet [132].

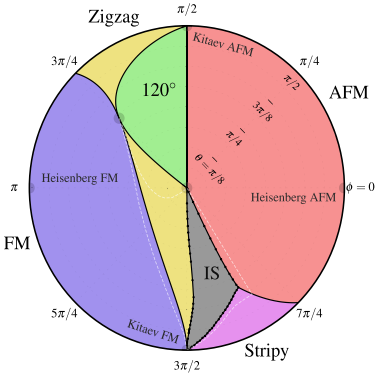

(a) Classical phase diagram with $\Gamma > 0$

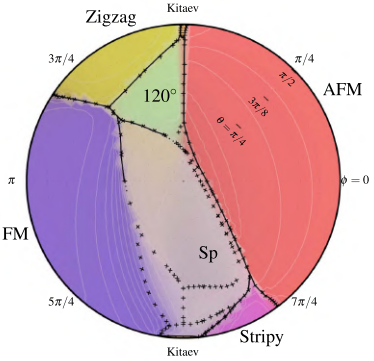

(h) Phase diagram for $\Gamma > 0$

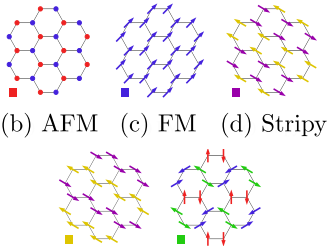

(b) AFM (c) FM (d) Stripy

(e) Zigzag (f) 120°

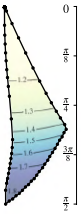

(g) $|\vec{Q}|$ in the IS

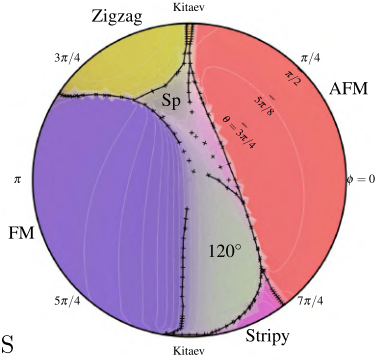

(i) Phase diagram for $\Gamma < 0$

Figure 3.7.: (Figure from [15]) (a) Classical phase diagram based on both Luttinger-Tisza (solid lines) and single-**Q** analysis (surrounded by white dashed lines). (b)-(f) depict classical ground state configurations of the system, whereas (g) shows the **Q**-magnitude in the incommensurate spiral phase. (h) Quantum phase diagram based on the exact diagonalization of 24-site cluster for $\Gamma > 0$ and (i) $\Gamma < 0$. Colours represent S_Q contour map magnitudes while white solid lines display its "equipotential" contours.

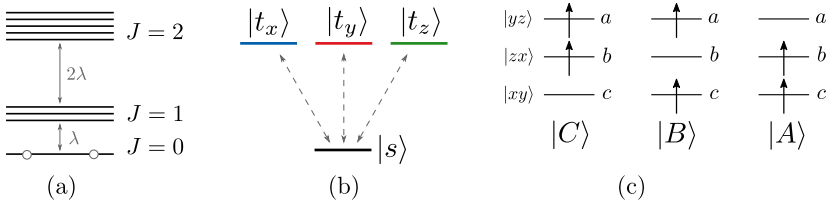

Figure 3.8.: (a) $S = 1$ and $L = 1$ coupled by LS-scheme yield $J = 0$ non-magnetic singlet and separated by λ $J = 1$ triplet (see Eq. (2.19)). We omit $J = 2$ levels, since λ is large. (b) The singlet ground state and three triplon flavours corresponding to the excited $J = 1$ levels. (c) Hole configurations $|A\rangle$, $|B\rangle$ and $|C\rangle$, realized on the t_{2g} subshell.

3.3 Singlet-triplet model for the case of 180° bonding geometry

In order to develop a microscopic theory of magnetism in these materials, we derive a superexchange Hamiltonian [20]. First we study the corner-shared 180° bonding geometry (see Fig. 3.2), which applies to perovskites of the type ABO_3 or A_2BO_4 (e.g. Ca_2RuO_4). Three t_{2g} orbitals d_{yz}, d_{xz} and d_{xy} we label with a, b and c correspondingly. Then hoppings along the c-bond are described by the Hamiltonian

$$H^{(c)} = t \sum_{\langle ij \rangle} (a_i^\dagger a_j + b_i^\dagger b_j + \text{h.c.}). \tag{3.18}$$

Following [20] we introduce operators of the t_{2g}^4 shell orbital configurations

$$A = \{a^2bc\}, \qquad B = \{ab^2c\} \qquad C = \{abc^2\} \tag{3.19}$$

and an effective orbital momentum operator (similar to $\tilde{l}=1$) [114]

$$L_x = -i(B^\dagger C - C^\dagger B), \quad L_y = -i(A^\dagger C - C^\dagger A), \quad L_z = -i(A^\dagger B - B^\dagger A). \tag{3.20}$$

In the second-order perturbation theory one obtains the resulting spin-orbital Hamiltonian (for details see Appendix A)

$$H = \frac{t^2}{U}\sum_\gamma \sum_{\langle ij\rangle\gamma} \Big[(\mathbf{S}_i\mathbf{S}_j + 1)O_{ij}^{(\gamma)} + (L_i^\gamma)^2 + (L_j^\gamma)^2\Big], \tag{3.21}$$

where for the c-bond

$$O_{ij}^{(c)} = (L_i^x L_j^x)^2 + (L_i^y L_j^y)^2 + L_i^x L_i^y L_j^y L_j^x + L_i^y L_i^x L_j^x L_j^y,$$

and operators $O_{ij}^{(a)}$ and $O_{ij}^{(b)}$ can be obtained by means of cyclic permutations of L_x, L_y and L_z (compare the structure of (3.21) to Eq. (2.32)).

The low-energy subspace is spanned by the ground state $J=0$ singlet and the excited $J=1$ triplet separated by λ (see Fig. 3.8). In the $|M_S, M_L\rangle$ basis these states are

$$|s\rangle = \frac{1}{\sqrt{3}}\big(|1,-1\rangle - |0,0\rangle + |-1,1\rangle\big), \quad |t_1\rangle = \frac{1}{\sqrt{2}}\big(|1,0\rangle - |0,1\rangle\big), \tag{3.22}$$
$$|t_{-1}\rangle = -\frac{1}{\sqrt{2}}\big(|-1,0\rangle - |0,-1\rangle\big), \quad |t_0\rangle = \frac{1}{\sqrt{2}}\big(|1,-1\rangle - |-1,1\rangle\big).$$

It is often convenient to use the Cartesian components

$$|t_x\rangle = \frac{1}{i\sqrt{2}}(|t_1\rangle - |t_{-1}\rangle), \quad |t_y\rangle = \frac{1}{\sqrt{2}}(|t_1\rangle + |t_{-1}\rangle), \quad |t_z\rangle = |it_0\rangle, \tag{3.23}$$

and to introduce bond operators [133]

$$\begin{aligned} &s^\dagger|\mathrm{vac}\rangle = |s\rangle, \qquad t_i^\dagger|\mathrm{vac}\rangle = |t_i\rangle, \qquad [s, s^\dagger] = 1, \\ &[t_i, t_j^\dagger] = \delta_{ij}, \qquad [s, t_i] = [s, t_i^\dagger] = 0, \qquad s^\dagger s + t_i^\dagger t^i = 1, \\ &i,j = x,y,z. \end{aligned} \tag{3.24}$$

Since only one state can be found on a given site, an essential constraint $n_s + n_t = 1$ with $n_t = n_x + n_y + n_z \leq 1$ has to be enforced. We also introduce 'transition' hard-core triplon operators $\mathbf{T} = s^\dagger \mathbf{t}$ and their cross product $\mathbf{J} = -i\mathbf{T}^\dagger \times \mathbf{T}$. Using commutation relations for s and t (3.24) one finds

$$n_{T_i} = n_{t_i}, \qquad [T_i, T_j^\dagger] = (1 - 2n_{T_i})\delta_{ij}. \tag{3.25}$$

The $\mathbf{T}$-operators can be expressed in terms of two real fields $\mathbf{u}$ and $\mathbf{v}$[2] as follows [135],[136]:

$$\mathbf{T} = \mathbf{u} + i\mathbf{v}, \qquad \mathbf{u}^2 + \mathbf{v}^2 \leq 1, \qquad \mathbf{u} \cdot \mathbf{v} = 0. \tag{3.26}$$

In order to get the effective theory we project the Hamiltonian (3.21) onto the given subspace, i.e. $H(S, L) \to H(T, J)$, and calculate all matrix elements of its entries (see Appendix B). For example, the operators of spin, angular momentum and magnetic moment ($\mathbf{M} = 2\mathbf{S} - \mathbf{L}$) read as

$$\mathbf{S} = -i\sqrt{\frac{2}{3}}\big(\mathbf{T} - \mathbf{T}^\dagger\big) + \frac{i}{2}\mathbf{J}, \tag{3.27}$$

$$\mathbf{L} = +i\sqrt{\frac{2}{3}}\big(\mathbf{T} - \mathbf{T}^\dagger\big) + \frac{i}{2}\mathbf{J}, \tag{3.28}$$

$$\mathbf{M} = -i\sqrt{6}\big(\mathbf{T} - \mathbf{T}^\dagger\big) + \frac{i}{2}\mathbf{J}. \tag{3.29}$$

Finally, collecting all projections we end up with the Hamiltonian

$$H_{\text{eff}} = \lambda \sum_i n_i + \sum_\gamma H^{(\gamma)}, \qquad H^{(\gamma)} = \frac{t^2}{U} \sum_{\langle ij \rangle} (h_2 + h_3 + h_4)_{ij}^{(\gamma)},$$

[2] These are the coherent states for a spin-1 system [134].

where (for the c-bond)

$$h_2^{(c)} = \frac{11}{3}\mathbf{v}_i \cdot \mathbf{v}_j - v_{iz}v_{jz} + \frac{1}{3}(\mathbf{u}_i\mathbf{u}_j - u_{iz}u_{jz}), \tag{3.30}$$
$$h_3^{(c)} = \frac{1}{\sqrt{24}}(\mathbf{v}_i \cdot \mathbf{J}_j + v_{iz}J_{jz} + u_{ix}Q_{jx} - u_{iy}Q_{jy}) + (i \leftrightarrow j),$$
$$h_4^{(c)} = \frac{3}{4}d_{ij}^\dagger d_{ij} + \frac{1}{2}\mathbf{J}_i \cdot \mathbf{J}_j + \frac{1}{4}(J_{iz}J_{jz} + J_{iz}^2 J_{jz}^2) - \frac{5}{36}n_i n_j$$
$$n = \sum_\gamma T_\gamma^\dagger T_\gamma, \qquad Q_x = -(T_y^\dagger T_z + T_z^\dagger T_y), \qquad \text{etc.}$$

We quantify the interaction by $\kappa = 4t^2/U$. The density of out-of-condensate particles near the critical point is small, hence we neglect $\mathbf{J}$ and Q_γ. Moreover, for the given geometry the bond-dependent terms are irrelevant [2], and hence we substitute $v_{i\gamma}v_{j\gamma}$ with $\mathbf{v}_i\mathbf{v}_j/3$. Thus, we are left with the quadratic Hamiltonian

$$H_2 = \lambda\sum_i n_i + \frac{2\kappa}{9}\sum_{\langle ij\rangle}\Big\{\mathbf{T}_i^\dagger\mathbf{T}_j - \frac{7}{16}\mathbf{T}_i\mathbf{T}_j + \text{h.c.}\Big\}. \tag{3.31}$$

One assumes that the hard-core constraint is fulfilled on average and neglects magnon interactions. Following the singlet-triplet extension of the linear spin-wave theory [137, 138] one performs the Bogoliubov transformation for $\mathbf{T}$-bosons (for details see Appendix D.1), which yields the excitation dispersions

$$\omega_\gamma(\mathbf{k}) = \lambda\sqrt{1 + \frac{\kappa}{\kappa_{\rm cr}}\phi_k}, \qquad \text{with} \qquad \phi_k = \frac{1}{2}\sum_\gamma \cos(k_\gamma), \tag{3.32}$$

where $\kappa_{\rm cr} \sim \frac{2}{5}\lambda$ refers to some critical value of κ. Thus, if $\kappa > \kappa_{\rm cr}$, the gap $\lambda\sqrt{1-(\kappa/\kappa_{\rm cr})}$ closes and we observe a magnetic phase transition driven by condensation of the dipolar part of one of the $\mathbf{T}$-components [20, 43–45, 139]. This yields a finite staggered magnetization

$$M_\gamma = 2\sqrt{6\rho(1-\rho)}, \quad \text{with} \quad \rho = \frac{1}{2}\Big(1 - \frac{1}{\tau}\Big), \quad \tau = \frac{\kappa}{\kappa_{\rm cr}} > 1. \tag{3.33}$$

The M-length (or the Higgs-amplitude mode [53]) fluctuates with a gapped dispersion (for details see Appendix D.2)

$$\omega_\gamma(\mathbf{k}) \simeq \lambda\sqrt{\tau^2+\phi_k}, \tag{3.34}$$

while two other components represent gapless Goldstone modes with

$$\omega_{\alpha/\beta}(\mathbf{k}) \simeq \lambda\frac{\tau+1}{2}\sqrt{1+\phi_k}, \qquad \gamma\neq\alpha\neq\beta\neq\gamma. \tag{3.35}$$

In [20] one applies the above results to Ca_2RuO_4 [22], a d^4 Mott insulator with $\lambda \simeq 75$ meV [23] and with the staggered moment $M \simeq 1.3\mu_B$ [24]. First, this provides reasonable values for $(4t^2/U) \simeq 53$ meV, $t \sim 0.2$ meV and $U \sim 3-4$ eV. Second, the estimated product $LS \simeq -0.2$ [20] does not strongly deviate from the observed one -0.28 ± 0.07 [23]. Furthermore, one obtains the uniform magnetic susceptibility [20]

$$\chi = \frac{12\mu_B^2 N_A}{\lambda(1+\tau)} \simeq 2.3\times10^{-3} \ \text{ emu/mol}, \tag{3.36}$$

while its experimental value above the Néel temperature is $\sim 2.5\times10^{-3}$ emu/mol [22, 24].

Motivated by these predictions, one considered an extension of this model including a tetragonal distortion essential for perovskites, which specifies one component of $\mathbf{T}$ [21]. Introducing the splitting between xy and xz/yz orbitals as $\delta = (E_{xz/yz} - E_{xy})/2$, we obtain the effective Hamiltonian

$$H_{\text{eff}} = \delta\sum_i\Big(n_i^z - \frac{1}{3}n_i\Big) + \lambda\sum_i n_i + J\sum_{\langle ij\rangle a} H_{ij}^{(a)} + J\sum_{\langle ij\rangle b} H_{ij}^{(b)}, \tag{3.37}$$

with

$$H_{ij}^{(a)} = \mathbf{T}_i^\dagger\mathbf{T}_j - \frac{1}{3}T_{i,x}^\dagger T_{j,x} - \frac{5}{6}\mathbf{T}_i\mathbf{T}_j + \frac{1}{6}T_{i,x}T_{j,x} + \text{h.c.}, \tag{3.38}$$
$$n_i = n_i^x + n_i^y + n_i^z,$$

where a and b denote two bonds of a square lattice, $J = t^2/U$ and $H_{ij}^{(b)}$ can be obtained by substituting $T_{i,x} \to T_{i,y}$. Here we do not consider the bond-dependent terms as the average value $\mathbf{v}_i\mathbf{v}_j/3$.

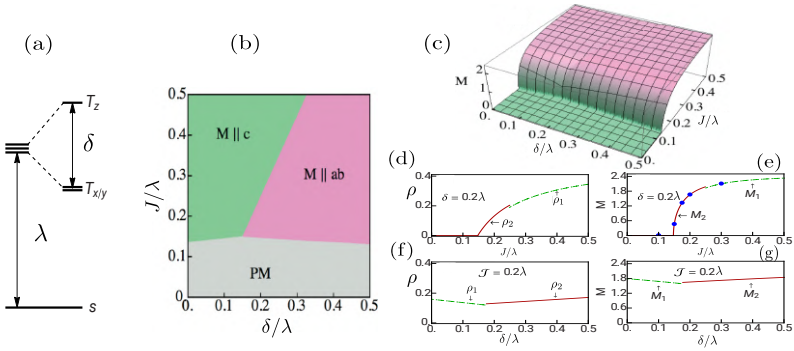

Figure 3.9.: (Taken from [21]): (a) A cartoon of energy levels highlighting the relative orientation of the ground-state singlet and the excited triplet state split by the crystal field δ. (b) Magnetic phase diagram displaying both magnetic phases as a function of J and δ. (c) 3D plot of the magnetisation M, where grid distortions correspond to the phase transitions shown in (b). (d), (e) the condensate density and the magnetic moment for $\delta = 0.2\lambda$ vs. J. (f),(g) $J = 0.2\lambda$ vs. δ.

One observes two different ordered phases depending on the J/δ ratio: an out-of-plane $M \parallel c$ and an in-plane $M \parallel ab$ one. In the first case the condensate density reads as [21]

$$\rho_1 = \frac{1}{2}\Big(1 - \frac{\beta_1}{\kappa_1}\Big), \quad \text{where} \quad \kappa_1 = \frac{22}{3}J \quad \text{and} \quad \beta_1 = \lambda + \frac{2}{3}\delta, \tag{3.39}$$

which yields a critical value $J_{\text{cr}} = (3\lambda+2\delta)/22$. The in-plane orientation

is described by

$$\rho_2 = \frac{1}{2}\Big(1 - \frac{\beta_2}{\kappa_2}\Big), \quad \text{where} \quad \kappa_1 = \frac{19}{3}J \quad \text{and} \quad \beta_1 = \lambda - \frac{1}{3}\delta, \tag{3.40}$$

with $J_{\rm cr} = (3\lambda - \delta)/19$. The staggered magnetic moment is given by

$$M_i = \sqrt{6(1-\eta_i)}, \tag{3.41}$$

where $\eta_i \equiv \beta_i^2/\kappa_i^2$, $i = 1, 2$. These magnetic moments and corresponding condensate densities can be found in Fig. 3.9. In Ca_2RuO_4 the crystal field δ is relatively small, hence the in-plane order is more preferable.

In the relevant in-plane phase the amplitude x-mode dispersion reads as

$$\omega_x(\mathbf{k}) = \sqrt{\kappa_2^2 + \beta_2^2\phi_k}, \tag{3.42}$$

while taking into account the chemical energy shift for the transverse y/z components we obtain

$$\omega_y(\mathbf{k}) = \tilde{\kappa_2}\sqrt{1+\phi_k}, \tag{3.43}$$

$$\omega_z(\mathbf{k}) = (\tilde{\kappa_2} + \delta)\sqrt{1 + \frac{22}{19}\frac{\tilde{\kappa}_2\phi_k}{\tilde{\kappa_2}+\delta}}, \tag{3.44}$$

where $\tilde{\kappa_2} = (\kappa_1 + \beta_1)/2$. The corresponding spin excitation intensities are [21]

$$\mathrm{Im}\chi^{\gamma}_{\mathbf{k}}(\omega) = \frac{|F_\gamma(\mathbf{k})|}{\omega_\gamma(\mathbf{k})}\delta(\omega - \omega_\gamma(\mathbf{k})), \quad \gamma = x, y, z, \tag{3.45}$$

$$F_x(\mathbf{k}) = \frac{3\tilde{\kappa}_2}{19}(-1 + 19\eta_2)\phi_{\mathbf{k}}, \quad F_y(\mathbf{k}) = \frac{54\tilde{\kappa}_2}{19}\phi_{\mathbf{k}}, \quad F_z(\mathbf{k}) = \frac{60\tilde{\kappa}_2}{19}\phi_{\mathbf{k}}.$$

In Fig. 3.10 one can directly compare these intensities at the ordering wave vector M-point (π, π).

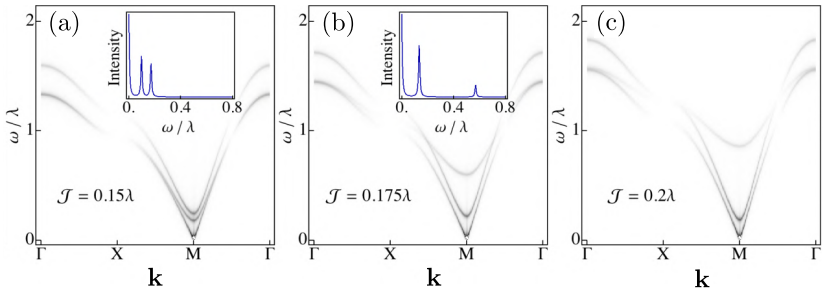

Figure 3.10.: (Taken from [21]) Magnon intensities multiplied by $\sqrt{\omega}$ in the in-plane phase for $\delta = 0.2\lambda$ and (a) $J = 0.15\lambda$, (b) $J = 0.15\lambda$ and (c) $J = 0.175\lambda$. Insets represent the intensities at the ordering **M**-vector. The highest peak is given by the amplitude mode, the middle one by the out-of-plane magnon and the lowest one by the gapless in-plane magnon.

Introducing δ leads to a new result for the magnetic susceptibility (3.36)

$$\chi_{\mathrm{ab}} = \frac{12\mu_{\mathrm{B}}^2 N_A}{\kappa_2(1+\eta_2)}, \tag{3.46}$$

Although it was shown that the resulting magnetic phase of Ca_2RuO_4 can be phenomenologically described by a standard formulation of the Heisenberg model with strong anisotropy terms [140, 141], the Higgs mode and its decay into two Goldstone modes was observed in inelastic neutron scattering expreiments [34] (see Fig. 3.11).

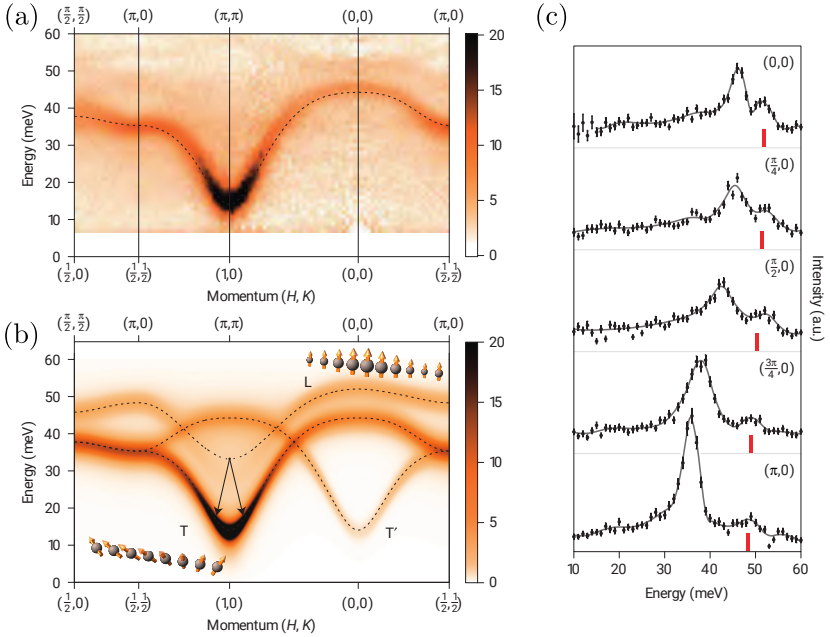

Figure 3.11.: (Fig taken from [34]) (a) Time-of-flight inelastic neutron scattering spectra along high-symmetry directions measured at $T = 5$K. The top axis represents the corresponding undistorted square lattice momenta. The dotted line displays direct comparison to the theoretical results. (b) The excitation spectra given by theory. "T" indicates the transversal mode and "L" the longitudinal one, which carries the Higgs amplitude oscillation. Black arrows highlight the decay of L into two T modes, which conserves the energy and the momentum. (c) Energy spectra along the path $(0, 0) \to (\pi, 0)$. Red bars stand for the theoretically predicted L-mode position.

3.4 Singlet-triplet model for the case of 90° bonding geometry

Now we consider the edge-sharing octahedra (90° bonding geometry). In this case the kinetic Hamiltonian is

$$H^{(c)} = t\sum_{\langle ij\rangle}(a_i^\dagger b_j + b_i^\dagger a_j + \text{h.c.}). \tag{3.47}$$

Using cyclic permutations and the notation introduced above, one obtains

$$\begin{aligned} h_2^{(c)} &= 3(\mathbf{v}_i\cdot\mathbf{v}_j - v_{iz}v_{jz}) - \frac{1}{3}(\mathbf{u}_i\mathbf{u}_j - u_{iz}u_{jz}) \\ &\equiv \frac{2}{3}(T_{ix}^\dagger T_{jx} + T_{iy}^\dagger T_{jy}) - \frac{5}{6}(T_{ix}T_{jx} + T_{iy}T_{jy}) + \text{h.c.}, \\ h_3^{(c)} &= \frac{1}{\sqrt{24}}(3\mathbf{v}_i\cdot\mathbf{J}_j + 3v_{iz}J_{jz} - u_{ix}Q_{jx} + u_{iy}Q_{jy}) + (i\leftrightarrow j), \\ h_4^{(c)} &= -\frac{3}{4}d_{ij}^\dagger d_{ij} + \frac{1}{4}(J_{iz}J_{jz} + Q_{iz}Q_{jz}) + \frac{1}{6}(n_i n_{jz} + n_{iz}n_j) - \frac{1}{12}n_i n_j. \end{aligned} \tag{3.48}$$

The quadratic part of the effective Hamiltonian reads as

$$H_2^{(\gamma)} = \lambda\sum_i n_i + \frac{\kappa}{6}\sum_{\langle ij\rangle}\Big\{(\mathbf{T}_i^\dagger\mathbf{T}_j - T_{i\gamma}^\dagger T_{j\gamma}) - \frac{5}{8}(\mathbf{T}_i\mathbf{T}_j - T_{i\gamma}T_{j\gamma}) + \text{h.c.}\Big\}. \tag{3.49}$$

Therefore, only two flavours of triplons are active on each bond. This does not lead to exotic phenomena on a triangular lattice, as each component of the **T**-vector forms a square sublattice considered above. Still, on a honeycomb lattice each flavour resides on its own quasi one-dimensional zigzag chain (see Fig. 3.12(c)). In the paramagnetic phase

dispersion of the T_z boson is given by[3]

$$\omega_z(\mathbf{k}) \equiv \omega_z(k_y) \approx \lambda \sqrt{1 + \frac{\kappa}{\kappa_{cr}} \cos \frac{\sqrt{3}}{2} k_y}, \tag{3.50}$$

which is purely one-dimensional and we observe a flat band zero mode

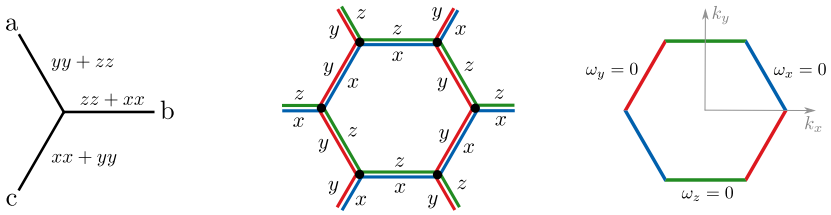

(a) (b) (c)

Figure 3.12.: (Reproduced from [20]) (a) Bonds and active components of $\mathbf{T}$, whereby $yy + zz$ means that only T_y and T_z are present on the given bond. (b) Zigzag chains formed by each flavour. (c) Momenta points indicating the condensation of every T_γ boson on the edges of the first Brillouin zone.

on the Brillouin Zone edges (see Fig.3.12(c)). The other two bosons behave in the same way and condensation takes place for $\mathbf{k}$ lying on the corresponding Brillouin Zone edges. The quadratic part (3.49) does not provide a satisfactory scenario and the h_3 and h_4 terms become of a decisive importance.

The excitonic model of magnetism in d^4 Van-Vleck Mott insulators is intriguing, since for the 180° bonding geometry it is argued to be evidenced experimentally by observation of the amplitude mode in Ca_2RuO_4. Less is known concerning the 90° geometry.

[3]Details are given in Chapter 5 and in Appendix D.1

In Section 3.1 we showed that the proposal for realization of the Kitaev model in Mott insulators [4] with 90° bonding geometry was extended by including the direct exchange interaction channel [5]. The resulting spin 1/2 Kitaev-Heisenberg model (3.6) turned out to be a reliable descriptive theory for the honeycomb iridates.

In this thesis we propose an analogous extension of the excitonic model [20] for the 90° bonding geometry. Similar to [5] we introduce the direct overlap between two neighbouring t_{2g} orbitals. We expect to obtain an effective theory, where triplon interactions are given by the Kitaev-Heisenberg character, i.e. an isotropic full-flavour part competes with a single-flavour bond-dependent anisotropic one. Moreover, a reformulation of (3.48) shows that it already has a prerequisite to have the desired structure:

$$h_2^{(c)} = J_v \sum_{\langle ij \rangle} \mathbf{v}_i \mathbf{v}_j + 2K_v \sum_{\langle ij \rangle c} v_i^z v_j^z + h_{2,u}^{(c)}, \tag{3.51}$$

where $J_v = 3$, $K_v = -3/2$ and $h_{2,u}^{(c)}$ refers to the $\mathbf{u}$-part of $h_2^{(c)}$. Therefore, including the direct exchange can provide more flexibility in couplings and result new interesting physics.

3.5 Excitonic Kitaev-Heisenberg model

Both channels considered together are given by the hopping Hamiltonian [118]

$$\mathcal{H}_{\text{Kin}}^c = \sum_{\sigma,\langle ij \rangle} \left(t a_{i,\sigma}^\dagger b_{j,\sigma} + t b_{i,\sigma}^\dagger a_{j,\sigma} - t' c_{i,\sigma}^\dagger c_{j,\sigma} \right) + h.c., \qquad t, t' > 0,$$

where t' stands for the hopping integral between two orbitals of the same flavour[4]. Reproducing the perturbation theory calculations, we

[4]Its sign is given by the corresponding value of the overlap integral [103].

obtain

$$\mathcal{H}^c_{90^\circ} = \frac{1}{U}\sum_{\langle ij\rangle}(\mathbf{S}_i\mathbf{S}_j+1)\Omega^c_{ij} + \frac{t^2-t'^2}{U}\big((L^z_i)^2+(L^z_j)^2\big) - \frac{4t^2}{U}, \tag{3.52}$$

where the bond-dependent operator is

$$\begin{aligned}\Omega^c_{ij} =& t^2\Big\{(L_x)^2_i(L_y)^2_j + (L_y)^2_i(L_x)^2_j + (L_xL_y)_i(L_xL_y)_j + (L_yL_x)_i(L_yL_x)_j\Big\}\\ &-tt'\Big\{(L_zL_y)_i(L_xL_z)_j + (L_zL_x)_i(L_yL_z)_j + (L_xL_z)_i(L_zL_y)_j\\ &+(L_yL_z)_i(L_zL_x)_j\Big\} + t'^2\Big\{(L_z)^2_i(L_z)^2_j\Big\}.\end{aligned}$$

We introduce the transition operators $x^\dagger_i = T^\dagger_{x,i}$, $y^\dagger_i = T^\dagger_{y,i}$ and $z^\dagger_i = T^\dagger_{z,i}$ and reproduce the projection onto the low-energy subspace. The resulting quadratic part of the effective Hamiltonian is

$$\mathcal{H}^{\text{eff}}_2 = \lambda\sum_i(n^x_i+n^y_i+n^z_i) + \mathcal{H}^{(a)}_2 + \mathcal{H}^{(b)}_2 + \mathcal{H}^{(c)}_2, \tag{3.53}$$

where

$$\begin{aligned}\mathcal{H}^c_2 = \frac{1}{U}\sum_{\langle ij\rangle}\Bigg[& t^2\Big\{\frac{2}{3}(x^\dagger_ix_j+y^\dagger_iy_j) - \frac{5}{6}(x_ix_j+y_iy_j)\Big\}\\ &+tt'\Big\{\frac{11}{12}(x^\dagger_iy_j+y^\dagger_ix_j) - \frac{13}{12}(x_iy_j+y_ix_j)\Big\}\\ &+t'^2\Big\{\frac{1}{6}(x^\dagger_ix_j+y^\dagger_iy_j-x_ix_j-y_iy_j) + \frac{2}{3}(z^\dagger_iz_j-z_iz_j)\Big\}\Bigg] + \text{h.c.}\end{aligned} \tag{3.54}$$

and $\mathcal{H}^{(a/b)}_2$ can be easily derived from (3.54) by means of cyclic permutations of x, y and z.

Alternatively we can introduce the real fields (3.26) as $T_{\gamma,j} = u_{\gamma,j} +$

$iv_{\gamma,j}$ with $\gamma = x, y, z$ and for (3.54) we get

$$\mathcal{H}_2^c = \frac{1}{U}\sum_{\langle ij\rangle}\Big[t^2\big\{3(v_xv_x + v_yv_y)_{ij} - \frac{1}{3}(u_xu_x + u_yu_y)_{ij}\big\} \tag{3.55}$$
$$+tt'\big\{(v_xv_y + v_yv_x)_{ij} - \frac{1}{3}(u_xu_y + u_yu_x)_{ij}\big\}$$
$$+t'^2\big\{\frac{2}{3}(v_xv_x + v_yv_y)_{ij} + \frac{8}{3}(v_zv_z)_{ij}\big\}\Big]$$

New interaction parameters $\{J_v, \Gamma_v, K_v\}$ and $\{J_u, \Gamma_u, K_u\}$ yield the Kitaev-Heisenberg type structure for (3.53):

$$\mathcal{H}_{\text{eff}} = \lambda\sum_i n_i^t + \sum_\gamma\Big\{H_v^\gamma + H_u^\gamma\Big\}, \tag{3.56}$$

$$H_v^\gamma = J_v\sum_{\langle ij\rangle}\mathbf{v}_i\mathbf{v}_j + K_v\sum_{\langle ij\rangle\gamma}v_i^\gamma v_j^\gamma + \Gamma_v\sum_{\langle ij\rangle\gamma}(v_i^\alpha v_j^\beta + v_i^\beta v_j^\alpha) \tag{3.57}$$

$$H_u^\gamma = J_u\sum_{\langle ij\rangle}\mathbf{u}_i\mathbf{u}_j + K_u\sum_{\langle ij\rangle\gamma}u_i^\gamma u_j^\gamma + \Gamma_u\sum_{\langle ij\rangle\gamma}(u_i^\alpha u_j^\beta + u_i^\beta u_j^\alpha), \tag{3.58}$$

with

$$J_v = \frac{9t^2 + 2t'^2}{3U}, \qquad \Gamma_v = tt'/U \qquad K_v = \frac{-3t^2 + 2t'^2}{U} \tag{3.59}$$

and

$$J_u = -\frac{t^2}{3U}, \qquad \Gamma_u = -\frac{tt'}{3U}, \qquad K_u = \frac{2t^2}{3U}, \tag{3.60}$$

where $n_i^t = n_i^x + n_i^y + n_i^z$ and for the given γ holds: $\gamma \neq \alpha \neq \beta \neq \gamma$. This representation of the effective Hamiltonian is suitable for the classical studies (see Chapter 4).

However, the parameter space of the Hamiltonian (3.56) is too large and within the first consideration we omit the quadrupole **u**-terms and we are left with

$$\mathcal{H}_{\text{eff}} = \lambda\sum_i n_i^t + J\sum_{\langle ij\rangle}\mathbf{v}_i\mathbf{v}_j + K\sum_\gamma\sum_{\langle ij\rangle\gamma}v_i^\gamma v_j^\gamma + \Gamma\sum_\gamma\sum_{\langle ij\rangle\gamma}(v_i^\alpha v_j^\beta + v_i^\beta v_j^\alpha), \tag{3.61}$$

which also can be explicitly rewritten in terms of the bosonic operators

$$\begin{aligned}\mathcal{H}_{\text{eff}} = \frac{1}{4}\sum_{\langle ij\rangle a}\Big\{ & J\big(x_i^\dagger x_j + y_i^\dagger y_j + z_i^\dagger z_j - (x_i^\dagger x_j^\dagger + y_i^\dagger y_j^\dagger + z_i^\dagger z_j^\dagger)\big) \\ & + \Gamma\big(z_i^\dagger y_j + y_i^\dagger z_j - (z_i^\dagger y_j^\dagger + y_i^\dagger z_j^\dagger)\big) + K\big(x_i^\dagger x_j - x_i^\dagger x_j^\dagger\big)\Big\} \\ & + \frac{1}{4}\sum_{\langle ij\rangle b}\Big\{ J\big(x_i^\dagger x_j + y_i^\dagger y_j + z_i^\dagger z_j - (x_i^\dagger x_j^\dagger + y_i^\dagger y_j^\dagger + z_i^\dagger z_j^\dagger)\big) \\ & + \Gamma\big(z_i^\dagger x_j + x_i^\dagger z_j - (z_i^\dagger x_j^\dagger + x_i^\dagger z_j^\dagger)\big) + K\big(y_i^\dagger y_j - y_i^\dagger y_j^\dagger\big)\Big\} \\ & + \frac{1}{4}\sum_{\langle ij\rangle c}\Big\{ J\big(x_i^\dagger x_j + y_i^\dagger y_j + z_i^\dagger z_j - (x_i^\dagger x_j^\dagger + y_i^\dagger y_j^\dagger + z_i^\dagger z_j^\dagger)\big) \\ & + \Gamma\big(x_i^\dagger y_j + y_i^\dagger x_j - (x_i^\dagger y_j^\dagger + y_i^\dagger x_j^\dagger)\big) + K\big(z_i^\dagger z_j - z_i^\dagger z_j^\dagger\big)\Big\} + \text{h.c.} \\ & + \lambda\sum_i n_i^t. \end{aligned} \tag{3.62}$$

The latter representation is used in the linear spin-wave studies (see Chapter 5), in the exact diagonalization simulations (see Chapter 6) and in investigating topological properties of the model (Chapter 7).

It is logical to start with the simplest formulation of the theory by eliminating the cross-terms, to obtain the corresponding (J, K) magnetic phase diagram and to compare it to that of the $J = 1/2$ Kitaev-Heisenberg model. In what follows, we suppose J and K to be two independent arbitrary real numbers, since in general many microscopic processes may also contribute our interaction parameters (e.g. Hund's coupling, e_g-mediated processes). Nevertheless, we keep in mind that the physical sector defined within the derived theory is restricted and given by the mutual J-K dependence on t and t' (see Fig. 3.13). To illustrate this fact, we introduce the polar representation (A, α) (3.10):

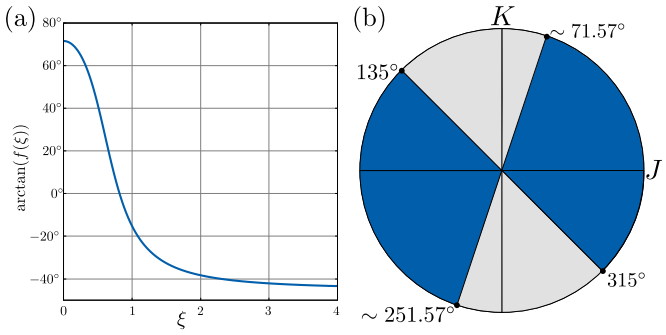

Figure 3.13.: The physical Sector defined by t and t' in terms of polar coupling representation. (a) A direct plot of α as a function of t and t', (b) which is mapped onto the J-K plane. Blue sectors signify the realisable region, while the gray area is unachievable within the considered regime of the theory.

$J = A\cos\alpha$, $K = A\sin\alpha$ with $A = \sqrt{J^2 + K^2}$ and get

$$\tan\alpha = \frac{K}{J} = \frac{-9t^2 + 6t'^2}{9t^2 + 2t'^2} \quad \Rightarrow \quad \alpha = \arctan\frac{-9t^2 + 6t'^2}{9t^2 + 2t'^2} + \pi k$$
$$= \arctan\frac{-9\xi + 6}{9\xi + 2} + \pi k \equiv \arctan f(\xi) + \pi k,$$

where we used $\xi = t^2/t'^2 > 0$ and $k \in \mathbb{Z}$. The resulting physical sector is depicted in Fig. 3.13. One can see that original couplings consistently cover $\sim 65\%$ of the circle. Introducing the Hund's coupling J_{H} or the tetragonal crystal field Δ_{CF} can enlarge the physical sector.

4

Classical analysis of the excitonic Kitaev-Heisenberg model

In this chapter we explore classical properties of the excitonic model. We define classical energies per site for the whole parameter space, discuss possible phases, phase transitions and corroborate these results by performing Markov Chain Monte Carlo studies of the model.

4.1 The classical excitonic Kitaev-Heisenberg model

An appropriate and convenient for the classical analysis formulation of the model is given by the Hamiltonian (3.61). For the sake of simplicity, we exclude Γ-terms within the first consideration and redefine the spin-orbit coupling term in (3.61) using the assumption $u \ll v$ explicitly:

$$n_{i,T} = \mathbf{T}_i^\dagger \mathbf{T}_i = \mathbf{u}_i^2 + \mathbf{v}_i^2 \simeq \mathbf{v}_i^2. \tag{4.1}$$

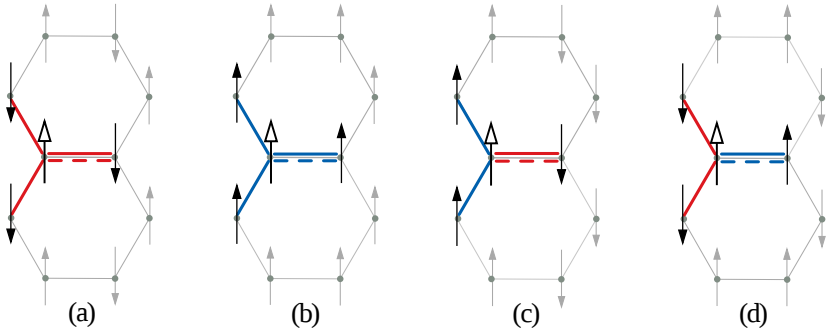

Figure 4.1.: Cartoons of the classical ground state configurations (a) AF Néel, (b) FM, (c) Zigzag, (d) Stripy. The white-headed arrows represent given sites, the bold ones are their neighbours and the pale arrows do not contribute to $E_{\text{class}}/N_{\text{sites}}$. Solid (dashed) lines refer to Heisenberg J (Kitaev K) interaction, while line colours display scalar products $\mathbf{S}_i \cdot \mathbf{S}_j = \pm 1$.

Introducing polar parametrization (3.10) $A = \sqrt{J^2 + K^2}$, $\tan\alpha = K/J$, we obtain the effective Hamiltonian (3.61) in the form

$$H^{\gamma}_{\text{eff}} = \lambda \sum_i n_{t,i} + A\cos\alpha \sum_{\langle ij \rangle} \mathbf{v}_i \mathbf{v}_j + A\sin\alpha \sum_{\langle ij \rangle \gamma} v^{\gamma}_i v^{\gamma}_j . \tag{4.2}$$

The above Hamiltonian resembles the spin-1/2 Kitaev Heisenberg model (3.10), whose classical properties are studied well [10, 11, 142]. In order to emphasize the main differences and similarities between the conventional and the excitonic models, we shortly review the classical spin Hamiltonian

$$H^{\gamma}_{\text{eff}} = \lambda \sum_i \mathbf{S}^2_i + A\cos\alpha \sum_{\langle ij \rangle} \mathbf{S}_i \mathbf{S}_j + A\sin\alpha \sum_{\langle ij \rangle \gamma} S^{\gamma}_i S^{\gamma}_j , \tag{4.3}$$

where all spins are unit vectors, while λ plays the role of a chemical

Phase	AF Néel	FM	Zigzag	Stripy
(a_J, a_K)	$(-3, -1)$	$(3, 1)$	$(1, -1)$	$(-1, 1)$

Table 4.1.: Coefficients, which define proportions between the Heisenberg and the Kitaev couplings for four possible orderings. See Eq. (4.4) and Fig. 4.1.

potential. In the previous Chapter we observed four magnetically ordered configurations: AF, FM, Zigzag and Stripy, depicted in Fig. 4.1. In general the corresponding classical energies per site are expressed as follows

$$E_{\text{class}}^{\text{spins}}(\alpha) = \lambda + \frac{1}{2}\Big(a_J A \cos\alpha + a_K A \sin\alpha\Big), \tag{4.4}$$

where the pairs (a_J, a_K) represent summed scalar products of the neighbouring collinear spins for both interaction channels (see Fig. 4.1) and the prefactor $1/2$ equally divides the energy between two sites sharing the same bond. Without loss of generality we choose z as the alignment axis and thus every spin has only one non-zero component S_z (since all the above mentioned phases are collinear), hence the anisotropic Kitaev interaction gives non-zero contribution only on one bond (in Fig. 4.1 the horizontal one). Therefore, we have four functions $E_{\text{class}}(\alpha)$ given by linear combinations of the trigonometrical functions (see Fig.4.2). These energies compete for the prefix 'ground state' and each of them succeeds on its own α-interval, which can be interpreted as a classical phase diagram. Although one cannot include quantum fluctuations in such a manner, the ordered phases and corresponding α-intervals (see Table (4.2)) fit rather well with the phase diagram in Fig. 3.6(a).

At first glance, we should reproduce all the previous steps in order to likewise obtain the corresponding excitonic classical phase diagram, but a conceptual difference takes place – there is no ordering if the

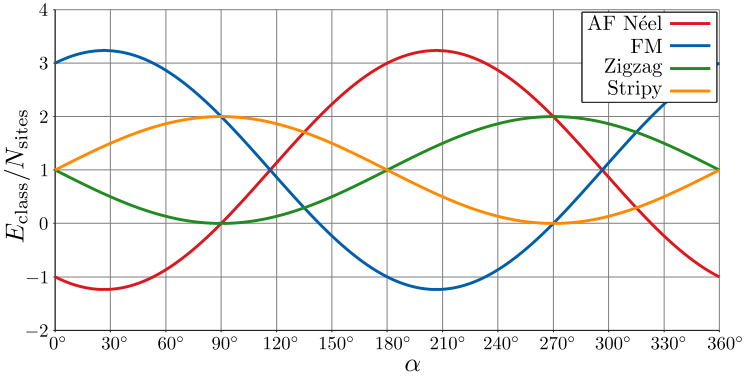

Figure 4.2.: Classical energies per site (4.4) of the spin 1/2 Kitaev-Heisenberg model for $A = 2$ and $\lambda = 1$. This plot demonstrates, which configuration is energetically more favourable for a given α.

exciton condensate is not formed. We illustrate this mechanism first in the **t**-language and then explicitly map it onto the **v**-formalism. As we learnt from Sec. 3.3, the magnetic ordering occurs if the magnitude A exceeds its critical value $A \geq A_{\text{cr}}(\alpha)$ and one of the **t** components condenses with density

$$n_t = t_\gamma^\dagger t_\gamma = \rho, \tag{4.5}$$

where γ denotes the condensed **t**-component (one can set $\gamma = z$, which is the same choice of the alignment axis performed above). The condensate is a coherent mixture of s and t_γ states with the maximal proportion possible $1 : 1$, i.e. $\rho_{\max} = 1/2$, which represents a physical restriction on ρ. Thus, the classical contribution of the spin-orbit coupling per site reads as

$$E_{\text{class}}^{\text{SOC}} = \lambda\rho. \tag{4.6}$$

The vector-boson operators **v** consist of the transition operators **T**

given by a composition of s and $\mathbf{t}$. Let us consider the following expression (here we omit bold letters, as only the condensed component is relevant):

$$T^\dagger T = s^\dagger s\, t^\dagger t = s^\dagger s \cdot n_t = s^\dagger s \cdot \rho. \tag{4.7}$$

Using the hard-core constraint $s^\dagger s + t^\dagger t = s^\dagger s + n_t = s^\dagger s + \rho = 1$ we conclude that

$$s^\dagger s = 1 - \rho \qquad \Rightarrow \qquad T^\dagger T = \rho(1-\rho). \tag{4.8}$$

On the other hand, according to (4.1) at any site i

$$T_i^\dagger T_i \simeq v_i^2 \quad \Rightarrow \quad v_i^2 \simeq \rho(1-\rho) \quad \Rightarrow \quad v_i = \sqrt{\rho(1-\rho)}. \tag{4.9}$$

Therefore, using Eq. 4.6 and inserting expressions for v_i (4.9) into Eq. 4.2 one obtains

$$E^v_{\text{class}}(\alpha) = \lambda\rho + \frac{1}{2}\Big(a_J A\cos\alpha + a_K A\sin\alpha\Big)\rho(1-\rho). \tag{4.10}$$

From the standpoint of classical vectors, the general structure of the Hamiltonian (4.2) is similar to that of the spin model and we assume that the same set of phases should occur[1] and thus a_J and a_K are supposed to be the same. The principal difference is the fact that the length of $\mathbf{v}$-vectors may vary and is governed by the condensate density ρ. Consequently, the absence of ordering for $A < A_{\text{cr}}$ can be associated with zero-length vectors ($\rho = 0$), while in the opposite case $A > A_{\text{cr}}$ the length is given by (4.9) and the ground state energy (4.10) minimized with respect to ρ determines the condensate density as a function of the parameters A and α:

$$\rho = \frac{1}{2}\Big(1 + \frac{2\lambda}{(a_J A\cos\alpha + a_K A\sin\alpha)}\Big). \tag{4.11}$$

[1]This statement is examined in the next section by means of the Markov Chain Monte-Carlo technique without presetting any expected results.

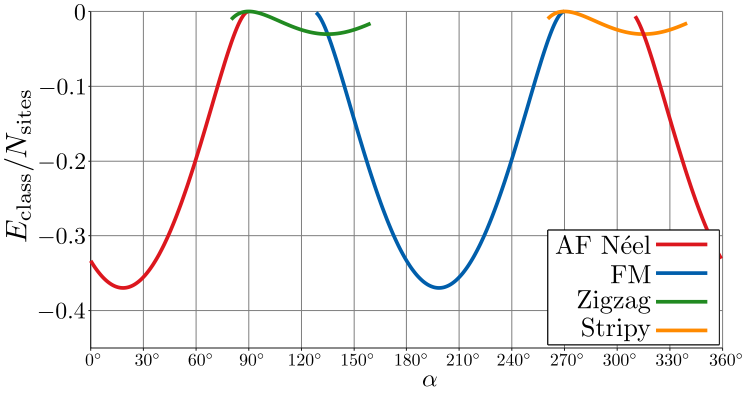

Figure 4.3.: Classical energies of the excitonic model (4.10) sketched in appropriate intervals for $A = 2$ and $\lambda = 1$. Locations of the resulting ground state configurations coincide with those of the spin 1/2 Kitaev-Heisenberg model.

As we mentioned above, the essential physical requirement $0 \leq \rho \leq 1/2$ should hold for any ρ. This automatically makes it impossible to define every phase for $\alpha \in [0°,\ 360°]$. Physical α-boundaries for each phase (a_J, a_K) are determined by the above inequality and the resulting energies defined in the appropriate regions are depicted in Fig. 4.3. We find out that if the ordered ansatz-phases are the ground states of the model (4.2), they arise in the familiar spin model intervals of α, despite the functions $E_{\text{class}}(\alpha)$ being completely different now.

We illustrate the main principles of the classical excitonic model considering the pure Heisenberg case $\alpha = 0°$ with the Hamiltonian

$$H_{\text{eff}}(\alpha = 0°) = \lambda \sum_i n_{t,i} + A \sum_{\langle ij \rangle} \mathbf{v}_i \mathbf{v}_j. \tag{4.12}$$

The corresponding classical energy reads as

$$E_{\text{class}}(\alpha = 0°) = \lambda\rho - \frac{3}{2} A\rho(1-\rho), \tag{4.13}$$

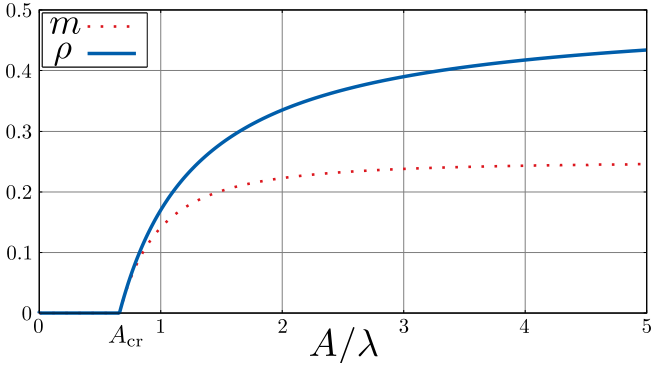

Figure 4.4.: The condensate density ρ and the corresponding magnetic moment $m \sim \sqrt{\rho(1-\rho)}$ versus the magnitude A for $\alpha = 0°$. We note that for $A \to \infty$ the density $\rho \to 1/2$.

and its minimization yields

$$\frac{dE}{d\rho} = 0, \quad \Rightarrow \quad \rho = \frac{1}{2} - \frac{\lambda}{3A} = \frac{1}{2}\Big(1 - \frac{2\lambda}{3A}\Big), \tag{4.14}$$

hence $A_{\mathrm{cr}} = 2\lambda/3$. Using the notation from Sec. 3.3, we introduce a dimensionless parameter $\tau = A/A_{cr}$ and rewrite the condensate density according to [20] as (see Fig. 4.4)

$$\rho = \frac{1}{2}(1 - \tau^{-1}). \tag{4.15}$$

Calculating A_{cr} for each $\alpha \in [0, 360°]$ provides a paramagnetic region, where no condensate emerged (see Fig. 4.5). Moreover, one can notice that phase boundaries (Table (4.2)) do not depend on the magnitude A, which in fact only rescales the classical energies and does not shift the phase transition values of α. Therefore, once α is chosen, the corresponding phase is predetermined, whereas A is merely responsible for formation of the condensate density (and consequently for the or-

Phase	AF Néel	FM	Zigzag	Stripy
α	$(0°, 90°)$, $(315°, 360°)$	$(90°, 135°)$	$(135°, 270°)$	$(270°, 315°)$

Table 4.2.: Ordered phases and α intervals, where these phases represent the ground state. Remarkably, these boundaries are valid for both spin and excitonic models.

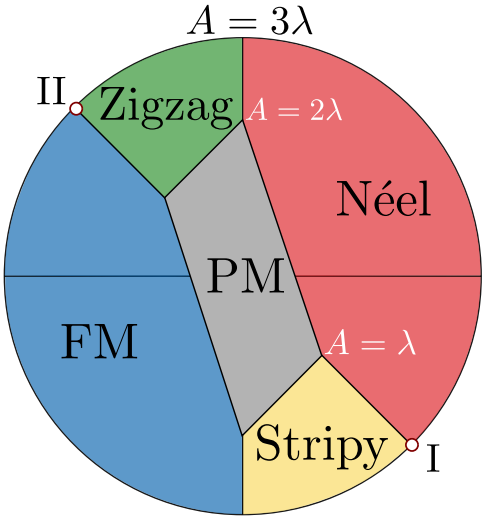

Figure 4.5.: The phase diagram predicted by the classical analysis. In the middle one finds a parallelogram-shaped paramagnetic area, where the condensate density is zero and no magnetic order emerges. The phase colors correspond to those in Fig. 4.3. Points I and II refer to the model (3.49) and its dual one, i.e. with the opposite signs of J, K.

dering). This fact allows us to propose a sketch of the classical phase diagram of the excitonic model (4.2), see Fig. 4.5.

For further calculations (e.g. see Section 5.2) it can be useful to introduce a chemical potential $\mu_n = -\lambda(\tau_n - 1)/2$ for a given phase n, which leads to

$$E^n_{\text{class}} = -\frac{\lambda}{4}\frac{(\tau_n - 1)^2}{\tau_n} = -\mu_n \rho_n. \tag{4.16}$$

In summary, it can be said that we provided the classical description of the excitonic Kitaev-Heisenberg model, defined main physical quantities and obtained a draft for the magnetic phase diagram. However, the phases are predetermined under the assumption that the new degree of freedom, i.e. vector length, does not dramatically change the diagram, where only collinear orderings are present (if we considered vortices, some length variations could bring an energy gain and thus another scenario is more likely to take place).

4.2 Classical Markov Chain Monte Carlo

The Monte-Carlo technique is a large group of methods, used for estimating integrals and simulations of stochastic processes. Known for centuries (e.g. Buffon's needle), the main principle of these methods remains the same: approximation of complex problems by means of repetitive random sampling. In particular, we consider the so-called *Markov Chain Monte Carlo* (MCMC), where Markov Chain postulates connection between 'future', 'present' and 'past', whereas Monte Carlo technique provides appropriate data.

We consider a probability distribution $p(X)$. Monte-Carlo methods generate a sample from this distribution $X_1, X_2, \ldots, X_N \sim p(X)$, which

can be further used as an estimation for probability integrals of the form

$$\langle f(X)\rangle = \frac{1}{Z}\int f(X)p(X)dX, \qquad Z = \int p(X)dX. \tag{4.17}$$

Indeed, if a set $\{X_i\}$ is picked with a given probability distribution $P(X)$ then

$$\langle f(X)\rangle = \frac{\sum_{i=1}^{N} f(X_i)p(X_i)P^{-1}(X_i)}{\sum_{i=1}^{N} p(X_i)P^{-1}(X_i)}, \tag{4.18}$$

and if we choose

$$P(X_i) = \frac{p(X_i)}{Z}, \qquad \Rightarrow \qquad \langle f(X)\rangle \approx \frac{1}{N}\sum_{i=1}^{N} f(X_i). \tag{4.19}$$

Our strategy is to generate a sample from such a distribution $p(X)$ by means of a homogeneous ergodic Markov Chain and an invariant Markov Chain distribution. It can be clarified as follows.

By definition Markov chain is a sequence of stochastic variables $\{X_n\}_{n\geq 0}$ if it satisfies

$$\mathbb{P}(X_n = i_{n+1}|X_n = i_n, X_{n-1}, \ldots, X_0 = i_0) = \mathbb{P}(X_{n+1} = i_{n+1}|X_n = i_n), \tag{4.20}$$

where $\mathbb{P}(X|Y)$ is the conditional probability of the event X given Y. Therefore, this process can be associated with a random walk on a graph [143]. Markov chain is called *homogeneous* if

$$q_n(X_{n+1}|X_n) = q(X_{n+1}|X_n), \tag{4.21}$$

i.e. the transition probability does not depend on the step n. Distribution $\pi(X)$ is called an *invariant distribution* if

$$\pi(X) = \int q(X|S)\pi(S)dS. \tag{4.22}$$

A sufficient condition of any distribution being invariant is so called *detailed balance equation* [143], which reads as

$$\pi(S)q(X|S) = \pi(X)q(S|X). \tag{4.23}$$

Any arbitrary Markov Chain can have more than one invariant distribution. Say $\pi(X)$ is its invariant distribution, then the Markov Chain is said to be *ergodic* if

$$\forall p_0(X) \xrightarrow[n\to+\infty]{} \pi(X), \tag{4.24}$$

where $p_0(X)$ is called a *starting distribution*. Obviously, an ergodic Markov Chain has only one invariant distribution. A sufficient condition of ergodicity is the following property:

$$\forall S, \forall X : \pi(X) \neq 0 : q(X|S) > 0. \tag{4.25}$$

Therefore, if we obtain a homogeneous ergodic Markov Chain and an invariant Markov Chain distribution then starting from some point n the generated set becomes a sample from the distribution $p(X)$ regardless of the initial distribution $p_0(X)$.

The Metropolis-Hastings algorithm was proposed as a tool for simulating molecular systems by Metropolis and Rosenbluth and later improved for the sampling from any probability distribution by Hastings [144]. A short review can be given as follows.

One assumes that the distribution $p(X)$ (target distribution) is defined up to the constant

$$p(X) = \frac{1}{Z}\tilde{p}(X). \tag{4.26}$$

The algorithm starts with an initial guess, for example, at the point n the current Markov chain configuration is known as X_n. Then one generates a new state X_* from an arbitrary proposal probability distribution $r(X|X_n)$, which should be simple enough to pick a sample from it, and calculates the factor

$$A(X_*, X_n) = \min\left(1, \frac{\tilde{p}(X_*)r(X_n|X_*)}{\tilde{p}(X_n)r(X_*|X_n)}\right) \tag{4.27}$$

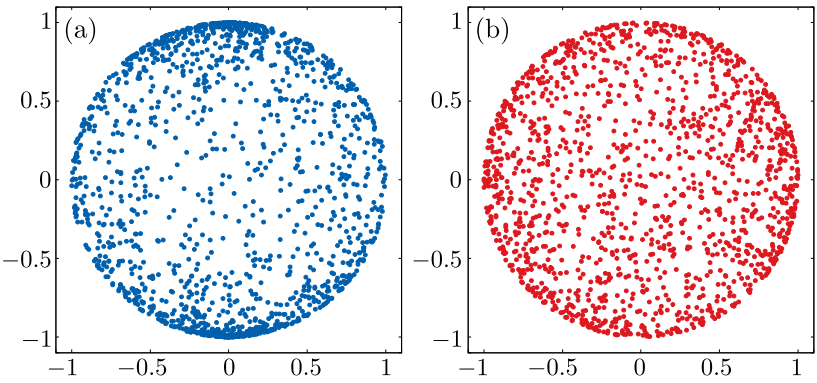

Figure 4.6.: Examples of a distribution of 1000 points on a sphere projected onto the XZ plane. (a) Incorrect. Displays the result of $r = \text{rand}[0, 1]$, $\phi = \text{rand}[0, 2\pi]$, $\theta = \text{rand}[-\pi, \pi]$. (b) Correct. This picture is obtained according to App. C.

The new candidate configuration X_* is accepted as the next step X_{n+1} with the probability $A(X_*, X_n)$. Otherwise, it is rejected and $X_{n+1} = X_n$. Therefore, we have the Markov Chain with a transition probability

$$q(X_{n+1}|X_n) = \begin{cases} r(X_{n+1}|X_n)A(X_{n+1}|X_n), & \text{if} \quad X_{n+1} \neq X_n, \\ 1 - r(X_{n+1}|X_n)A(X_{n+1}|X_n), & \text{if} \quad X_{n+1} = X_n. \end{cases} \tag{4.28}$$

One can see that the posterior distribution (4.26) indeed may be defined up to a normalization constant, since it cancels in (4.27).

Now we consider the Hamiltonian (4.2) with $\mathbf{v}_i$ treated as classical vectors, whose length may vary from 0 to 1. Implementation of the Markov Chain Monte Carlo is realized according to the scheme

i Distribute arbitrarily orientated N vectors of a random length $|\mathbf{v}_i| \leq 1$, $\forall i \leq N$ on the honeycomb lattice with N sites.

ii Calculate the corresponding system energy (up to β: $\ln Z = -\beta\mathcal{H}$)[2].

iii Pick a random lattice site.

iv Change the given vector's parameters, either its length or orientation.

v Compute the new state's energy

vi Draw another random number and if the condition (4.27) is fulfilled, accept the new configuration

vii Repeat the steps ii – vi

First of all, we note that a uniform sampling on a sphere (in a ball) is not a trivial step (see Fig. 4.6) and has to be done carefully (for details see Appendix C).

The second important nuance is hidden behind the condensation phenomenon. To show it explicitly, we rewrite the spin Kitaev-Heisenberg Hamiltonian (4.3), including the spin-orbit coupling and substituting $\mathbf{S}_i$ with vectors in spherical coordinates

$$\begin{aligned}\mathcal{H}_{\text{spins}} = \lambda \sum_i r_i^2 + A\cos\alpha \sum_{\langle ij\rangle} r_i \cdot r_j \, \Theta(\theta_i, \phi_i, \theta_j, \phi_j) \\ + A\sin\alpha \sum_{\langle ij\rangle\gamma} r_i \cdot r_j \, \Theta^{\gamma}(\theta_i, \phi_i, \theta_j, \phi_j),\end{aligned} \tag{4.29}$$

$$\begin{aligned}\Theta(\theta_i, \phi_i, \theta_j, \phi_j) = \cos\phi_i \sin\theta_i \cdot \cos\phi_j \sin\theta_j \\ + \sin\phi_i \sin\theta_i \cdot \sin\phi_j \sin\theta_j + \cos\theta_i \cdot \cos\theta_j\end{aligned} \tag{4.30}$$

where $\Theta^{\gamma}(\theta_i, \phi_i, \theta_j, \phi_j)$ represents one of the angular terms (4.30), depending on the chosen bond γ. Despite both $\mathbf{S}$ and $\mathbf{v}$ being usual vectors in $3D$, once again we face the crucial difference governed by

[2]Thermal fluctuations are given by $\beta \sim 1000$.

the longitudinal degree of freedom. Being associated with our model, the spin Hamiltonian provides wrong results, since the decisive role in the excitonic case is played by the condensate, which transforms each vector into

$$\mathbf{v}_i = \sqrt{\rho_i(1-\rho_i)}\bar{\mathbf{v}}_i(\theta_i, \phi_i), \tag{4.31}$$

where $\bar{\mathbf{v}}_i(\theta_i, \phi_i)$ is a unit vector fixing the orientation[3] on the site i and ρ_i is the 'local' condensate density[4]. Thus, the Hamiltonian 4.2 is given by

$$\begin{aligned}\mathcal{H} =&\lambda \sum_i \rho_i + A\cos\alpha \sum_{\langle ij\rangle} \sqrt{\rho_i(1-\rho_i)} \cdot \sqrt{\rho_j(1-\rho_j)}\, \Theta(\theta_i, \phi_i, \theta_j, \phi_j) \\ &+A\sin\alpha \sum_{\langle ij\rangle\gamma} \sqrt{\rho_i(1-\rho_i)} \cdot \sqrt{\rho_j(1-\rho_j)}\, \Theta^\gamma(\theta_i, \phi_i, \theta_j, \phi_j),\end{aligned} \tag{4.32}$$

There are two obvious ways of introducing the real-space vector length: either we set $r_i = \sqrt{\rho}$ and get

$$\begin{aligned}\mathcal{H}^{(1)}_{\mathrm{MCMC}} =&\lambda \sum_i r_i^2 + A\cos\alpha \sum_{\langle ij\rangle} r_i \cdot r_j \sqrt{1-r_i^2}\sqrt{1-r_j^2}\, \Theta(\theta_i, \phi_i, \theta_j, \phi_j) \\ &+A\sin\alpha \sum_{\langle ij\rangle\gamma} r_i \cdot r_j \sqrt{1-r_i^2}\sqrt{1-r_j^2}\, \Theta^\gamma(\theta_i, \phi_i, \theta_j, \phi_j),\end{aligned} \tag{4.33}$$

or $r_i = \sqrt{\rho_i(1-\rho_i)}$ with

$$\begin{aligned}\mathcal{H}^{(2)}_{\mathrm{MCMC}} =&\frac{\lambda}{2} - \frac{\lambda}{2}\sum_i \sqrt{1-4r_i^2} + A\cos\alpha \sum_{\langle ij\rangle} r_i \cdot r_j\, \Theta(\theta_i, \phi_i, \theta_j, \phi_j) \\ &+A\sin\alpha \sum_{\langle ij\rangle\gamma} r_i \cdot r_j\, \Theta^\gamma(\theta_i, \phi_i, \theta_j, \phi_j),\end{aligned} \tag{4.34}$$

[3]In the previous Section we wrote $v_i = \sqrt{\rho(1-\rho)}$, since we had chosen z as the alignment axis, or equivalently $\bar{\mathbf{v}} = \mathbf{e}_z$.

[4]Within the framework of MCMC we start with different lengths (and hence ρ's) and vary them on a local level. However, after many iterations they become the same everywhere and the index 'i' can be omitted.

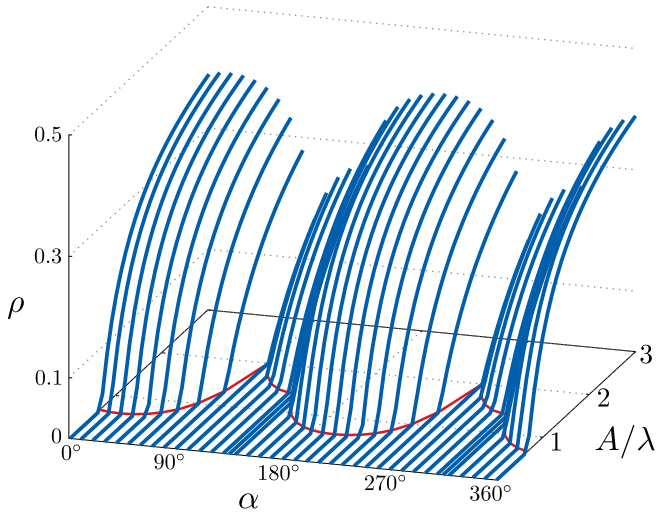

Figure 4.7.: Condensate densities given for various angles α obtained by MCMC. The red line represents the behaviour of A_{cr}, which is mapped onto the diagram (little red-white squares in Fig (4.9)) and thus restricts the paramagnetic phase.

where in (4.34) originates as a solution of the equation $\rho_i^2 - \rho_i + r_i^2 = 0$ for $0 \leq r_i, \rho_i \leq 1/2$. Comparing Hamiltonians (4.29) and $\mathcal{H}^{(1)/(2)}_{\mathrm{MCMC}}$ we capture an unusual behaviour of the longitudinal degree of freedom in the excitonic model (either in the nearest-neighbours interaction or in the spin-orbit coupling term).

These Hamiltonians can shed light on some properties of the system even before we start MCMC simulations. For the sake of simplicity we set $\alpha = 0$ and hence the second line in (4.33)/(4.34) vanishes. Therefore, in the Hamiltonian (4.33) the antiparallel orientation of two neighbouring vectors is energetically favourable for the second term. This corresponds to the maximal value of the length $r_i\sqrt{1 - r_i^2}$ (i.e. $1/2$ for

$r_i = 1/\sqrt{2}$ or $\rho = 1/2$). In contrast, the first term favours $r_i^2 \to 0$. In (4.34) vice versa, the second term tends to reach the maximum of $\sqrt{1-4r_i^2} = 1$ (for $r_i = 0$) and the last one prefers $r_i \to \max(r_i) = 1/2$. In both cases for dominant λ we expect to observe $r_i \sim 0$ but once A is 'large enough' (as we already know $A \geq A_{\mathrm{cr}}$) the length r_i increases, and for $A \to \infty$ one predicts $\rho \to 1/\sqrt{2}$. Summarizing, if λ is fixed then the classical ordering is very improbable for small A, since $r_i \sim 0$ and there is nothing to get ordered. In the opposite case we expect to find an ordered phase with $r_i \to 1/\sqrt{2}$ or $\rho \to 1/2$ for $A \to \infty$. These estimations coincide with the results obtained in the previous section.

We choose the Hamiltonian (4.33) and find its ground state configurations (r_i, θ_i, ϕ_i), $i \in \{1, N\}^5$ for every $\alpha \in [0, 360°]$, calculate the averaged square length as a function of A

$$\bar{r^2}(A) = \frac{1}{N}\sum_{i=1}^{N} r_i^2(A) = \bar{\rho}(A), \tag{4.35}$$

and the structure factor

$$S^{\alpha,\beta}(\mathbf{q}) = \frac{1}{N^2}\sum_{\langle ij\rangle}\langle \mathbf{v}_i^{\alpha}\mathbf{v}_j^{\beta}\rangle e^{-i\mathbf{q}(\mathbf{R}_i - \mathbf{R}_j)}, \tag{4.36}$$

where $\langle \dots \rangle$ refers to the thermal averaging and $\mathbf{R}_i$ to the position vector of the site i.

4.3 Classical phase diagram of the excitonic Kitaev-Heisenberg model

The final classical phase diagram can be found in Fig. 4.9. The ordered phases are identified both by direct observation of the ground

[5] In our simulations we used $N = 12\times12,\ 24\times24,\ 36\times36,\ 48\times48$ and in some cases $N = 72\times72$ as well.

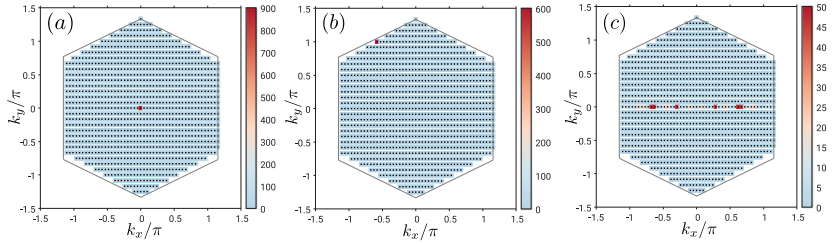

Figure 4.8.: Spin structure factor (4.36) in the first Brillouin zone for $N = 48\times48$ sites and $A = 3$ indicating the following ground states: (a) FM at $\alpha = 180°$, (b) Zigzag at $\alpha = 120°$ and (c) independent AF chains at $\alpha = 315°$.

state configurations and by means of the structure factors (4.36) (see Fig. 4.8). This diagram coincides with Fig. 4.5 and confirms our previous estimations. Indeed, in Fig. 4.7 we see functions $\rho(A, \alpha)$, given by the averaged squared length (4.35) (since we choose the formulation (4.33), this value directly reflects the condensate density ρ). One can see that for every α the density remains zero if the interaction magnitude is not 'large enough', i.e. if it does not exceed its critical value A_{cr} (see the red line in Fig. 4.7). Thus, for each α we can read off its $A_{\text{cr}}(\alpha)$ and map it onto the polar grid, which results in the parallelogram-shaped area provided in the previous Section (see white squares in Fig. 4.9).

Of particular interest is the special point $\alpha = 315°$ (or alternatively $K = -J,\ J > 0$), as it represents the model (3.49) and the corresponding ground state remained unclear. According to the results of MCMC simulations these parameters correspond to a phase transition between Zigzag and AF phases, while the ground state is given by a set of independent one-dimensional AF zigzag chains (see Fig. 4.9). For its dual point $\alpha = 135°$ ($K = -J,\ K > 0$) we observe the phase transition

between Stripy and FM orderings and the ground state is represented by a set of independent FM one-dimensional chains. The spin structure factor for these points is nonzero for all momenta lying along a line within the first Brillouin zone, which was predicted in Fig. 3.12(d).

In the pure Kitaev regimes $\alpha = 90°,\ 270°$ we find the classical spin liquid. The corresponding ground state is infinitely degenerate and represented by configurations with short-ranged correlations only.

Inclusion of the cross-terms yields diagrams very similar to [15] (see Fig. 3.7(a)). However, the condensation mechanism provides paramagnetic regions, whose borders slowly and asymmetrically shrink with growth of Γ.

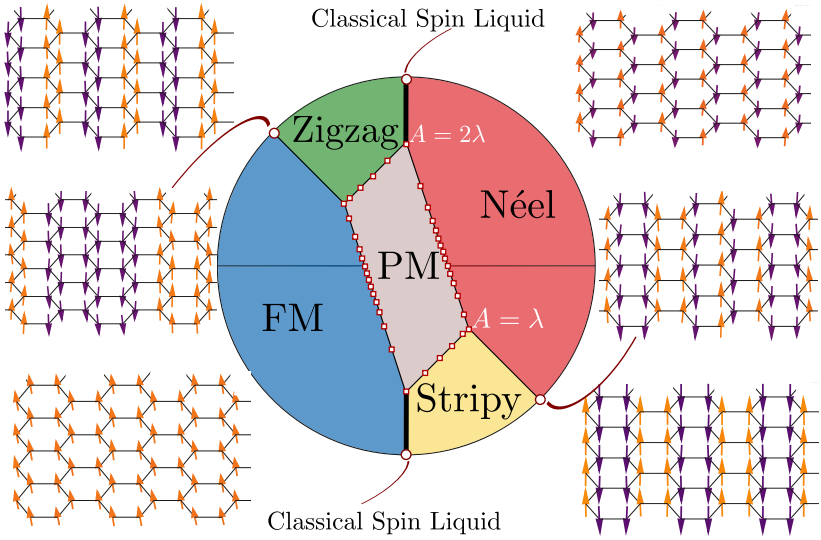

Figure 4.9.: Classical phase diagram with the ground state configurations. Apart from the classical analysis prediction represented by the long-range ordered AF, FM, Zigzag, Stripy phases and disordered paramagnetic region, we observe phase transitions, given by two rays $\alpha = 90°,\ 270°$ with the classical spin liquid ground state and two rays ($\alpha = 135°,\ 315°$) with purely one-dimensional long-range correlations. Red-white squares reflect the mapped values A_{cr} illustrated with the red line in Fig. 4.7.

5

Linear spin wave theory

In this Chapter we apply the linear spin wave theory to the excitonic model and find the excitation spectra in both paramagnetic and ordered phases.

5.1 Excitations in the paramagnetic phase

We consider the Hamiltonian (4.2), which is studied classically in the previous Chapter

$$H_{\text{eff}} = \lambda \sum_i (n_{i,x} + n_{i,y} + n_{i,z}) + H(v_x) + H(v_y) + H(v_z). \tag{5.1}$$

Since it is free of the cross-terms, which mix different components of $\mathbf{v}$, we can divide (4.2) into three equivalent single-flavour contributions and consider each of them separately (for example, the z-part). Moreover, the honeycomb lattice is bipartite, hence we distinguish two inequivalent sublattices and label one of them with tilde. Therefore, the z-contribution reads as

$$H^z_{\text{eff}} = \lambda \sum_i (n_{i,z} + n_{i,\tilde{z}}) + A\cos\alpha \sum_{\langle ij \rangle} v^z_i \tilde{v}^z_j + A\sin\alpha \sum_{\langle ij \rangle_c} v^z_i \tilde{v}^z_j \tag{5.2}$$

We reformulate (5.2) in terms of the hard-core transition operators **T** (3.26):

$$v_i^z = \frac{1}{2i}(z_i - z_i^\dagger) \qquad \text{where} \qquad z_i \equiv T_{i,z}, \tag{5.3}$$

and finally get the quadratic Hamiltonian

$$\begin{aligned} H_{\text{eff}}^z =& \lambda \sum_i z_i^\dagger z_i + \lambda \sum_i \tilde{z}_i^\dagger \tilde{z}_i + \frac{A}{4}\cos\alpha \sum_{\langle ij\rangle} \left(z_i^\dagger \tilde{z}_j + \tilde{z}_j^\dagger z_i - z_i \tilde{z}_j - z_i^\dagger \tilde{z}_j^\dagger\right) \\ &+ \frac{A}{4}\sin\alpha \sum_{\langle ij\rangle c} \left(z_i^\dagger \tilde{z}_j + \tilde{z}_j^\dagger z_i - z_i \tilde{z}_j - z_i^\dagger \tilde{z}_j^\dagger\right), \end{aligned} \tag{5.4}$$

The Hamiltonian (5.4) can be diagonalized according to the following recipe: switch to the momentum space performing the Fourier transformation and apply the Bogolyubov transformation subsequently [145]. The Fourier-transformed z-triplon operator takes the form

$$z_i = \frac{1}{\sqrt{N}} \sum_k z_k e^{-ikr}, \qquad \text{etc.} \tag{5.5}$$

and we obtain the Hamiltonian (5.4) in the momentum space

$$\begin{aligned} \mathcal{H}_{\text{eff}}(k) = \sum_k \Big\{ & \lambda(z_k^\dagger z_k + \tilde{z}_k^\dagger \tilde{z}_k) + \gamma_k \tilde{z}_k^\dagger z_k \\ & + \gamma_k^* z_k^\dagger \tilde{z}_k - \gamma_k^* z_k \tilde{z}_{-k} - \gamma_k z_k^\dagger \tilde{z}_{-k}^\dagger \Big\}, \end{aligned} \tag{5.6}$$

where

$$\begin{aligned} &\gamma_k = \frac{3A}{4}\phi_k, \qquad \phi_k = \frac{1}{3}(e^{-ik_a} + e^{-ik_b} + e^{-ik_c})\cos\alpha + \frac{1}{3}e^{-ik_c}\sin\alpha, \\ &k_a = -\frac{1}{2}k_x - \frac{\sqrt{3}}{2}k_y, \qquad k_b = -\frac{1}{2}k_x + \frac{\sqrt{3}}{2}k_y, \qquad k_c = k_x. \end{aligned} \tag{5.7}$$

We introduce a generalized Bogoliubov transformation [145] (see Appendix 5.6), which gives us the dispersion relation

$$\omega_k(A,\alpha) = \sqrt{\lambda^2 \pm 2\lambda|\gamma_k|} = \lambda\sqrt{1 \pm \frac{3A|\phi_k(\alpha)|}{2\lambda}}. \tag{5.8}$$

One can notice that expression (5.8) provides information about the paramagnetic boundaries, which can be compared to the classical results. One takes the squared norm $|\phi_k|^2$ and rewrites it as

$$|\phi_k(\alpha)|^2 = \frac{1}{9}\Big\{4\cos^2\frac{\sqrt{3}}{2}k_y\,\cos^2\alpha + 4\sqrt{2}\cos\frac{\sqrt{3}}{2}k_y\,\cos\frac{k_x}{2}\,\sin(\alpha+45^\circ)\cos\alpha + \sin(2\alpha)+1\Big\}. \tag{5.9}$$

It is a function of (k_x, k_y) and for each α its maximum defines $A_{\rm cr}(\alpha)$. This problem can be solved for an arbitrary α and yields $A_{\rm cr}(\alpha)$ depicted in Fig. 5.1(e), which perfectly coincides with that of Fig. 4.9. Remarkably, the current approach is valid only in the paramagnetic phase for $A < A_{\rm cr}(\alpha)$, whereas the classical methods operate in terms of the condensate densities for $A > A_{\rm cr}(\alpha)$. However, both techniques yield the same function $A_{\rm cr}(\alpha)$, which indicates that their applicability borderlines coincide.

Another important property of (5.8) is its invariance under a shift of the J-K-tuning angle: $|\phi_k(\alpha)| = |\phi_k(\alpha+\pi)|$, which allows us to investigate the excitonic model only for $\alpha \in [0,\pi]$[1]. Let us consider several important cases in more detail.

1) $\alpha = 0$, the pure Heisenberg Hamiltonian with positive J. This translates (5.9) into

$$|\phi_k(0)| = \frac{1}{3}\sqrt{4\cos^2\frac{\sqrt{3}}{2}k_y + 4\cos\frac{\sqrt{3}}{2}k_y\cos\frac{3}{2}k_x + 1}. \tag{5.10}$$

The maximal value of $|\phi_k(0)|$ corresponds to the excitation energy minima and is given by

$$\max|\phi_k(0)| = 1 \quad \text{at} \quad \Big(\pm\frac{2\pi}{3}, \pm\frac{2\pi}{\sqrt{3}}\Big), \Big(\pm\frac{4\pi}{3}, 0\Big) \quad \text{and} \quad \Big(0,0\Big), \tag{5.11}$$

[1]This holds only in absence of Γ-terms.

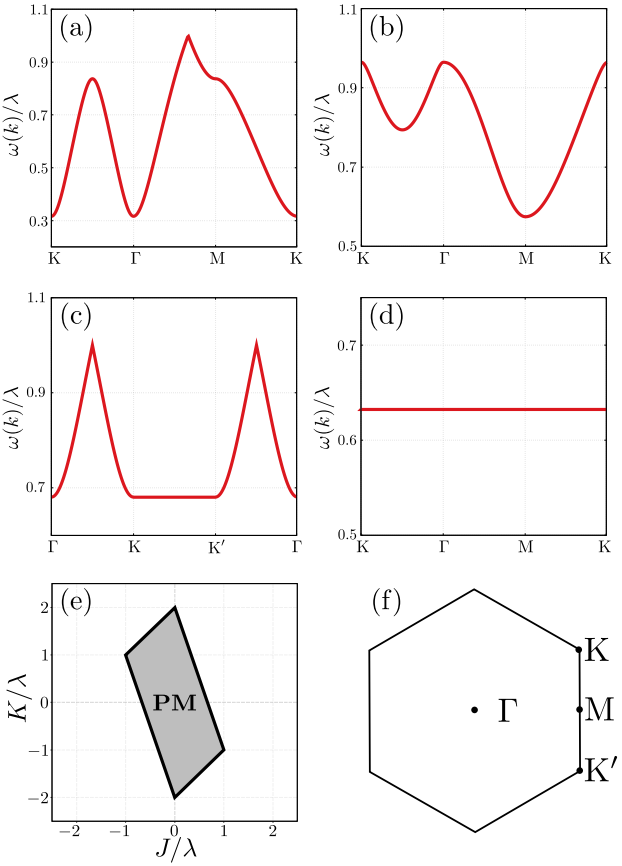

Figure 5.1.: Excitation energies ω_k in the paramagnetic phase for $A = 0.5\lambda$ and (a) $\alpha = 0°$, (b) $\alpha = 120°$, (c) $\alpha = 315°$, (d) $\alpha = 90°$. (e) Polar representation of the paramagnetic parameter subspace. (f) First Brillouin Zone and the symmetry points.

which indicates the AF excitations. Furthermore, substituting (5.11) directly into (5.8)

$$\omega_k^{\text{crit}} = \lambda\sqrt{1 - \frac{3A}{2\lambda}}, \tag{5.12}$$

one finds the critical magnitude $A_{\text{cr}} = 2\lambda/3$ (compare to Eq. (4.14)).

2) $\alpha = 315°$, this value refers to the original excitonic model [20]. From (5.9) we have

$$|\phi_k(315°)|^2 = \frac{4}{9}\Big|\cos^2\frac{\sqrt{3}}{2}k_y\cos^2(315°)\Big| = \frac{\sqrt{2}}{3}\cos\frac{\sqrt{3}}{2}k_y, \tag{5.13}$$

which means that this regime describes the one-dimensional propagation of the z- boson along its 'own' particular zigzag direction (see Fig. 3.12(b)). The critical magnitude is defined by

$$\omega_k(315°) = \lambda\sqrt{1 - \frac{3\cdot A\cdot\sqrt{2}}{3\cdot 2\lambda}\cos\frac{\sqrt{3}}{2}k_y} = \lambda\sqrt{1 - \frac{A}{\lambda\sqrt{2}}\cos\frac{\sqrt{3}}{2}k_y}. \tag{5.14}$$

Thus, as soon as $A = A_{\text{cr}} \equiv \lambda\sqrt{2}$, a flat band emerges (see Fig. 3.12 and Fig. 5.1 (c))[2].

3) $\alpha = 120°$, corresponds to the Zigzag phase on the classical diagram, which yields

$$|\phi_k(120°)|^2 = \frac{1}{9}\Big(\cos^2\frac{\sqrt{3}}{2}k_y - \frac{1}{2}(\sqrt{6}-\sqrt{2})\cos\frac{\sqrt{3}}{2}k_y\,\cos\frac{k_x}{2} - \frac{\sqrt{3}}{2} + 1\Big),$$
$$\max(|\phi_k(120°)|) \simeq 0.43 \qquad \text{at} \qquad \Big(0, \pm\frac{2\pi}{\sqrt{3}}\Big) \tag{5.15}$$

and one gets $A_{\text{cr}} \simeq 1.55$ with minimum at the M-point indicating the Zigzag excitations.

4) $\alpha = 90°$, the pure Kitaev anisotropic interaction. Therefore,

$$|\phi_k(90°)| = \frac{1}{3}, \tag{5.16}$$

[2]In [20] $A_{cr} = 4\lambda/3$ compared to $A_{cr} = \lambda\sqrt{2}$ in our calculation. This difference is caused by neglecting **u**-terms in the current work.

and finally

$$\omega_k = \lambda\sqrt{1 - \frac{A}{2\lambda}}. \tag{5.17}$$

Thus, we observe a dispersionless band with $\omega_k = \text{const}$ and $A_{\text{cr}} = 2\lambda$.

5.2 Excitations in the ordered phase

One can reproduce the above calculations in the ordered phases as well, i.e. determine excitations for $A > A_{\text{cr}}$. If the gap in (5.8) closes and the z-boson condenses, the magnetisation reads as

$$M_z = \sqrt{\rho(1-\rho)}, \qquad \text{with} \qquad \rho = \frac{1}{2}(1 - \tau^{-1}), \qquad \tau = \frac{A}{A_{\text{cr}}} \tag{5.18}$$

and M-length fluctuations are given by (for details see Appendix D.2):

$$\omega_z(k, \alpha) \simeq \lambda\sqrt{\tau^2 + |\phi_k(\alpha)|}, \tag{5.19}$$

which is the gapped amplitude Higgs mode. The other two components get an energy shift $-\mu n_{x/y}$, where μ is the chemical potential (4.16). Thus, the transversal dispersions read as

$$\omega_{x/y}(\mathbf{k}) = \lambda\frac{\tau + 1}{2}\sqrt{1 + |\phi_k(\alpha)|}, \tag{5.20}$$

which are gapless Goldstone modes.

6

Exact diagonalization studies

In this Chapter we continue our numerical studies, performing the the Lanczos algorithm based exact diagonalization. We start with a brief introduction giving an overview on the corresponding technical questions. Then we apply the method onto our model, obtain a quantum phase diagram and discuss a new order-by-disorder generated triplon liquid phase.

6.1 Main principles of the exact diagonalization technique

Exact diagnalization is a powerful tool in investigating quantum many-body systems on finite clusters. This technique allows us to calculate the ground state energy and dynamical correlation functions, which can be observed in many experiments (e.g. neutron scattering). Moreover, exact diagonalization treats the hard-core constraint explicitly.

The main idea is to construct the Hamilton matrix $\mathcal{D} \times \mathcal{D}$, where $\mathcal{D} = \dim \mathcal{H}$ is the Hilbert space dimension, and to 'exactly' solve the eigenproblem by diagonalizing the matrix. However, $\mathcal{D}$ grows exponentially with the cluster size, e.g. in general for the excitonic model on a cluster with N_{sites} one has $\mathcal{D} = 4^{N_{\text{sit}}}$. Even being restricted to only

even numbers of particles (since triplons can be created only in pairs) the corresponding dimension is given by

$$\begin{aligned}\mathcal{D}_{\text{even}} &= \sum_{i=0}^{N/2}\binom{N}{2i}\Big\{\sum_{j=0}^{N/2-i}\binom{N-2i}{2j}\Big[\sum_{k=0}^{N/2-i-j}\binom{N-2i-2j}{2k}\Big]\Big\} \\ &= \frac{1}{4}\sum_{i=0}^{N/2}\binom{N}{2i}\left(9^{\frac{N}{2}-i}+1\right) = 2^{N-2}+2^{2N-3},\end{aligned} \tag{6.1}$$

where $\binom{n}{k} = \frac{n!}{k!(n-k)!}$ refers to a binomial coefficient and N is supposed to be even. The exponential growth of $\mathcal{D}$ provokes an exponential growth of the Hamilton matrix size $\sim \mathcal{D}^2$, whereas the computation time scales as $\sim \mathcal{D}^3$. Therefore, a direct treatment of such matrices by means of Householder tridiagonalization cannot be performed.

On the other hand, one can see that in absence of long-range interactions a non-zero contribution to the Hamilton matrix is given only by the diagonal and hopping terms ($N_{\text{terms}} \sim N_{\text{part}} \times N_{\text{Neigh}}$). Such a matrix is called *sparse* [146] and can be diagonalized by means of an iterative scheme, called a *Lanczos algorithm* [147–149]. Thus, in what follows the term 'exact diagonalization' refers to a solution of the Hamiltonian eigenproblem by means of the Lanczos algorithm.

6.2 Lanczos algorithm

Starting with an arbitrary normalized vector $|\phi_0\rangle$, we want to obtain the $L+1$-dimensional *Krylov space* of H over $|\phi_0\rangle$ (the Lanczos basis):

$$\mathcal{K}^L(|\phi_0\rangle) = \text{span}(|\phi_0\rangle, H|\phi_0\rangle, H^2|\phi_0\rangle, \ldots, H^N|\phi_0\rangle). \tag{6.2}$$

Our goal is to find the state of the lowest energy in $\mathcal{K}^L(|\phi_0\rangle)$. The iterative procedure works as follows: we take the first basis vector $|\phi_0\rangle$

and obtain the second one by orthogonalizing $H|\phi_0\rangle$ to $|\phi_0\rangle$

$$|\tilde{\phi_1}\rangle = H|\phi_0\rangle - |\phi_0\rangle\langle\phi_0|H|\phi_0\rangle \tag{6.3}$$

and normalizing it obtain $|\phi_1\rangle$. With $a_0 = \langle\phi_0|H|\phi_0\rangle$ and $b_1^2 = \langle\tilde{\phi_1}|\tilde{\phi_1}\rangle$ we get

$$H|\phi_0\rangle = b_1|\phi_1\rangle + a_0|\phi_0\rangle, \tag{6.4}$$

and thus

$$b_1|\phi_1\rangle = |\tilde{\phi_1}\rangle = H|\phi_0\rangle - a_0|\phi_0\rangle. \tag{6.5}$$

Then we calculate $H|\phi_1\rangle$, orthogonalize and normalize it to all previous vectors

$$b_2|\phi_2\rangle = |\tilde{\phi_2}\rangle = H|\phi_1\rangle - \sum_{i=0}^{1}|\phi_i\rangle\langle\phi_i|H|\phi_1\rangle = H|\phi_1\rangle - a_1|\phi_1\rangle - b_1|\phi_0\rangle, \tag{6.6}$$

with $a_1 = \langle\phi_1|H|\phi_1\rangle$ and $b_2^2 = \langle\tilde{\phi_2}|\tilde{\phi_2}\rangle$. The next vector is

$$b_3|\phi_3\rangle = |\tilde{\phi_3}\rangle = H|\phi_2\rangle - \sum_{i=0}^{2}|\phi_i\rangle\langle\phi_i|H|\phi_2\rangle = H|\phi_2\rangle - a_2|\phi_2\rangle - b_2|\phi_1\rangle. \tag{6.7}$$

The last term vanishes, since the orthogonality of the basis vectors $|\phi_0\rangle$, $|\phi_1\rangle$ and $|\phi_2\rangle$ together with (6.5) implies $\langle\phi_1|H|\phi_0\rangle = 0$.

All following vectors are obtained according to the above scheme:

$$b_{n+1}|\phi_{n+1}\rangle = |\tilde{\phi}_{n+1}\rangle = H|\phi_n\rangle - \sum_{i=0}^{2}|\phi_i\rangle\langle\phi_i|H|\phi_n\rangle = H|\phi_n\rangle - a_n|\phi_n\rangle - b_n|\phi_{n-1}\rangle, \tag{6.8}$$

where $a_n = \langle\phi_n|H|\phi_n\rangle$ and $b_n^2 = \langle\tilde{\phi}_n|\tilde{\phi}_n\rangle$. We rewrite (6.8) and get

$$H|\phi_n\rangle = b_n|\phi_{n-1}\rangle + a_n|\phi_n\rangle + b_{n+1}|\phi_{n+1}\rangle, \tag{6.9}$$

hence $H|\phi_n\rangle$ is orthogonal to all basis states, except $|\phi_n\rangle$ and $\phi_{n\pm1}\rangle$.

We can perform this procedure until the Hilbert space dimension is reached or equivalently a convergence criterion can be set, e.g. $\langle\tilde{\phi}_{n+1}|\tilde{\phi}_{n+1}\rangle < \varepsilon$. Finally the Hamiltonian becomes tridiagonal

$$H = \begin{pmatrix} a_0 & b_1 & 0 & 0 & \dots \\ b_1 & a_1 & b_2 & 0 & \dots \\ 0 & b_2 & a_2 & b_3 & \dots \\ 0 & 0 & b_3 & a_3 & \dots \\ \vdots & \vdots & \vdots & \vdots & \ddots \end{pmatrix} \tag{6.10}$$

It seems that one can easily solve the complete eigenproblem with the Lanczos basis of the Hilbert space dimension. However, the basis analytically proven to be orthogonal may quickly lose this property in a numerical realisation, since floating-point arithmetic is not absolutely accurate. Luckily, another advantage of this technique is its fast convergence, i.e. the ground state can be reached in couple of hundreds steps.

6.3 Implementation

We consider the Hamiltonian (3.62) omitting Γ-terms and neglecting the prefactor 1/4 originating from the **v**-definition[1]

$$H_{\text{eff}} = \lambda \sum_i (n_x + n_y + n_z) + H_x + H_y + H_z, \tag{6.11}$$

$$H_x = A\cos\alpha \sum_{\langle ij\rangle} \left(x_i^\dagger x_j - x_i^\dagger x_j^\dagger\right) + A\sin\alpha \sum_{\langle ij\rangle a} \left(x_i^\dagger x_j + -x_i^\dagger x_j^\dagger\right) + \text{h.c.},$$

$$H_y = A\cos\alpha \sum_{\langle ij\rangle} \left(y_i^\dagger y_j - y_i^\dagger y_j^\dagger\right) + A\sin\alpha \sum_{\langle ij\rangle b} \left(y_i^\dagger y_j - y_i^\dagger y_j^\dagger\right) + \text{h.c.},$$

$$H_z = A\cos\alpha \sum_{\langle ij\rangle} \left(z_i^\dagger z_j - z_i^\dagger z_j^\dagger\right) + A\sin\alpha \sum_{\langle ij\rangle c} \left(z_i^\dagger z_j - z_i^\dagger z_j^\dagger\right) + \text{h.c.},$$

[1] Hence, in order to compare the 'quantum' A_{cr} to the classical results, one has to multiply it by four.

where $x_i^\dagger = T_{x,i}^\dagger$, $y_i^\dagger = T_{y,i}^\dagger$ and $z_i^\dagger = T_{z,i}^\dagger$ respectively. Since (6.11) does not contain cross-terms, besides the even total particle number we expect to have the even number of particles of each flavour. This leads to a Hilbert space dimension given by the expression (6.1) (and not 4^N anymore).

A more thorough analysis of orderings and quantum fluctuations at $T = 0$ can be provided by an investigation of the dynamical susceptibility, in our case given by a Fourier transformed **M**-**M** correlation function

$$\chi_{\gamma\gamma}(\omega, \mathbf{k}) = i \lim_{\epsilon \to +0} \int \langle \Psi_0 | [M_{\mathbf{k}}^\gamma(t), M_{-\mathbf{k}}^{\gamma\dagger}(0)] | \Psi_0 \rangle e^{i\omega t} e^{-\epsilon t} dt, \qquad (6.12)$$

where $|\Psi_0\rangle$ is the cluster ground state and

$$M_{\mathbf{k}}^\gamma = -i\sqrt{6}\left(\mathbf{T}_{\mathbf{k}}^\gamma - \mathbf{T}_{\mathbf{k}}^{\gamma\dagger}\right) = \frac{-i\sqrt{6}}{N^2} \sum_{\mathbf{r}} \left(\mathbf{T}_{\mathbf{r}}^\gamma - \mathbf{T}_{\mathbf{r}}^{\gamma\dagger}\right) e^{-i\mathbf{k}\mathbf{r}}, \qquad (6.13)$$

is the Fourier transformed magnetic moment operator. The excitations intensity is given by the imaginary part of the susceptibility $\chi_{\gamma\gamma}(\omega, \mathbf{k})$, which for $\omega > 0$ reads as

$$\chi''_{\gamma\gamma}(\omega, \mathbf{k}) = -2\sqrt{6} \lim_{\epsilon \to +0} \mathrm{Im} \big\langle \Psi_0 \big| v_{\mathbf{k}}^\gamma \frac{1}{\omega + E_0 + i\varepsilon - H} v_{-\mathbf{k}}^\gamma \big| \Psi_0 \big\rangle, \quad (6.14)$$

or by inserting the full set of states one obtains

$$\chi''_{\gamma\gamma}(\omega, \mathbf{k}) = 2\sqrt{6}\,\pi \sum_{|\Phi\rangle} \big| \langle \Phi | v_{-\mathbf{k}}^\gamma | \Psi_0 \rangle \big|^2 \delta(\omega - E_\Phi), \qquad (6.15)$$

where E_Φ is the energy of the excited state $|\Phi\rangle$.

The fluctuation-dissipation theorem connects the dynamical structure factor with the imaginary part of the dynamical susceptibility for $T = 0$ and $\omega > 0$ as follows

$$S^{\gamma\gamma}(\mathbf{k}, \omega) = -\frac{1}{\pi} \mathrm{Im} \chi_{\gamma\gamma}(\omega, \mathbf{k}). \qquad (6.16)$$

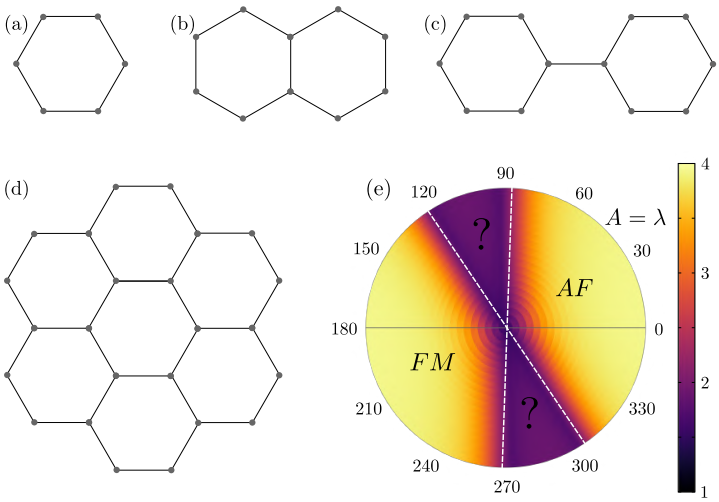

Figure 6.1.: Clusters used $N_{\text{sites}} = $ (a) 6, (b) 10, (c) 12, (d) 24. (e) Dominant static structure factor (6.17) among the accessible $\mathbf{k}$-points for the $N = 6$ cluster. Colour represents its intensity, while white lines indicate maxima of $-d^2 E_{\text{GS}}/d\alpha^2$. Although low-correlated sectors cannot be identified for a such small cluster, here we demonstrate, how the magnetic phase diagram is produced in our further investigations.

Of particular interest is the corresponding static structure factor

$$S^{\gamma\gamma}(\mathbf{k}) = \int_{-\infty}^{+\infty} \frac{d\omega}{2\pi} S^{\gamma\gamma}(\mathbf{k}, \omega). \tag{6.17}$$

6.4 Quantum phase diagram of the excitonic Kitaev-Heisenberg model

We want to find out, which phases can be observed in the complete J-K parameter space, collect this information and present it similar to Fig.3.6. Since the excitonic model possesses the interaction magnitude (with respect to λ) degree of freedom, we expect to get a "filled" circle (e.g. see Fig.4.9). In previous Chapters the filling was accomplished either according to the lowest configuration energy per site or to both real space orderings and the structure factor. Within the framework of exact diagonalization we indicate phases by means of the static structure factor and its values in the First Brillouin Zone, similar to Fig.4.8. However, compared to MCMC simulations, where $N_{\text{sites}} = 48 \times 48$, the clusters allowed by our computational capacity (see Fig. 6.1(a)-(d)) seem to be tiny. This fact restricts the number of available $\mathbf{k}$-points and makes producing pictures similar to Fig.4.8 impossible[2]. Luckily, even the $N = 12$ cluster provides a sufficient amount of the symmetry points (e.g. Γ, Γ', K, M) and thus represents the minimal cluster required for detecting the ordered phases.

We start discussing the phase diagram, which results from the $N_{\text{sites}} = 6$ cluster, see Fig. 6.1(e). We plot the dominant among all the $\mathbf{k}$-points contribution of the static structure factors (6.17) and represent intensities by color. White dashed lines display the second derivative $-d^2E_{\text{GS}}/d\alpha^2$ peaks at $\alpha = 88°,\ 124°,\ 268°,\ 304°$. At first glance, it resembles the classical circle phase diagram, as it can also be divided into four similar sectors with AF and FM orderings present. Nevertheless, many differences occur. First of all, there is no explicit parallelogram-

[2]Introducing twisted boundary conditions [150–155] can be a possible solution of this problem but the structure of the Hamiltonian (6.11) makes this technique inapplicable.

shaped disordered area in the middle but two low-correlated sectors instead, and their location coincides with that of Zigzag/Stripy phases on the classical diagram. In fact, the **M**-vector necessary for such ordering is not covered by the momentum space given by the cluster and hence, the corresponding structure factor cannot be numerically evaluated for it.

We continue with the $N_{\text{sites}} = 12$ system. First, one should note that any $N_{\text{sites}} = 12$ honeycomb lattice cluster cannot be symmetric with respect to a four-sublattice cluster division (required for zigzag or stripy-like orderings) and thus cannot be equally translated along all directions. As a consequence, one of **T** components becomes special, for example in our case it is T_y. This leads to a notable difference between the static factors $S^{xx/zz}(\mathbf{k})$ and $S^{yy}(\mathbf{k})$ in the Zigzag/Stripy regime, whereas in all the remaining sectors they take the same values. Therefore, considering this cluster by 'structure factor' we mean $S^{yy}(\mathbf{k})$.

Fig. 6.2 represents an illustrative interpretation of the $N_{\text{sites}} = 12$ exact diagonalization data. As before, we express our results in polar coordinates and divide the parameter space with respect to momentum vectors maximizing the structure factor and its magnitude indicating the ordering. White dots refer to the structure factor inflection points and thus restrict the paramagnetic area around the origin, where boson densities are small and no ordering is found. This region, as well as familiar AF/FM sectors, resembles the classical diagram.

The second derivative of the ground-state energy predicts phase transitions for $\alpha = 86°, 99°, 134°, 266°, 279°, 314°$. Contrary to the $N_{\text{sites}} = 6$ cluster, the **M**-vectors are accessible and they maximize the structure factor, indicating Zigzag/Stripy orderings approximately in the same sectors as estimated by classical methods.

The dynamical magnetic susceptibilities can be found in Fig.6.3. For three different angles $\alpha = 0°, 120°$ and $135°$ we can observe evolution of $\chi^{yy}(\omega, \mathbf{k})$ with growth of the magnitude A (in units of λ). In

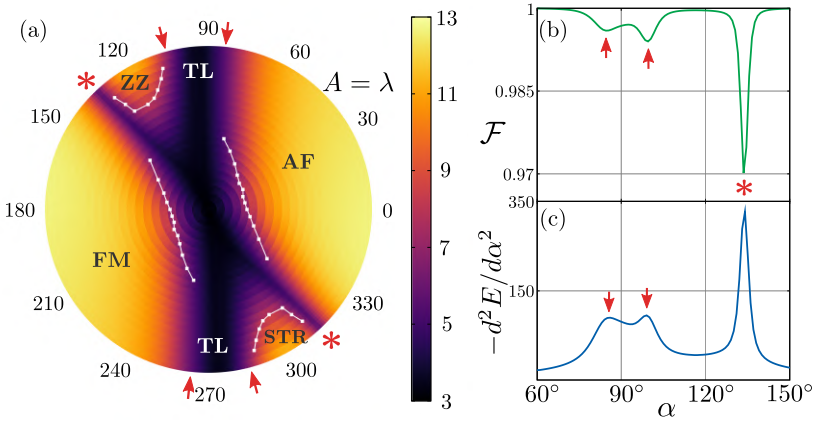

Figure 6.2.: Magnetic phase diagram obtained for the $N_{\text{sites}} = 12$ cluster. (a) The structure factor $S^{yy}(\mathbf{k})$ based polar phase diagram. Colour displays the dominant factor's intensity and white dots give its inflection points. The orderings are associated with the $\mathbf{k}$-vector maximizing the $S(\mathbf{k})$ and the new labelling TL stands for 'triplon liquid' (see text). (b) Fidelity and (c) second derivative of the ground-state energy calculated for the outer border $A = \lambda$ in the upper semicircle (which is sufficient due to $\alpha \to \alpha + 180°$ symmetry). Asterisk and arrows establish correspondence between the panels.

Fig.6.3(a) we notice a typical gap [142] originating from finite size effects, namely from tunneling between two equivalent AF ground states. Fig. 6.3(b) displays vanishing of a low-energy gap in χ^{yy} at the M-point and Fig. 6.3(c) shows an equal gap for Γ and M points, which is an expected result (see Eq. (5.14), Fig. 5.1(c) and Fig. 4.8).

Notably we have two new sectors enclosing the pure Kitaev $\alpha = 90°/270°$ points, where presumably no ordering is present. Nevertheless, they require special attention. In the spin 1/2- Kitaev-Heisenberg model ground state of the same sectors is given by the Kitaev spin liquid. We are dealing neither with spin-1/2 nor with fermions, rather with spin-1 hard-core bosons performing bond-dependent anisotropic interactions. Therefore, there are no obvious clues for the origin of these two dark sectors (e.g. in the spin-1/2 Kitaev-Heisenberg model these sectors harbour the spin-liquid ground state, which is determined by the exactly solvable Hamiltonian itself). The structure factors[3] are low and equal for all available $\mathbf{k}$, as well as the susceptibility χ^{yy} low-energy gaps are the same $\forall\mathbf{k}$. Thus, our previous markers do not provide any comprehensive information about the system any more.

An initial guess could be taken from the classical methods, which manifested themselves very well so far. However, there are no similar sectors in the classical diagrams except two 'classical spin liquid' points, where the ground states are infinitely degenerate and no real space long-range order is present. Moreover, in Fig. 6.4 we observe different ground-state energies compared in the strong-coupling limit $A \gg \lambda$, where the classical energy is expected to fit well with the quantum ones. Fig. 6.4 confirms that assumption, except for the Kitaev point, where quantum fluctuations play the key role.

We should first verify, whether these dark regions represent genuine

[3]Analogously to the **M**-structure factor one can calculate the corresponding **u**-factor, indicating the quadrupole order, and demonstrate that it is not realized either.

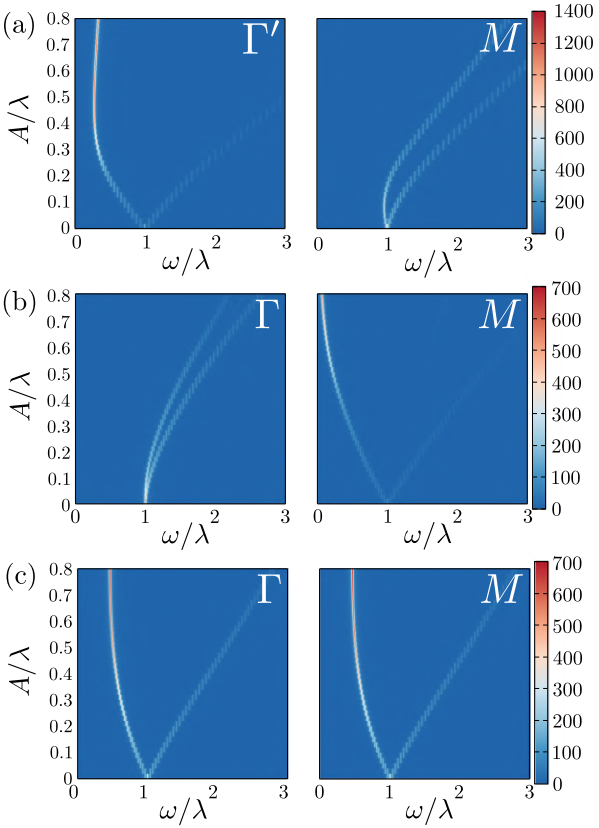

Figure 6.3.: Contour map of the susceptibility $\chi^{yy}(\omega, \mathbf{k})$ dependence on the interaction magnitude A for (a) AF ordering at $\alpha = 0°$, (b) Zigzag at $\alpha = 120°$ and (c) the original excitonic model regime at $\alpha = 135°$. White capital letters indicate the fixed momentum vector $\mathbf{k}$.

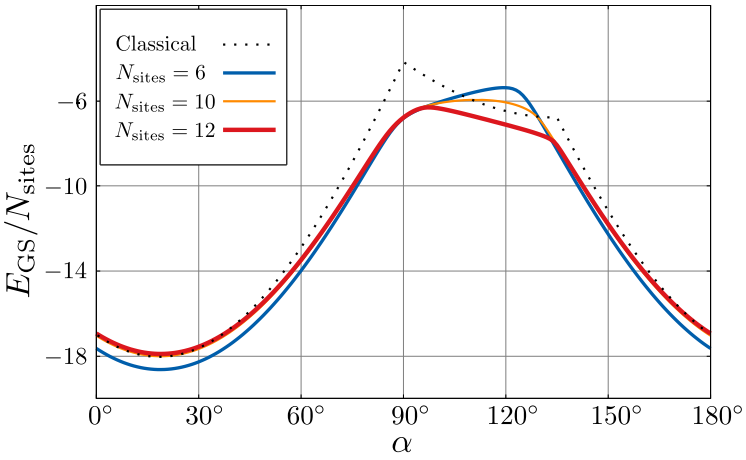

Figure 6.4.: Comparison of the rescaled ground state energies for $A = 10$ versus the tuning angle α. One can see that quantum fluctuations at $\alpha = 90°$ provide a drastic difference between classical and quantum results even on a small cluster.

phases or they simply reflect continuous overlaps between two different neighbouring phases. Furthermore, the second derivative peaks at $\alpha = 86°, 99°$ are not as sharp as those at 135°. Thus, we introduce another quantity detecting phase transitions – the ground-state fidelity

$$\mathcal{F}(\alpha) = \langle \Psi_{\text{GS}}(\alpha) | \Psi_{\text{GS}}(\alpha + \delta\alpha) \rangle. \tag{6.18}$$

It is defined as the overlap between two states separated in parameter space by a small interval, which in our case is represented by two ground states at α and $\alpha + \delta\alpha$. The absolute value of the ground-state fidelity depends on the step $\delta\alpha$, which we can set so that within one phase $\mathcal{F} \simeq 1$. If at some point $\mathcal{F}(\alpha_0)$ sinks down then a small alteration $\delta\alpha$ caused remarkable changes in the ground state, thus excluding the continuous overlap scenario. In Fig. 6.2(b) we observe three minima:

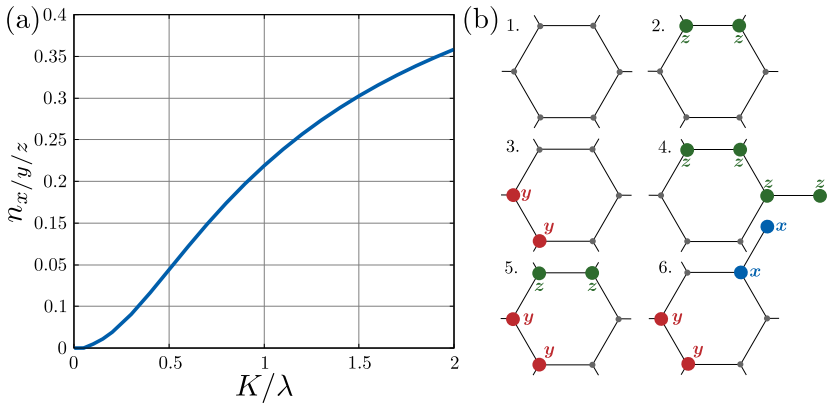

Figure 6.5.: Obtained by $N_{\text{sites}} = 24$ exact diagonalization: (a) the triplon density as a function of the Kitaev coupling for $\alpha = 90°$, (b) examples of configurations observed in the triplon liquid phase.

a strong one at $\alpha \simeq 135°$ and two smaller ones. These results are in consonance with the second derivative peaks and we conclude that the Kitaev-sectors are very likely to define phases.

Let us consider the pure Kitaev case $\alpha = 90°$, where only bond-dependent terms are present, i.e.

$$H_{\text{Kit}} = \lambda \sum_i n_i^t + K \Big\{ \sum_{\langle ij \rangle a} x_i^\dagger x_j + x_j^\dagger x_i - x_i x_j - x_i^\dagger x_j^\dagger + (a \to b, x \to y) + (a \to c, x \to z) \Big\}. \tag{6.19}$$

As we see in (6.19) only one flavour of triplons may interact on each bond. Combined with the hard-core constraint this fact makes the hopping terms in (6.19) irrelevant. Thus, we are left with the Hamiltonian

$$H_{\text{dimer}} = \lambda \sum_i n_i^t - K \sum_{\langle ij \rangle a} x_i^\dagger x_j^\dagger - K \sum_{\langle ij \rangle b} y_i^\dagger y_j^\dagger - K \sum_{\langle ij \rangle c} z_i^\dagger z_j^\dagger + \text{h.c.}, \quad (6.20)$$

describing multi-flavoured excitonic dimers. The resulting Hilbert space is now reduced, which allows us to continue the exact diagonalization studies with a $N_{\text{sites}} = 24$ cluster.

Fig. 6.5(a) demonstrates the growth of the triplon density with K, which makes it conceptually different from the vacuum area restricted by the white dots (with $\sim$ zero triplon density). Our numerical studies provide a unique gapped ground state and no indications for bond order. One can demonstrate that the system is more robust against Γ perturbations than the Kitaev spin-liquid. Thus, by analogy with the spin-liquid, we observe the '*triplon liquid*', which emerges according to the order-by-disorder mechanism [156] driven by quantum fluctuations. Some typical triplon configurations in this phase can be found in Fig. 6.5(b).

7

Topological excitations

In this Chapter we introduce topologically nontrivial states of matter and consider the excitonic model in the presence of a magnetic field. We find topologically nontrivial triplon bands, calculate the corresponding Chern numbers, thermal Hall conductivity and classify topological states for different regimes of our theory.

7.1 General overview

The era of topological materials started with the *Integer Quantum Hall effect*, an experiment performed by von Klitzing, Dorda and Pepper [157]. They measured the transverse conductance of a two dimensional electron gas in strong magnetic fields and obtained an unexpected result: the Hall conductivity σ^{xy} instead of being a non-trivial function, was quantized (the Hall plateau), robust and given by an elegant expression

$$\sigma^{xy} = -C\frac{e^2}{h}, \tag{7.1}$$

where C is an integer, which was identified as a topological invariant [158].

As we mentioned before, topological effects in bosonic systems are widely discussed in literature: photons [54–60], phonons [61–63], magnons

on pyrochlore [64–66], kagome [67–76], honeycomb [77–87] lattices and topologically nontrivial triplon bands [88–90]. In contrast to electronic systems, triplon edge modes cannot be probed by doping, since they are electrically neutral and are not affected by any voltage. Therefore, for detecting edge modes in such systems the thermal Hall effect is used [94]. Originally derived for magnons [95], this scheme is valid for triplons as well [88, 89].

7.2 Theoretical remarks

The essence of the topological band theory is the *Berry phase* [159], acquired through the adiabatic (with respect to other energy scales) transport of the system along a path in the parameter space. Following [160], we consider a Hamiltonian $H(\mathbf{R})$, where $\mathbf{R} = (R_1, R_2, \dots)$ is a parameter vector, providing a time dependency of H. We choose a path $\mathcal{C}$ (in parameter space), describing the adiabatic evolution of $\mathbf{R}$. We suppose that the instantaneous orthonormal eigenbasis of H is known and is given by

$$H(\mathbf{R})|n(\mathbf{R}\rangle = E_n(\mathbf{R})|n(\mathbf{R}\rangle. \tag{7.2}$$

One starts with an initial state $|n(\mathbf{R}(0))\rangle$ and lets $\mathbf{R}(t)$ vary slowly. The initial state now evolves with $H(\mathbf{R})$ and remains its instantaneous eigenstate but it can acquire a non-zero phase $\theta(t)$ and then dynamics of the state $|\Psi(t)\rangle = e^{-i\theta(t)}|n(\mathbf{R}(t))\rangle$ is given by

$$H(\mathbf{R}(t))|\Psi(t)\rangle = i\hbar\frac{d}{dt}|\Psi(t)\rangle, \tag{7.3}$$

which yields

$$E_n(\mathbf{R}(t))|n(\mathbf{R}(t))\rangle = \hbar\Big[\frac{d}{dt}\theta(t)\Big]|n(\mathbf{R}(t))\rangle + i\hbar\frac{d}{dt}|n(\mathbf{R}(t))\rangle, \quad | \quad \times\langle n(\mathbf{R}(t))|$$

$$E_n(\mathbf{R}) - i\hbar\Big\langle n(\mathbf{R}(t))\Big|\frac{d}{dt}\Big|n(\mathbf{R}(t))\Big\rangle = \hbar\frac{d}{dt}\theta(t). \tag{7.4}$$

Solving the differential equation one obtains

$$|\Psi(t)\rangle = \exp\Big\{\frac{1}{\hbar}\int_0^t E_n(\mathbf{R}(t'))dt'\Big\}\exp(i\gamma_n)|n(\mathbf{R}(t))\rangle \tag{7.5}$$

where the Berry phase is defined as

$$\gamma_n = i\int_0^t \Big\langle n(\mathbf{R}(t'))\Big|\frac{d}{dt'}\Big|n(\mathbf{R}(t'))\Big\rangle dt', \tag{7.6}$$

or with the explicit time-dependence excluded

$$\gamma_n = i\int_0^{t_{\text{end}}} \langle n(\mathbf{R}(t'))|\nabla_{\mathbf{R}}|n(\mathbf{R}(t'))\rangle\frac{d\mathbf{R}}{dt'}dt' = i\int_{\mathcal{C}}\langle n(\mathbf{R}(t'))|\nabla_{\mathbf{R}}|n(\mathbf{R}(t'))\rangle d\mathbf{R}. \tag{7.7}$$

This phase manifests that two states separated by the time interval dt are not identical. Geometrical similarities with the electromagnetic field allow us to introduce the vector-potential analogue, called *Berry connection*

$$\mathbf{A}_n(\mathbf{R}) = i\langle n(\mathbf{R}(t'))|\nabla_{\mathbf{R}}|n(\mathbf{R}(t'))\rangle, \quad \Rightarrow \quad \gamma_n = \int_{\mathcal{C}} d\mathbf{R}\,\mathbf{A}_n(\mathbf{R}), \tag{7.8}$$

and the corresponding anti-symmetric tensor, called *Berry curvature*

$$\Omega_n^{\mu\nu} = \frac{\partial}{\partial R^\mu}A_{n,\nu}(\mathbf{R}) - \frac{\partial}{\partial R^\nu}A_{n,\mu}(\mathbf{R}). \tag{7.9}$$

It can be shown [160] that when the Fermi level lies in the gap, the integer C from (7.1) is given by

$$C_n = \frac{1}{2\pi}\int_{BZ} d^2k\,\Omega_n^{xy}(\mathbf{k}), \tag{7.10}$$

where n corresponds to a filled n^{th} band.

The Berry curvature $\Omega_n^{\mu\nu}$ may be associated with a magnetic field in the parameter space. This analogy prompts the application of Stoke's theorem to the circulation of the **A**-field, i.e. to the Berry curvature. The Brillouin zone is a torus and does not have any boundary, which gives $\sigma^{xy} = 0$. However, experiments reveal non-zero conductance. This 'contradiction' reminds that in some cases Stoke's theorem is inapplicable. Namely, it resembles a situation, when the corresponding vector-potential is not defined within its complete domain, here represented by the Brillouin zone. Therefore, there exists no gauge, which could yield a continuous and single valued **A** within the Brillouin Zone. This *obstruction* of the Stoke's theorem is manifested by a non-zero Chern number[1, 2].

There is another representation of the Berry curvature, which is especially useful for numerical simulations [160]

$$\Omega_n^{xy}(\mathbf{k}) = 2 \sum_{m \neq n} \mathrm{Im} \frac{\langle n \left| \frac{\partial H}{\partial k_x} \right| m \rangle \langle m \left| \frac{\partial H}{\partial k_y} \right| n \rangle}{(\omega_n - \omega_m)^2}, \tag{7.11}$$

where ω_n denotes the n^{th} eigenvalue of H.

For detecting topologically nontrivial triplonic bands, we need the thermal Hall conductivity, which consists of two parts [81], originating from the current density [67] and from the orbital motion [163, 164] and reads as

$$\kappa^{xy} = \kappa_1^{xy} + \kappa_2^{xy} = -\frac{k_B^2 T}{(2\pi)^2 \hbar} \sum_n \int_{BZ} d^2k \, c_2[\rho_i] \Omega_{n,xy}(\mathbf{k}), \tag{7.12}$$

[1] This also resembles having a magnetic monopole [161], since there is a non-zero "magnetic" flux coming out from a closed surface

[2] It is an illustrative description of the Chern number, sufficient for a qualitative understanding of the topological degree of freedom. A more mathematical explanation can be found, for example in [162]

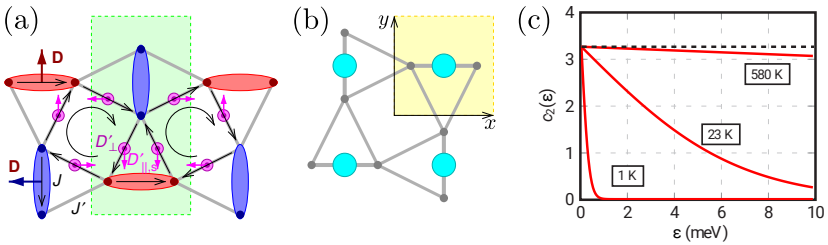

Figure 7.1.: Taken from [88]. (a) The $SrCu_2(BO_3)_2$ and corresponding interactions. (b) New unit cell obtained by a transformation, which uses the equivalence of two dimers within the yellow square. (c) Thermal coefficient $c_2[x]$ at different temperatures.

where $c_2[x]$ is a thermal coefficient (see Fig. 7.1(c))

$$c_2[x] = \int_0^x \ln^2 \frac{1+t}{t}\, dt = (1+x)\ln^2 \frac{1+x}{x} - \ln^2 x - 2\,\mathrm{Li}_2(-x), \quad (7.13)$$

with $\mathrm{Li}_2(-x)$ a *dilogarithm* or *Spence's* function [165].

7.3 Triplon Hall effect in $SrCu_2(BO_3)_2$

A prominent realization of the triplon Hall effect was proposed for a frustrated quantum magnet $SrCu_2(BO_3)_2$ [88] described by a Shastry-Sutherland model [91]. This material has a gapped dimer-singlet ground state, while excitations are of a triplet nature. The authors included symmetry allowed small Dzyaloshinskii-Moriya anisotropic interactions [92, 93] and a small magnetic field perpendicular to the $SrCu_2(BO_3)_2$

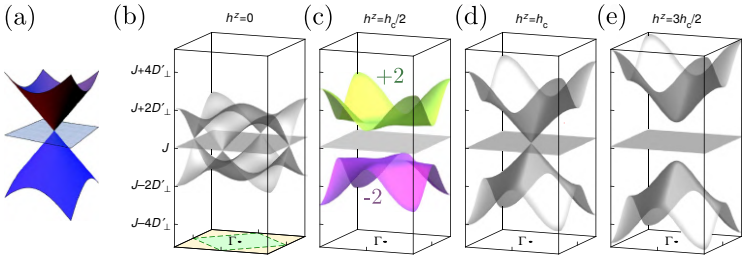

Figure 7.2.: Taken from [88] (a) Three bands touching, which forms a spin-1 Dirac cone. (b) Triplon bands in zero field. The bottom surface represents the Brillouin zone, which is enlarged due to a unitary transformation Brillouin Zone (compared to the green area, see text). (c)-(e) triplon bands for different values of h^z. One can see (d) that at $h = h_c$ the bands touch at the Dirac cone at Γ and remain trivial for $h > h_c$.

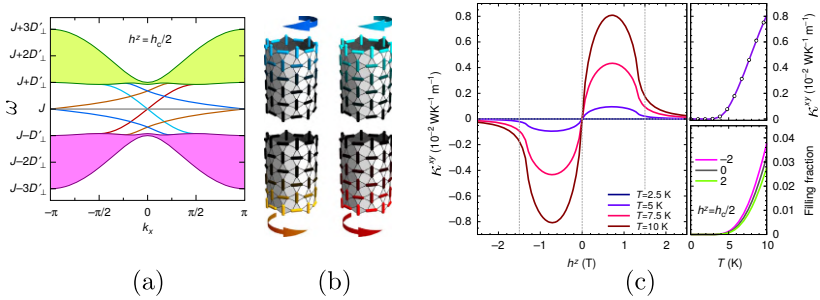

Figure 7.3.: From [88]. (a) Triplon bands on a cylindrical strip and corresponding edge modes. (b) Wave functions of the edge states. The color reflects a triplon weight. Right-(left-) movers reside on the bottom (top) edge. (c) Thermal Hall conductivity as a function of magnetic field (left) and temperature (right).

plane. The complete Hamiltonian then reads as

$$\mathcal{H} = J\sum_{\langle ij\rangle}\mathbf{S}_i\mathbf{S}_j + J'\sum_{\langle\langle ij\rangle\rangle}\mathbf{S}_i\mathbf{S}_j - g_z h^z\sum_i S_i^z + \sum_{\langle ij\rangle}\mathbf{D}_{ij}(\mathbf{S}_i\times\mathbf{S}_j) + \sum_{\langle\langle ij\rangle\rangle}\mathbf{D}'_{ij}(\mathbf{S}_i\times\mathbf{S}_j), \tag{7.14}$$

where $\langle\langle ij\rangle\rangle$ refers to next-nearest neighbours. Introducing the bond operator formalism [133], one can express this model in terms of triplons and thus obtain a 6×6 Hamiltonian matrix in momentum space (three triplons on both blue and red dimers, see Fig. 7.1(a))[3]. Nevertheless, if the magnetic field is parallel to the z axis, one can find a unitary transformation, which makes the hoppings translationally invariant (see Fig. 7.1(b)) and therefore yields a 3×3 matrix:

$$\mathcal{H} = \sum_{\mathbf{k}}\sum_{\mu,\nu=x,y,z}\tilde{t}^\dagger_{\mu,\mathbf{k}}M_{\mu\nu}(\mathbf{k})\tilde{t}_{\nu,\mathbf{k}}, \tag{7.15}$$

where

$$M(\mathbf{k}) = \begin{pmatrix} J & ih^z g_z + 2iD'_\perp\gamma_3 & \tilde{D}_\parallel\gamma_2 \\ -ih^z g_z - 2iD'_\perp\gamma_3 & J & -\tilde{D}_\parallel\gamma_1 \\ \tilde{D}_\parallel\gamma_2 & -\tilde{D}_\parallel\gamma_1 & J \end{pmatrix}, \tag{7.16}$$

with $\gamma_1 = \sin k_x$, $\gamma_2 = \sin k_y$ and $\gamma_3 = (\cos k_x + \cos k_y)/2$. Alternatively, this matrix can be rewritten as

$$M(\mathbf{k}) = J\cdot\mathbf{1} + \mathbf{d}(\mathbf{k})\cdot\mathbf{L} \tag{7.17}$$

$$\text{where}\qquad \mathbf{L} = \left[\begin{pmatrix}0&0&0\\0&0&-1\\0&-1&0\end{pmatrix}, \begin{pmatrix}0&0&1\\0&0&0\\1&0&0\end{pmatrix}, \begin{pmatrix}0&-i&0\\i&0&0\\0&0&0\end{pmatrix}\right] \tag{7.18}$$

$$\text{and}\qquad \mathbf{d}(\mathbf{k}) = \left[\tilde{D}_\parallel\gamma_1(\mathbf{k}), \tilde{D}_\parallel\gamma_2(\mathbf{k}), h^z g_z - 2D'_\perp\gamma_3(\mathbf{k})\right]. \tag{7.19}$$

[3]Here the pairing terms $t^\dagger t^\dagger$ are ignored, since they do not affect energies to linear order in D, D' and h^z [88]. This approximation is justified by an explicit verification.

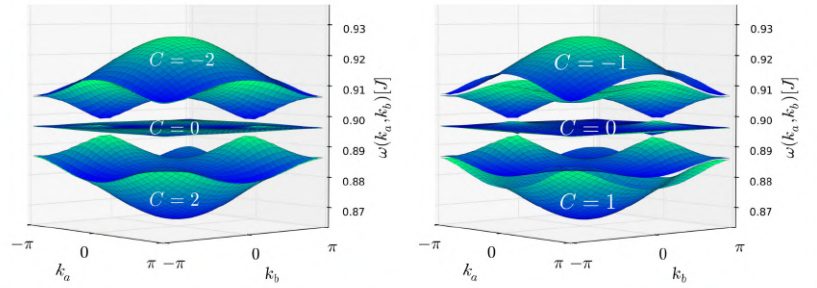

Figure 7.4.: From [89]. Two possible Chern number configurations, realizable within the extended Shastry-Sutherland model. On the left panel the magnetic field has one nonzero component h_z, whereas on the right one both h_x and h_z contribute.

Thus, $\mathbf{d}(\mathbf{k})$ represents a fictitious magnetic field, while $\mathbf{L}$ matrices satisfy the SU(2) algebra

$$[L^\mu, L^\nu] = i\varepsilon_{\mu\nu\alpha}L^\alpha. \tag{7.20}$$

The resulting Chern numbers can be interpreted as a winding number [166]

$$C = \frac{1}{4\pi}\int_{BZ} d\mathbf{k}\,\hat{\mathbf{d}}(\mathbf{k})\cdot\frac{\partial\hat{\mathbf{d}}(\mathbf{k})}{\partial k_x}\times\frac{\partial\hat{\mathbf{d}}(\mathbf{k})}{\partial k_y}, \tag{7.21}$$

where $\hat{\mathbf{d}}(\mathbf{k})$ is the normalized pseudo-magnetic field $\mathbf{d}(\mathbf{k})$.

It turns out that topologically nontrivial bands arise in magnetic fields $|h| \leq h_{\text{crit}}$. As it is shown in Fig. 7.2 the resulting Chern numbers are $C = 0, \pm 2$, which corresponds to a set of four edge states [167] illustrated in Fig. 7.3(a). The thermal Hall conductivity dependence on the magnetic field and temperature is given in Fig. 7.3(c).

Additionally, one can show [89] that an arbitrary field $\mathbf{h} = (h_x, h_y, h_z)$ applied to this system extends the above results to another configuration of the Chern numbers $C = 0, \ \pm 1$ (see Fig. 7.4).

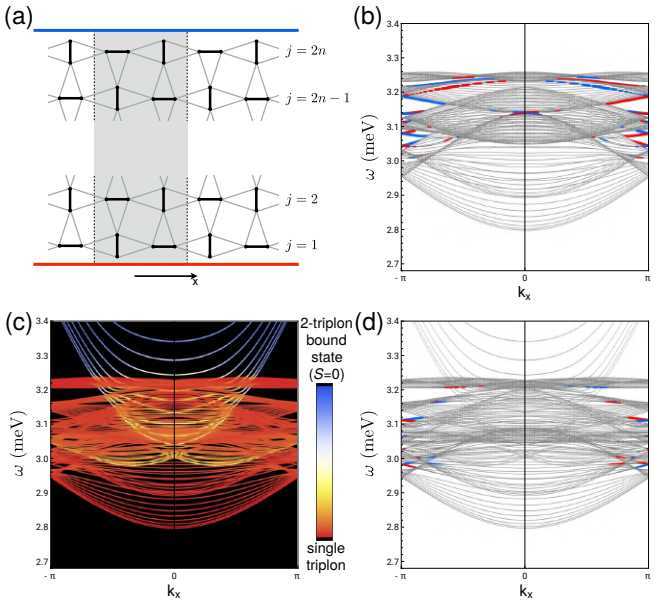

Figure 7.5.: (Taken from [90]) (a) Strip geometry of $SrCu_2(BO_3)_2$ used in edge mode simulations. (b) Excitation spectrum for $n = 20$. (c) Hybridization between the two-triplon bound state and the triplon modes and (d) the corresponding edge states.

7.4 Defining the regime

We consider the excitonic model deep in the paramagnetic phase $\lambda \gg A$, i.e. the darkest inner part of the diagram 6.2(a). It seems to be the most suitable case to start with, since it does not require any sophisticated transformations of the Hamiltonian caused by condensation phenomena. Following the above scenario we introduce a magnetic

field $\mathbf{h}$, which enters the Hamiltonian as

$$H_{\text{mag}} = \mu_B \mathbf{h} \sum_i \mathbf{M}_i, \tag{7.22}$$

where $\mathbf{M}_i = 2\mathbf{S}_i - \mathbf{L}_i$ is the magnetic moment

$$\mathbf{M}_i = -i\sqrt{6}(\mathbf{T} - \mathbf{T}^\dagger)_i + ig(\mathbf{T}^\dagger \times \mathbf{T})_i. \tag{7.23}$$

The Hamiltonian (7.22) diversifies the onsite interactions, represented solely by the spin-orbit coupling before. Furthermore, in previous Chapters the second term in (7.23) is ignored, since $\mathbf{S}$ and $\mathbf{L}$ operators do not contribute in (3.52) linearly, thus yielding $h^{(3)}$ and $h^{(4)}$ interactions, which are beyond the scope of this work. However, this term remains quadratic in triplons and becomes relevant if the magnetic field is introduced.

In contrast, linear terms in (7.23) are now suppressed and can be neglected (see Appendix E.2). Thus, setting $g = \frac{1}{2}$ [20] we get

$$M_x \simeq \frac{i}{2}(y^\dagger z - z^\dagger y), \quad M_y \simeq \frac{i}{2}(z^\dagger x - x^\dagger z), \quad M_z \simeq \frac{i}{2}(x^\dagger y - y^\dagger x).$$

The resulting Hamiltonian is given by

$$\begin{aligned}
H &= \lambda \sum_i \{n_i^x + n_i^y + n_i^z + \tilde{n}_i^x + \tilde{n}_i^y + \tilde{n}_i^z\} \\
&+ J \sum_{\langle ij \rangle} \{x_i^\dagger \tilde{x}_j + y_i^\dagger \tilde{y}_j + z_i^\dagger \tilde{z}_j + \text{h.c.}\} \\
&+ K \Big[\sum_{\langle ij \rangle a} x_i^\dagger \tilde{x}_j + \sum_{\langle ij \rangle b} y_i^\dagger \tilde{y}_j + \sum_{\langle ij \rangle c} z_i^\dagger \tilde{z}_j + \text{h.c.} \Big] \\
&+ \Gamma \Big[\sum_{\langle ij \rangle a} \{y_i^\dagger \tilde{z}_j + z_i^\dagger \tilde{y}_j\} + \sum_{\langle ij \rangle a} \{y_i^\dagger \tilde{z}_j + z_i^\dagger \tilde{y}_j\} + \sum_{\langle ij \rangle a} \{y_i^\dagger \tilde{z}_j + z_i^\dagger \tilde{y}_j\} + \text{h.c.} \Big] \\
&+ \mu_B \sum_i \Big[ih_x \big(y_i^\dagger z_i - z_i^\dagger y_i + \tilde{y}_i^\dagger \tilde{z}_i - \tilde{z}_i^\dagger \tilde{y}_i\big) + ih_y \big(z_i^\dagger x_i - x_i^\dagger z_i + \tilde{z}_i^\dagger \tilde{x}_i - \tilde{x}_i^\dagger \tilde{z}_i\big) \\
&+ ih_z \big(x_i^\dagger y_i - y_i^\dagger x_i + \tilde{x}_i^\dagger \tilde{y}_i - \tilde{y}_i^\dagger \tilde{x}_i\big) \Big],
\end{aligned} \tag{7.24}$$

where for the sake of convenience we drop out μ_B and the prefactor $1/2$ in front of the field (for a further intuitive feeling of the field strength one can justify that $h = 0.1$ corresponds to 1-2 Tesla, see Appendix F). Although, the pairing terms $T^{\dagger}_{\gamma,i}T^{\dagger}_{\gamma,j}$ enter in order $1/\lambda$ and are neglected (similar to the extended Shastry-Sutherland model [88]), we verified that including them does not affect the results (the complete Hamiltonian is given in Appendix E.1). Thus, by means of the Fourier transformation one obtains

$$\mathcal{H}(\mathbf{k}) = \sum_{\mathbf{k}} \Psi^{\dagger}_{\mathbf{k}} M(\mathbf{k}) \Psi_{\mathbf{k}}, \tag{7.25}$$

where

$$\Psi_{\mathbf{k}} = \begin{pmatrix} x_k & y_k & z_k & \tilde{x}_k & \tilde{y}_k & \tilde{z}_k \end{pmatrix}^T,$$

and the M-matrix is given by

$$\begin{pmatrix} \lambda & -ih_z & ih_y & J\epsilon_k + Ke^{ik_a} & \Gamma e^{ik_c} & \Gamma e^{ik_b} \\ ih_z & \lambda & -ih_x & \Gamma e^{ik_c} & J\epsilon_k + Ke^{ik_b} & \Gamma e^{ik_a} \\ -ih_y & ih_x & \lambda & \Gamma e^{ik_b} & \Gamma e^{ik_a} & J\epsilon_k + Ke^{ik_c} \\ J\epsilon_k^* + Ke^{-ik_a} & \Gamma e^{-ik_c} & \Gamma e^{-ik_b} & \lambda & -ih_z & ih_y \\ \Gamma e^{-ik_c} & J\epsilon_k^* + Ke^{ik_b} & \Gamma e^{-ik_a} & ih_z & \lambda & -ih_x \\ \Gamma e^{-ik_b} & \Gamma e^{-ik_a} & J\epsilon_k^* + Ke^{-ik_c} & -ih_y & ih_x & \lambda \end{pmatrix},$$

with $\epsilon_k = \sum_{\gamma} e^{ik_\gamma}$.

We numerically diagonalize the Hamiltonian (7.25), find the eigenvectors and evaluate Chern numbers (7.10) as integrals of the Berry curvature (7.11). The parameter space is defined by J, K (or alternatively by A and α), Γ and $\mathbf{h}$, while λ is supposed to be dominant and fixed. In order to classify all the possible scenarios carefully, we separate our investigations into several stages: we set the magnetic field orthogonal to the lattice ($\mathbf{h} \parallel (1,1,1)$), start with the Kitaev interaction then include the Heisenberg contribution and, as the last step, we verify which impact is provided by the cross-terms.

7.5 Kitaev coupling only

We start exploring nontrivial topological properties of the excitonic model (7.25) with the simplest case $J = 0,\ \Gamma = 0,\ K \neq 0$. In this regime triplon bands are threefold degenerate and completely flat (see for example Eq. (5.17) and Fig. 5.1(d)). Remarkably, even without applying magnetic fields we observe so-called *end states*, which can be attributed to a topological origin [169] related to the Zak phase [170] and to topological end states in a Su-Schrieffer-Heeger chain [168]. The latter we use labelling our end states with 'SSH end modes' in Fig. 7.6(d). The origin of these states can be explained as follows. In the pure Kitaev regime each flavour of triplons $\mathbf{T}$ can move along its 'own' direction, i.e. along a given flavour-associated bond. If we consider a semi-infinite system with zigzag boundaries, one kind of bonds is cut, e.g. the zz-bonds in Fig. 7.6(c). Thus, the z-boson becomes isolated and resides on the edges with the energy λ instead of $\lambda \pm K$.

The band degeneracy can be lifted by a finite magnetic field inducing onsite flavor transitions (see Fig. 7.6)[4]. A probe field $\mathbf{h} = (0.3, 0.3, 0.3)$ leads to the Chern number configuration $\mathcal{C} = \{-1, 0, 1, -1, 0, 1\}$[5] (from bottom to top) and to the corresponding edge modes illustrated in Fig. 7.6(b).

Now we determine an appropriate field strength interval, in which topologically nontrivial bands can arise, and seek corresponding critical values h_c. In Fig. 7.7(a) one finds the Chern numbers as functions of the field magnitude h. In total, we observe three different Chern number sets at different field strengths: $\mathcal{C} = \{-1, 0, 1\}$, $\mathcal{C} = \{-1, 0, 0\}$ and $\mathcal{C} = \{-1, 1, -1\}$, and the sign of h only flips the Chern numbers within

[4]The model becomes equivalent to a decorated honeycomb lattice, which possesses topologically nontrivial bands as well [171].

[5]In what follows we provide only three first integers, since the other ones are defined by the relation $C_{6-i+1} = -C_i,\ i \leq 3$.

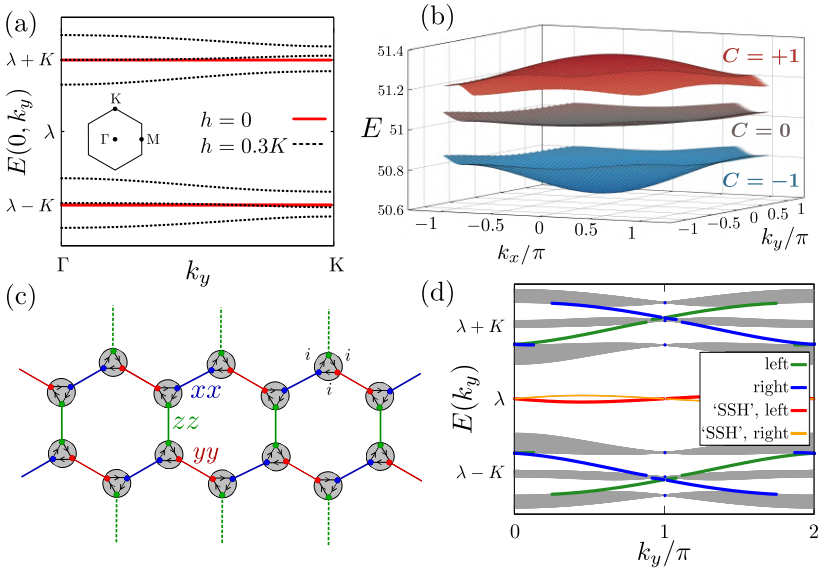

Figure 7.6.: (a) Triplon bands in the pure Kitaev case $\alpha = 90°$. In absence of fields we observe degenerate flat bands (red lines). A finite magnetic field lifts the degeneracy and makes the bands dispersive (black dotted lines). (b) A 3D plot of these dispersive bands (the upper three) labelled with acquired Chern numbers. (c) A decorated honeycomb lattice, reflecting the onsite transformations of triplons allowed by the field. Green dashed lines represent bond cuts made for formation of the zigzag edges generating end modes. (d) Nontrivial bands with edge states obtained for a cylinder along zigzag edges. "SSH" denotes the Su-Schrieffer-Heeger chain-like end states [168].

the given configuration. Since topological indices of the bands are robust with respect to adiabatic changes of the system, any given configuration remains unchanged, while gaps are open. Therefore, vertical lines[6] presumably manifest the gap closings. Indeed, in Fig. 7.7(b)-(c) we can see that in both cases bands touch at the vector $\mathbf{\Gamma} = (0, 0)$.

In order to define threshold fields, we consider the Hamiltonian (7.25) at the fixed momentum $\mathbf{k} = \mathbf{\Gamma}$ [172]. Mathematically λ defines the relative energy level of the bands and does not change their structure, hence for the sake of simplicity we can set $\lambda = 0$. Under these assumptions the eigenvalues can be expressed analytically

$$E_{2,5}(\alpha = 90^\circ)\Big|_{\mathbf{\Gamma}} = \pm K, \tag{7.26}$$

$$E_{3,4}(\alpha = 90^\circ)\Big|_{\mathbf{\Gamma}} = \pm\big(K - h\sqrt{3}\big), \tag{7.27}$$

$$E_{1,6}(\alpha = 90^\circ)\Big|_{\mathbf{\Gamma}} = \pm\big(K + h\sqrt{3}\big), \tag{7.28}$$

where indices reflect the energies sorting. In Fig. 7.7(a) we see that the first rearranging of the Chern numbers concerns C_3 and C_4 only, hence only two middle bands touch at $\mathbf{\Gamma}$, i.e. $E_3 = E_4$, which gives

$$K - h\sqrt{3} = 0, \qquad \Rightarrow \qquad \frac{h}{K} = \frac{1}{\sqrt{3}} \simeq 0.577. \tag{7.29}$$

The second change takes place for the pairs $(C_2,\ C_3)$ and $(C_4,\ C_5)$, which corresponds to $E_2 = E_3$ or $E_4 = E_5$, yielding

$$2K - h\sqrt{3} = 0, \qquad \Rightarrow \qquad \frac{h}{K} = \frac{2}{\sqrt{3}} \simeq 1.155. \tag{7.30}$$

The obtained threshold fields h/K agree with the singularities in Fig. 7.7(a). Furthermore, the triplon bands remain nontrivial for $h > 2K/\sqrt{3}$, and our calculations indicate that topologically nontrivial character of the bands persists for the limit of large magnetic fields. Let us

[6] Ideally vertical, i.e. for the step $\delta h \to 0$.

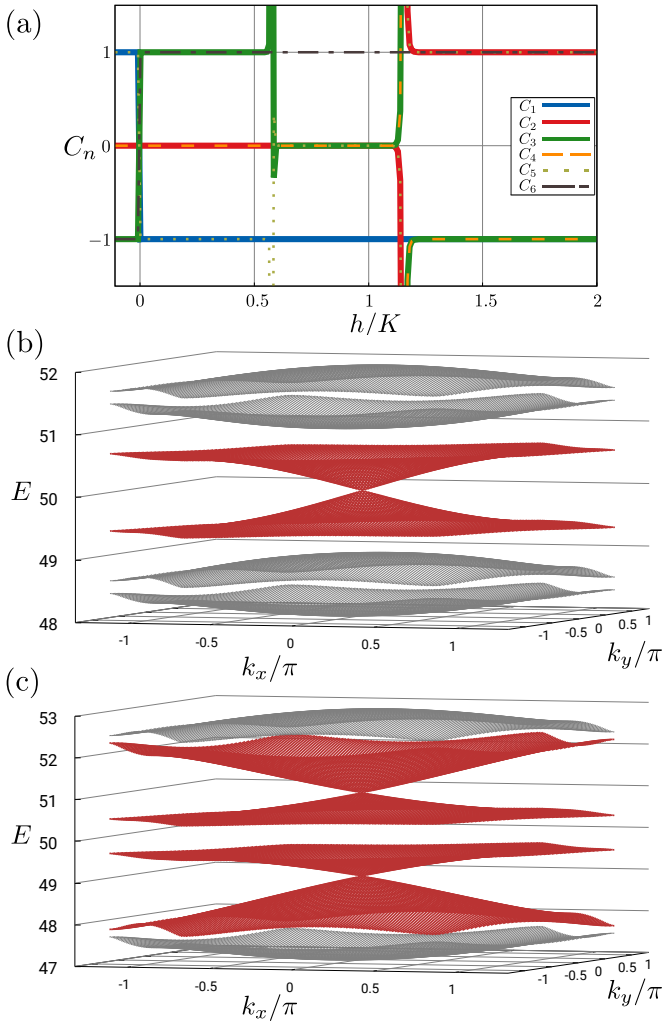

Figure 7.7.: (a) Band Chern numbers C_n versus the applied magnetic field magnitude h (in units of K). We observe three unique configurations of C_n. (b),(c) Bands touchings at the $\mathbf{\Gamma}$-point for $h \simeq 0.577K$ and $h \simeq 1.155K$ correspondingly. These gap closings indicate singularities of the Chern numbers, given in (a).

see, how the Heisenberg contribution affects the topologically nontrivial excitations of the Kitaev regime.

7.6 J-K topological 'phase diagram'

Using the standard polar representation of the parameter space $A = \sqrt{J^2 + K^2}$, $\tan\alpha = K/J$ and calculating the band Chern numbers (7.10) as functions of $h \in [0, 1.5A]$ and $\alpha \in [0°, 180°]$ (due to the $\alpha \to \alpha + 180°$ invariance of the model, the second half $\alpha \in [180°, 360°]$ provides equivalent results, see also the exact diagonalization results), we get a topological 'phase diagram', given in Fig.7.8. It is intriguing that the whole parameter space is covered by different topological 'phases', except the pure Heisenberg regime $\alpha = 0°,\ 180°$, where no gaps are open. Ideally.

It is very important to clarify that the numerical origin of these results produces uncertainties in describing the topological properties of the bands. Apart from the question, how many decimal points are needed to consider numerically real Chern numbers as integers, we have another one to answer. If we consider a finite 500×500 system, it provides 250000 available momentum points. Thus, the fact that the gaps close can be ascertained only up to a given precision, since the bands touching can happen not only at the $\mathbf{\Gamma} = (0, 0)$ but, for example, at $\mathbf{k} = \mathbf{M} = (0, \pm 2\pi/\sqrt{3})$, whose exact value has to be found among the accessible $\mathbf{k}$-points in order to yield $\omega_n(\mathbf{M}) - \omega_{n\pm1}(\mathbf{M}) = 0$ exactly. This situation is very improbable. Therefore, in our simulations we define a *numerical zero*[7] as $0 \simeq |\omega_n(\mathbf{k}) - \omega_{n\pm1}(\mathbf{k})| \leq A \cdot 10^{-8}$.

However, for a finite field h the diagram should be covered completely (except the pure Heisenberg regimes). We consider the Hamil-

[7] Additionally, this 'filter' rejects divergences while calculating the Berry curvature (7.11).

tonian (7.25) at $\mathbf{k} = \mathbf{\Gamma}$ and obtain the following eigenvalues

$$E_{2,5}(\alpha)\Big|_{\mathbf{\Gamma}} = \pm A(3\cos\alpha + \sin\alpha), \tag{7.31}$$

$$E_{3,4}(\alpha, h)\Big|_{\mathbf{\Gamma}} = \pm\big(3A\cos\alpha + A\sin\alpha - h\sqrt{3}\big), \tag{7.32}$$

$$E_{1,6}(\alpha, h)\Big|_{\mathbf{\Gamma}} = \pm\big(3A\cos\alpha + A\sin\alpha + h\sqrt{3}\big). \tag{7.33}$$

Thus, varying these energies with respect to α and h we define all possible gap closings at the $\mathbf{\Gamma}$ vector. The resulting phase transitions are given in red in Fig. 7.9(a).

Apart from $\mathbf{k} = \mathbf{\Gamma}$ we investigate (7.25) at fixed $\mathbf{k} = \mathbf{M}$ and $\mathbf{k} = \mathbf{K}$ as well. The resulting parameter space defining bands touching is depicted in Fig. 7.9(a) with green and blue correspondingly. Moreover, one can take a larger system, increase precision of the numerical zero and look for other touching points at the first Brillouin zone around the phase boundaries, given in Fig. 7.8. These simulations provide no new phase transitions.

Therefore, if our definition of the numerical zero is greater than the gaps, the bands become *numerically merged* and we classify them with a new set of topological characters and fill the empty spaces of the ideally complete diagram. Summarizing, the merged phases indicate a parameter subspace, where the gaps are extremely small.

We observe three merging channels and instead of the configuration $\{C_1, C_2, C_3\}$ (black-and-white label with curly brackets in Fig. 7.8) the merged sectors are described either by $\{C_1 + C_2, C_3\}$ (red and curly) or $[C_1, C_2, C_3 + C_4]$ (labelled blue with three numbers and square brackets) or $[C_1 + C_2, C_3 + C_4]$ (two numbers in blue). One can see that the resulting topological characters are in consonance with the 'standard' neighbouring phases.

It turns out that $\mathbf{h} \parallel (1, 1, 1)$ is the only field inducing nontrivial topology of the bands in the (J, K) parameter space. Thus, we take

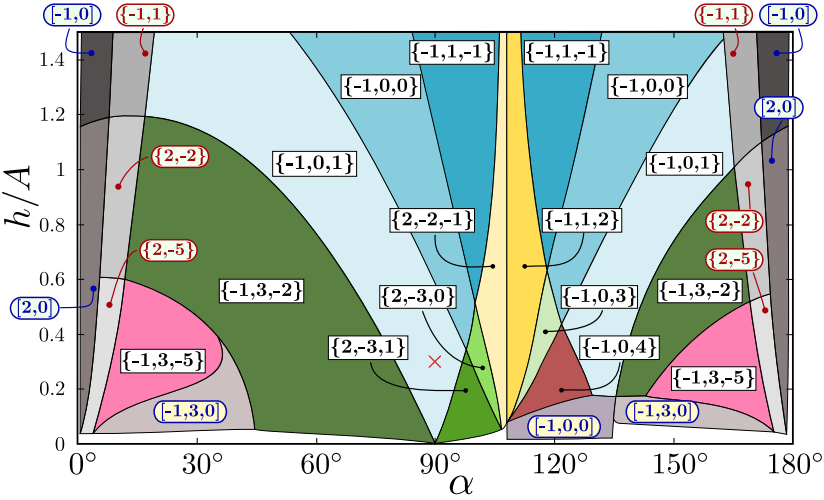

Figure 7.8.: Topological 'phase diagram', which illustrates all existing phases within the complete parameter space. Colours sort the phases with respect to the highest Chern number emerged: blue stands for $|C_n^{\max}| = 1$, yellow for 2, green for 3, red for 4 and pink for 5. Shades of gray highlight the so-called 'merged' phases (see text). Curly brackets represent phases with an even number of bands (four or six), while square ones indicate the phases, where the middle gap is closed, yielding an odd total number of bands. The red cross corresponds to $\alpha = 90°$, $h = 0.3K$ given in Fig. 7.6.

cross-terms into consideration and verify, whether they do not make band gaps trivial and whether other field directions lead to topologically nontrivial excitations.

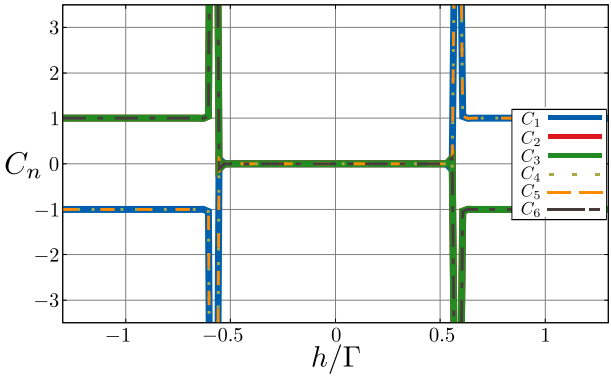

Figure 7.10.: Band Chern numbers in the $J = K = 0$, $\Gamma \neq 0$ regime. One can notice that choosing the opposite magnetic field direction leads to a sign flipping of C_n.

7.7 On the cross-terms contribution

We continue our investigations and consider the complete model (7.25). The resulting parameter space becomes too large to classify topological phases carefully and to provide an adequate phase diagram. However, Γ-terms are typically smaller than J or K, hence we can merely find out, whether the topological variety from Sec. 7.6 is robust against Γ-perturbations, and if so, how it changes the diagram 7.8.

We start with keeping the cross-terms only. The corresponding band Chern numbers are illustrated in Fig. 7.10. The pure Γ-regime itself hosts topologically nontrivial bands. In contrast to the Kitaev regime, there is a critical field $h_c = \Gamma/\sqrt{3}$ and only one phase $\{-1, 1, -1\}$ occurs

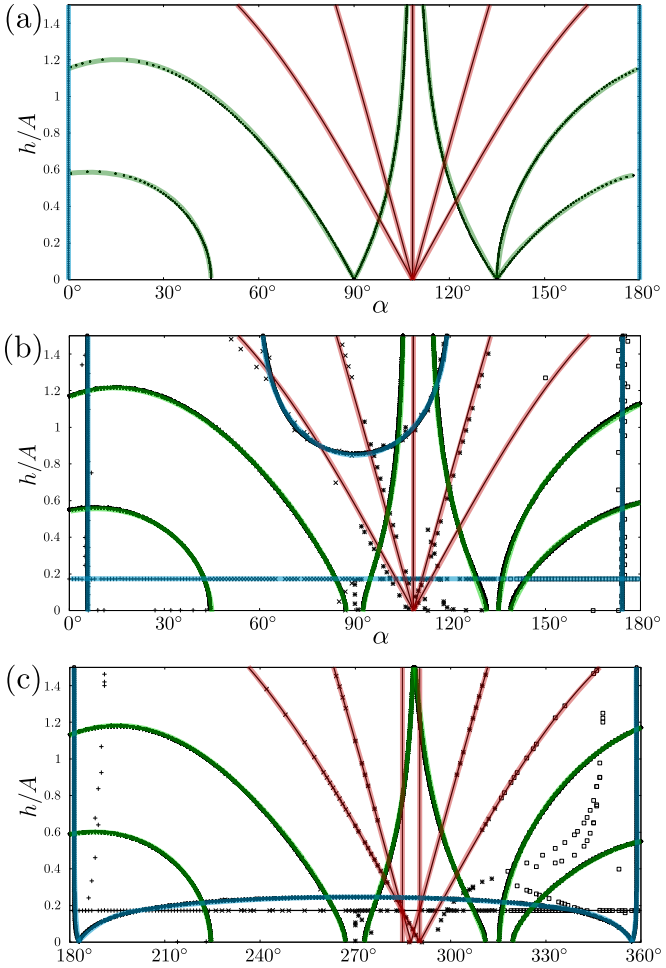

Figure 7.9.: Topological phase transitions evaluated numerically for exact values of $\mathbf{k}$ for (a) $\Gamma = 0$ and (b), (c) $\Gamma = 0.1\,A$. The red lines indicate bands touching at the $\mathbf{\Gamma}$ vector, green ones at $\mathbf{k} = \mathbf{M}$ and blue ones at $\mathbf{k} = \mathbf{K}$. Nonhighlighted points refer to gaps closings at any of remaining momentum points obtained by a higher precision tests, based on explicit minimization of the band gaps within the complete first Brillouin zone.

for $h > h_c$. By analogy with the previous sections one fixes $\mathbf{k} = \mathbf{\Gamma}$ and obtains the eigenvalues of (7.25)

$$E_{2,5} = \pm(2G + 3A\cos\alpha + A\sin\alpha), \tag{7.34}$$

$$E_{3,4} = \pm\big(G - 3A\cos\alpha - A\sin\alpha + h\sqrt{3}\big), \tag{7.35}$$

$$E_{1,6} = \pm\big(G - 3A\cos\alpha - A\sin\alpha - h\sqrt{3}\big), \tag{7.36}$$

where G refers to the cross-terms coupling avoiding confusion with $\mathbf{\Gamma} = (0,0)$. Putting $A = 0$ one finds gaps closing at $h_c = \Gamma/\sqrt{3}$.

Now we set $\Gamma = 0.1A$, repeat the calculations from 7.6 with $\alpha \in [0°, 360°]$ and end up with a diagram, given in Fig. 7.11. In order to make it readable, we separate it into two parts, which both for $\Gamma = 0$ reproduce the results of Fig. 7.8. Furthermore, one can show that a sign flip of Γ exchanges these two halves.

Remarkably, the cross-terms provide more freedom in choosing the magnetic field direction. For example, Fig. 7.12 demonstrates a topological 'phase diagram' corresponding to the field $\mathbf{h} \parallel (0,0,1)$. Although the diagram structurally differs from that of $\mathbf{h} \parallel (1,1,1)$, it is still completely covered with different topological regimes of the bands.

Our simulations indicate that only in presence of in-plane fields the bands become topologically trivial[8].

[8]The question whether it concerns all in-plane directions is open [172]. Thus, a more detailed analysis is required.

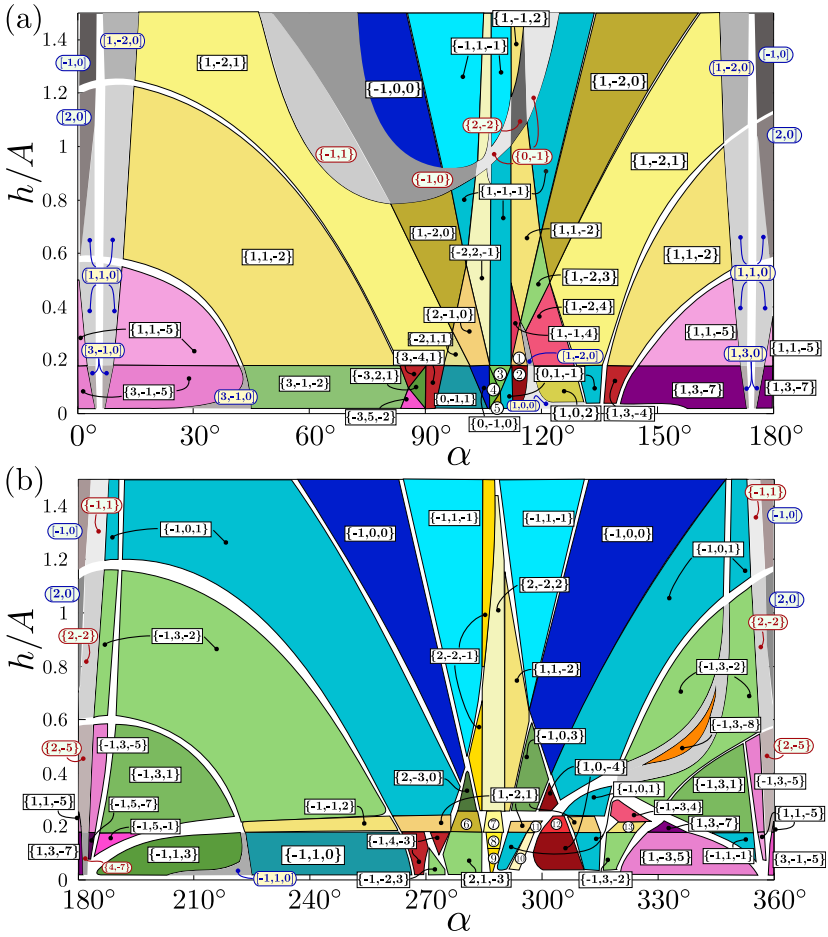

Figure 7.11.: Topological 'phase diagram' given in the h/A - α parameter space for $\Gamma = 0.1A$ and $\mathbf{h} = (h, h, h)$. These two diagrams exchange their α parameter subspaces under a Γ sign flip.

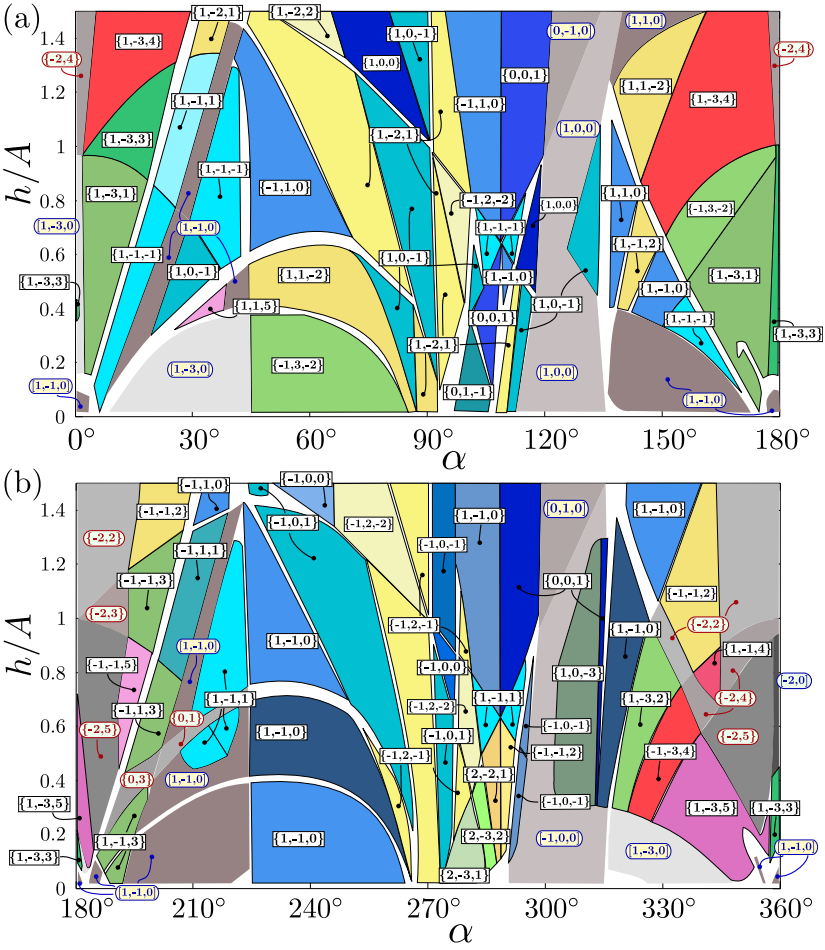

Figure 7.12.: Topological 'phase diagram' given in the h/A - α parameter space for $\Gamma = 0.1A$ and $\mathbf{h} = (0, 0, h)$.

7.8 Thermal Hall effect and real units in the excitonic model

In previous sections we expressed magnetic field strength in energy units (meV)[9]

$$h = -\frac{1}{2}\mu_{\mathrm{B}}\,\tilde{h}, \tag{7.37}$$

where $\tilde{h}$ represents the field in Tesla. In our calculations 10T corresponds to $h \sim 0.3\,\mathrm{meV}$. At first glance, accessible fields can lead to topologically nontrivial triplon bands. Nevertheless, we plotted topological 'phase diagrams' with respect to h/A. For $4t^2/U \sim 50\,\mathrm{meV}$ one obtains $A \sim 10\,\mathrm{meV}$. Therefore, a 10T field reads as $h/A \sim 0.03$.

Thus, we provide thermal conductivity plots in arbitrary units without implying any unrealistic fields $h/A \sim 1$, see Fig. 7.13.

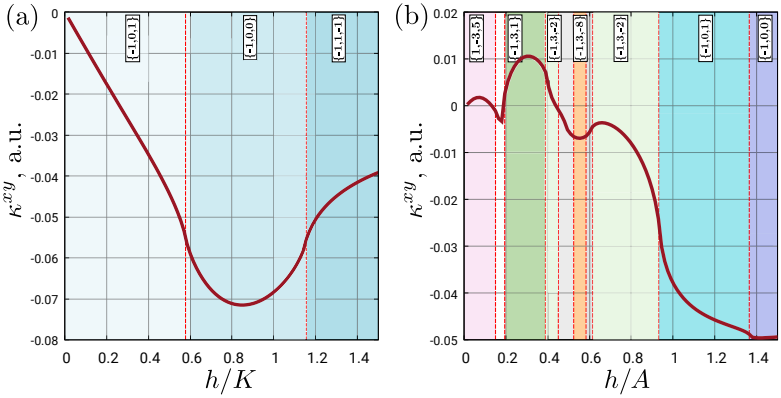

Figure 7.13.: Thermal Hall conductivity κ^{xy} vs. the magnetic field magnitude h for (a) $J = \Gamma = 0$, $K \neq 0$, (b) $\Gamma = 0.1A$, $\alpha = 340°$. Colours correspond to those of the diagrams.

[9] All estimations can be found in Appendix F.

8

Summary and Outlook

Based on [20] we considered d^4 Van-Vleck-type Mott insulators with the strong spin-orbit coupling for edge-shared bonding geometry. We included the direct exchange interaction and derived an extended effective excitonic model on the honeycomb lattice. The interaction picture of triplons appears to be similar to the spin-1/2 Kitaev-Heisenberg model, i.e. full-flavour Heisenberg-like contribution competes with the anisotropic bond-dependent one. This allows us to provide a direct comparison of these two 'cousin' models.

In Chapters 2, 3 we discussed standard tools and notions used in the relevant literature. We used them considering Mott insulators in the strong spin-orbit coupling and provided an illustrative derivation of the spin-1/2 Kitaev-Heisenberg model. We focused on Van-Vleck ions and on the mechanism of the excitonic magnetism in d^4 systems. Consequently, we included the direct exchange, derived the Kitaev-Heisenberg excitonic model and thus extended the results of [20]. The triplonic Hamiltonian appeared to be reminiscent of [15], where apart from the Heisenberg and Kitaev interactions, the cross-terms anisotropic exchange takes place.

In Chapter 4 we investigated the model on the classical level. For the sake of simplicity we excluded the cross-terms contribution and analogously to [12] we introduced polar coordinates in the parameter

space $(J, K) \to (A, \alpha)$. In the classical limit the excitonic and the conventional Kitaev-Heisenberg models are argued to behave alike, hence within the classical analysis we preset in the excitonic model orderings occurring in the $J = 1/2$ Kitaev-Heisenberg one and calculated the corresponding classical energies per site. These energies depend on the condensate densities ρ, since the magnetism within the excitonic paradigm is driven by the condensation of triplons. Minimization of the classical energies with respect to ρ provided a critical value of the interaction magnitude A_{cr} as a function of the spin-orbit coupling constant λ and the couplings tuning angle α. In other words, A_{cr} estimates the minimal energy (with respect to λ) needed for a triplon condensation for each J/K ratio.

Varying the classical energies of the triplons in the complete parameter space we defined the lowest ones and α-intervals, where each of these ground state configurations arose. Based on these results, we established the first proposal for a magnetic (J, K) phase diagram. The main difference compared to the conventional Kitaev-Heisenberg model is represented by a new paramagnetic sector $A < A_{\mathrm{cr}}(\alpha)$, where no condensate is formed and hence no ordering is present.

The initial guess we verified by means of Markov Chain Monte-Carlo simulations without prescribing any familiar orderings. We rewrote the triplonic Hamiltonian $H(\mathbf{T}, \mathbf{T}^\dagger)$ in the equivalent dipolar representation $H(\mathbf{v})$ with $\mathbf{v} = -i(\mathbf{T} - \mathbf{T}^\dagger)/2$, and treated the $\mathbf{v}$-vectors as real space ones. We showed that including the condensate degree of freedom gives rise to a nontrivial longitudinal behaviour of the $\mathbf{v}$-vectors, namely the tendency $|\mathbf{v}| \to 0$ for small couplings $A < A_{\mathrm{cr}}$. The initial lengths and orientations of the vectors were chosen randomly and were optimized by the Metropolis algorithm based MCMC with respect to the energy gain. For the complete parameter space, we obtained real space configurations of the vectors and spin structure factors in the first Brillouin Zone. The resulting classical phase diagram exactly reproduced the pre-

vious one and shed light on the ground state of [20], which is given by independent one-dimensional AF zigzag chains and manifests a phase transition between Stripy and AF orderings.

In Chapter 5 we carried out linear spin-wave calculations for the hard-core bosons and defined the excitation spectra of the model in the paramagnetic phase. These studies determined the paramagnetic parameter space and reproduced the results predicted by classical methods. Furthermore, we indicated the excitation dispersions in the ordered phases demonstrating the gapped Higgs amplitude and the gapless Goldstone modes.

In Chapter 6 we used exact diagonalization technique and obtained the quantum phase diagram of the model. It reflects the paramagnetic and the ordered phases, confirms and supplements the classical results, which cannot treat quantum fluctuations. In particular, the original excitonic model represents a first order phase transition.

Furthermore, in the Kitaev spin-liquid sector we found a new order-by-disorder 'triplon liquid' phase. In addition to the vacuum, the ground state in the pure Kitaev regime is represented by configurations, where only pairs of triplons occupy their corresponding bond sites. Thus, we restricted the Hilbert space to such dimer configurations and increased the cluster size up to $N_{\text{sites}} = 24$. We discovered that any structure factors were short-range and no evidence for bond order was found either. Moreover, this phase appeared to be more robust against $\Gamma \neq 0$ perturbations than the conventional Kitaev spin-liquid.

In Chapter 7 we introduced topologically nontrivial bands and notably highlighted the Shastry-Sutherland model, where nontrivial triplon bands occur. As a consequence, we introduced magnetic fields and considered the excitonic model in the 'deep' $J = 0$ paramagnetic regime, i.e. $\lambda \gg A$. We performed reasonable simplifications and neglected terms that enter the Hamiltonian in order $1/\lambda$. We demonstrated that for the fields $|\mathbf{h}| \in [0, 1.5\,A]$ the model hosts multiple topologically nontrivial

regimes, realized almost in the complete parameter space $\alpha \in [0, 180°]$. We classified these 'phases' in the form of a topological 'phase diagram' and explained the corresponding phase transitions.

Furthermore, we went beyond the common (J, K) couplings and included the cross-terms. We revealed that inclusion of the Γ contribution does not make the bands trivial, on the contrary it leads to new nontrivial band gap openings and thus to new topological 'phases' with Chern numbers up to $C = 8$. We gave the full 'phase diagram' for $\Gamma = 0.1\,A$, $\alpha \in [0, 180°]$ and $\alpha \in [180, 360°]$ correspondingly, clarified the phase transitions and verified that the sign of Γ swaps two halves. In addition, we provided a 'phase diagram' for another field direction $\mathbf{h} \parallel (0, 0, 1)$ and thermal conductivity plots for appropriate parameters.

The excitonic Kitaev-Heisenberg model demonstrates fascinating properties, especially concerning the topological bosonic bands. Indeed, we showed that even the 'boring' paramagnetic case provides a rich variety of topological 'phases' in almost all accessible regimes. Therefore, this model requires further investigations.

A more realistic picture can be provided by introducing the tetragonal/trigonal field splitting Δ and by including the Hund's coupling J_{H} into the perturbation theory calculations. These values then enter the (J, K, Γ) couplings in the same manner as t or t' and thus enlarge the physical sector. Projecting the resulting superexchange Hamiltonian onto the low-energy subspace one can derive the corresponding higher triplon terms h_3 and h_4 (see Eq. (3.48)) for $t' \neq 0$. Numerical treatment for the complete Hamiltonian $\mathcal{H} = h_2 + h_3 + h_4$ can enrich both classical and quantum phase diagrams, capture physics in more detail and perhaps determine the fate of the excitonic model 3.49.

Consequently, simulations on a larger $N_{\mathrm{sit}} = 24$ cluster (accepting a four-sublattice transformation) have to be performed for the whole parameter space in order to investigate magnetic phases more closely. The quadrupolar $\mathbf{u}$-contribution makes couplings of hoppings and pair-

ing terms different and should ideally be kept.

Concerning the topologically nontrivial bandstructure, a comprehensive study should be provided in the ordered phases, especially in the light of indication of the triplon liquid phase. A more complete model can be obtained by introducing additional couplings, such as Dzyaloshinskii-Moriya terms or next-nearest neighbour hoppings.

Moreover, it is argued that not all in-plane fields lead to topologically trivial bandgaps [172]. Thus, one can estimate, which field directions provide the topological character of the bands.

A

Perturbation theory notes

A.1 Superexchange Hamiltonian for d^2 systems.

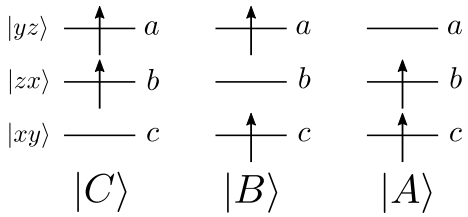

Figure A.1.: d^2 electron configurations

We derive a superexchange Hamiltonian $\mathcal{H}(d^2)$ for 90° bonding geometry and consider the d^4 theory substituting electrons with holes in $\mathcal{H}(d^2)$. We introduce the multi-electron states illustrated in Fig A.1

$$|A\rangle = A^\dagger|\text{vac}\rangle = b^\dagger c^\dagger|\text{vac}\rangle, \tag{A.1}$$

$$|B\rangle = B^\dagger|\text{vac}\rangle = a^\dagger c^\dagger|\text{vac}\rangle, \tag{A.2}$$

$$|C\rangle = C^\dagger|\text{vac}\rangle = a^\dagger b^\dagger|\text{vac}\rangle. \tag{A.3}$$

The following notation is used: n_a, n_b and n_c represent electron occupation numbers for the orbitals a, b and c (when not specified are labelled with γ), while n_A, n_B and n_C refer to the configurations A, B and C respectively (with a common subscript Γ; we impose an additional correspondence $\gamma = a \Leftrightarrow \Gamma = A$). Obvious relations, containing n_γ and n_Γ hold

$$n_A + n_B + n_C = 1, \tag{A.4}$$

$$n_a + n_b + n_c = 2, \tag{A.5}$$

i.e. only one configuration is realized exactly for two electrons. Analogous to $\tilde{l}$ (2.20) one introduces the effective momentum $\mathbf{L}$ [3, 114]

$$\mathbf{L}(d^2) = -i \begin{pmatrix} C^\dagger B - B^\dagger C \\ A^\dagger C - C^\dagger A \\ B^\dagger A - A^\dagger B \end{pmatrix}. \tag{A.6}$$

By means of standard fermionic commutation relations we define

$$L_y^2 = -\big(\cancelto{0}{b^\dagger c^\dagger b a b^\dagger c^\dagger b a} - b^\dagger c^\dagger b a a^\dagger b^\dagger c b - a^\dagger b^\dagger c b b^\dagger c^\dagger b a \tag{A.7}$$

$$+ \cancelto{0}{a^\dagger b^\dagger c b a^\dagger b^\dagger c b}\big) = a^\dagger b^\dagger (1 - b^\dagger b)(1 - c^\dagger c) b a + b^\dagger c^\dagger (1 - a^\dagger a)(1 - b^\dagger b) c b$$

$$= a^\dagger b^\dagger b a + b^\dagger c^\dagger c b = n_C + n_A = 1 - n_B,$$

which in total yields

$$\mathbf{L}^2(d^2) = \begin{pmatrix} 1 - n_A \\ 1 - n_B \\ 1 - n_C \end{pmatrix}. \tag{A.8}$$

On the other hand, $n_\gamma = 1$ if and only if $n_\Gamma = 0$, i.e. the configuration Γ is not realized. Thus, we obtain

$$\begin{cases} n_a = 1 - n_A, \\ n_b = 1 - n_B, \\ n_c = 1 - n_C. \end{cases} \tag{A.9}$$

Moreover, annihilating a b-electron and creating an a-electron in the state $|A\rangle$ is equivalent to annihilating the configuration A and creating the configuration B (see Fig A.1):

$$a^\dagger b|A\rangle = a^\dagger b b^\dagger c^\dagger|\text{vac}\rangle = a^\dagger(1-b^\dagger b)c^\dagger|\text{vac}\rangle = a^\dagger c^\dagger|\text{vac}\rangle = |B\rangle. \quad \text{(A.10)}$$

Formally, in terms of capital letters (A.10) such transformations for $|B\rangle$ and $|C\rangle$ read as

$$\begin{cases} B^\dagger A|A\rangle = B^\dagger|\text{vac}\rangle = |B\rangle, \\ C^\dagger B|B\rangle = C^\dagger|\text{vac}\rangle = |C\rangle, \\ A^\dagger C|C\rangle = A^\dagger|\text{vac}\rangle = |A\rangle. \end{cases} \quad \Rightarrow \quad \begin{cases} a^\dagger b = B^\dagger A, \\ b^\dagger c = C^\dagger B, \\ c^\dagger a = A^\dagger C. \end{cases} \quad \text{(A.11)}$$

Using the second order perturbation theory in t/U we finally obtain the effective d^2 Hamiltonian in the case of 90° bonding geometry

$$\mathcal{H}^{(2)}_{d^2} = -\frac{t^2}{U}\sum_{\langle ij\rangle}\Big\{(a^\dagger_{i,\uparrow}b_{j,\uparrow} + a^\dagger_{i,\downarrow}b_{j,\downarrow})(a^\dagger_{j,\uparrow}b_{i,\uparrow} + a^\dagger_{j,\downarrow}b_{i,\downarrow}) + \text{h.c.}\Big\} \quad \text{(A.12)}$$

$$= \frac{t^2}{U}\sum_{\langle ij\rangle}\Big\{\big(\mathbf{S}_i\mathbf{S}_j + 1\big)\big((n_a n_b + n_b n_a)_{ij} + (a^\dagger b)_i(b^\dagger a)_j + (b^\dagger a)_i(a^\dagger b)_j\big)\Big\}$$

$$= \frac{t^2}{U}\sum_{\langle ij\rangle}\Big\{\big(\mathbf{S}_i\mathbf{S}_j + 1\big)\big[(L^x_i L^y_j)^2 + (L^y_i L^x_j)^2 + L^y_i L^x_i L^y_j L^x_j + L^x_i L^y_i L^x_j L^y_j\big]$$

$$+ (L^z_i)^2 + (L^z_j)^2 - 4\Big\}.$$

The corresponding model with four electrons on the d-shell is given by the d^2-model, where electrons are substituted by holes and consequently $\mathbf{L}(d^4) = -\mathbf{L}(d^2)$.

We include the direct exchange interaction t' as well and resulting terms $\sim tt'/U$ and t'^2/U are treated analogously to (A.8 − A.11).

B

Projection technical details.

B.1 Projection of the Hamiltonian

We consider the superexchange Hamiltonian (3.52), which for the c-bond reads as

$$\mathcal{H}^c_{\text{eff}} = \frac{1}{U}\sum_{\langle ij\rangle}(\mathbf{S}_i\mathbf{S}_j + 1)\Omega^c_{ij} + \frac{t^2 - t'^2}{U}\left((L^z_i)^2 + (L^z_j)^2\right) + \mathcal{H}_{\text{SOC}} \quad \text{(B.1)}$$

where

$$\mathcal{H}_{\text{SOC}} = \lambda\sum_i \mathbf{S}_i\mathbf{L}_i,$$

and the bond-dependent operator is

$$\begin{aligned}\Omega^c_{ij} =& t^2\Big\{(L_x)^2_i(L_y)^2_j + (L_y)^2_i(L_x)^2_j + (L_xL_y)_i(L_xL_y)_j + (L_yL_x)_i(L_yL_x)_j\Big\}\\ &-tt'\Big\{(L_zL_y)_i(L_xL_z)_j + (L_zL_x)_i(L_yL_z)_j + (L_xL_z)_i(L_zL_y)_j\\ &+ (L_yL_z)_i(L_zL_x)_j\Big\} + t'^2\Big\{(L_z)^2_i(L_z)^2_j\Big\}.\end{aligned}$$

The table (B.3) provides projections of elementary elements entering the Hamiltonian (B.1). One can note that the most part of them are proportional to $(T_\gamma - T^\dagger_\gamma)$ and hence it is convenient to introduce $\mathbf{v}_i = -i(\mathbf{T}_i - \mathbf{T}^\dagger_i)/2$. Thus, the t^2 terms contribution is

- $(L_xL_y)_i(L_xL_y)_j + (L_yL_x)_i(L_yL_x)_j = -\frac{4}{3}v_z^i v_z^j$
- $(S_xL_x^2)_i(S_xL_y^2)_j + (S_xL_y^2)_i(S_xL_x^2)_j = \frac{8}{3}v_x^i v_x^j,$

  $(S_yL_x^2)_i(S_yL_y^2)_j + (S_yL_y^2)_i(S_yL_x^2)_j = \frac{8}{3}v_y^i v_y^j.$
- $(S_xL_xL_y)_i(S_xL_xL_y)_j + (S_yL_xL_y)_i(S_yL_xL_y)_j = -\frac{1}{3}(u_y^i u_y^j - v_y^i v_y^j),$

  $(S_xL_yL_x)_i(S_xL_yL_x)_j + (S_yL_yL_x)_i(S_yL_yL_x)_j = -\frac{1}{3}(u_x^i u_x^j - v_x^i v_x^j).$

In total one obtains

$$\begin{aligned} t^2\text{-Contribution} &= \Big(\frac{8}{3} + \frac{1}{3}\Big)(v_xv_x + v_yv_y)_{ij} - \frac{1}{3}(u_xu_x + u_yu_y)_{ij} \\ &= 3(v_xv_x + v_yv_y)_{ij} - \frac{1}{3}(u_xu_x + u_yu_y)_{ij}. \end{aligned}$$

The direct exchange yields

$$\begin{aligned} t'^2\text{-Contribution} &= (S_xL_z^2)_i(S_xL_z^2)_j + (S_yL_z^2)_i(S_yL_z^2)_j + (S_zL_z^2)_i(S_zL_z^2)_j \\ &= \frac{2}{3}(v_xv_x + v_yv_y)_{ij} + \frac{8}{3}v_z^i v_z^j. \end{aligned}$$

The cross-terms projections are

- $(L_zL_x)_i + (L_yL_z)_j + (L_zL_y)_i(L_xL_z)_j + (L_xL_z)_i(L_zL_y)_j$
  $+(L_yL_z)_i(L_zL_x)_j = 0 \cdot (u_xu_y + u_yu_x)_{ij} + \frac{4}{3}(v_xv_y + v_yv_x)_{ij}.$
- $(S_xL_xL_z)_i(S_xL_zL_y)_j + (S_yL_yL_z)_i(S_yL_zL_x)_j = 0,$
  $(S_xL_yL_z)_i(S_xL_zL_x)_j + (S_yL_xL_z)_i(S_yL_zL_y)_j = 0,$
  $(S_xL_zL_x)_i(S_xL_yL_z)_j + (S_yL_zL_y)_i(S_yL_xL_z)_j = 0,$
  $(S_xL_zL_y)_i(S_xL_xL_z)_j + (S_yL_zL_x)_i(S_yL_yL_z)_j = 0.$

- And finally

$$\left.\begin{aligned}(S_zL_xL_z)_i(S_zL_zL_y)_j &= -\tfrac{1}{6}(u_x+iv_x)_i(u_y-iv_y)_j,\\ (S_zL_yL_z)_i(S_zL_zL_x)_j &= -\tfrac{1}{6}(u_y+iv_y)_i(u_x-iv_x)_j,\\ (S_zL_zL_x)_i(S_zL_yL_z)_j &= -\tfrac{1}{6}(u_x-iv_x)_i(u_y+iv_y)_j,\\ (S_zL_zL_y)_i(S_zL_xL_z)_j &= -\tfrac{1}{6}(u_y-iv_y)_i(u_x+iv_x)_j.\end{aligned}\right\} =$$
$$= -\frac{1}{3}\big[(u_xu_y+u_yu_x)_{ij}+(v_xv_y+v_yv_x)_{ij}\big].$$

In total we have

$$tt'\text{-Contribution} = -\frac{1}{3}(u_xu_y+u_yu_x)_{ij}+\Big(\frac{4}{3}-\frac{1}{3}\Big)(v_xv_y+v_yv_x)_{ij}$$
$$= (v_xv_y+v_yv_x)_{ij}-\frac{1}{3}(u_xu_y+u_yu_x)_{ij}.$$

The resulting effective Hamiltonian for the c-bond is given by

$$\mathcal{H}^c = \frac{1}{U}\sum_{\langle ij\rangle}\Big[t^2\big\{3(v_xv_x+v_yv_y)_{ij}-\frac{1}{3}(u_xu_x+u_yu_y)_{ij}\big\}$$
$$+tt'\big\{(v_xv_y+v_yv_x)_{ij}-\frac{1}{3}(u_xu_y+u_yu_x)_{ij}\big\}$$
$$+t'^2\big\{\frac{2}{3}(v_xv_x+v_yv_y)_{ij}+\frac{8}{3}(v_zv_z)_{ij}\big\}\Big]$$

B.2 Projection of the Hamiltonian with tetragonal crystal field included

We introduce the tetragonal crystal filed splitting by means of two angles [34]

$$\tan\theta_1 = \frac{1}{\delta+\sqrt{1+\delta^2}}, \qquad \tan\theta_0 = \sqrt{1+\kappa^2}-\kappa \tag{B.2}$$

where

$$\delta = \frac{\Delta}{2\lambda}, \qquad \kappa = \frac{1}{\sqrt{2}}\Big(\delta - \frac{1}{2}\Big). \tag{B.3}$$

For the sake of convenience we use $c_i \equiv \cos\theta_i$ and $s_i \equiv \sin\theta_i$ with $i = 0, 1$. One reaches the cubic limit by setting $\Delta = 0$, which in this notation is equivalent to $c_0 = 1/\sqrt{3}$, $s_0 = \sqrt{2/3}$ and $c_1 = s_1 = 1/\sqrt{2}$.

The low energy subspace then reads as [34, 173]

$$\begin{aligned}
|s\rangle &= \frac{1}{\sqrt{2}}\big(s_0|1,-1\rangle - c_0\sqrt{2}|0,0\rangle + s_0|-1,1\rangle\big), \\
|t_x\rangle &= \frac{-i}{\sqrt{2}}\big(c_1|1,0\rangle - s_1|0,1\rangle + c_1|-1,0\rangle - s_1|0,-1\rangle\big), \\
|t_y\rangle &= \frac{1}{\sqrt{2}}\big(c_1|1,0\rangle - s_1|0,1\rangle - c_1|-1,0\rangle + s_1|0,-1\rangle\big), \\
|t_z\rangle &= \frac{i}{\sqrt{2}}\big(|1,-1\rangle - |-1,1\rangle\big).
\end{aligned} \tag{B.4}$$

According to the rules listed in the table (B.3) and introducing $\mathbf{v}_i = -i(\mathbf{T}_i - \mathbf{T}_i^\dagger)/2$ we obtain for the t^2 terms

- $(L_xL_y)_i(L_xL_y)_j + (L_yL_x)_i(L_yL_x)_j = -2s_0^2 v_z^i v_z^j$.
- $(S_xL_x^2)_i(S_xL_y^2)_j + (S_xL_y^2)_i(S_xL_x^2)_j = 8\Big(c_0c_1 + \frac{s_0s_1}{\sqrt{2}}\Big)c_0c_1 v_x^i v_x^j$,
  $(S_yL_x^2)_i(S_yL_y^2)_j + (S_yL_y^2)_i(S_yL_x^2)_j = 8\Big(c_0c_1 + \frac{s_0s_1}{\sqrt{2}}\Big)c_0c_1 v_y^i v_y^j$.
- $(S_xL_xL_y)_i(S_xL_xL_y)_j + (S_yL_xL_y)_i(S_yL_xL_y)_j = -(s_1s_0)^2(u_y^i u_y^j - v_y^i v_y^j)$,
  $(S_xL_yL_x)_i(S_xL_yL_x)_j + (S_yL_yL_x)_i(S_yL_yL_x)_j = -(s_1s_0)^2(u_x^i u_x^j - v_x^i v_x^j)$.

This in total yields the t^2-contribution

$$\begin{aligned}
\mathcal{H}(t^2) &= \Big(8(c_0c_1 + \tfrac{s_0s_1}{\sqrt{2}})c_0c_1 + (s_0s_1)^2\Big)(v_xv_x + v_yv_y)_{ij} - (s_0s_1)^2(u_xu_x + u_yu_y)_{ij} \\
&= (2\sqrt{2}c_0c_1 + s_0s_1)^2(v_xv_x + v_yv_y)_{ij} - (s_0s_1)^2(u_xu_x + u_yu_y)_{ij}.
\end{aligned}$$

The direct exchange t'^2 terms take the form

$$\begin{aligned}\mathcal{H}(t'^2) &= (S_xL_z^2)_i(S_xL_z^2)_j + (S_yL_z^2)_i(S_yL_z^2)_j + (S_zL_z^2)_i(S_zL_z^2)_j \\ &= 2(s_0s_1)^2(v_xv_x + v_yv_y)_{ij} + 4s_0^2v_z^iv_z^j.\end{aligned}$$

And for the cross-terms tt' we obtain

- $(L_zL_x)_i + (L_yL_z)_j + (L_zL_y)_i(L_xL_z)_j + (L_xL_z)_i(L_zL_y)_j + (L_yL_z)_i(L_zL_x)_j = 2\Big(c_0s_1 - \frac{c_1s_0}{\sqrt{2}}\Big)^2(u_xu_y + u_yu_x)_{ij} + 2\Big(c_0s_1 + \frac{c_1s_0}{\sqrt{2}}\Big)^2(v_xv_y + v_yv_x)_{ij}$.

- $(S_xL_xL_z)_i(S_xL_zL_y)_j + (S_yL_yL_z)_i(S_yL_zL_x)_j = 0,$
  $(S_xL_yL_z)_i(S_xL_zL_x)_j + (S_yL_xL_z)_i(S_yL_zL_y)_j = 0,$
  $(S_xL_zL_x)_i(S_xL_yL_z)_j + (S_yL_zL_y)_i(S_yL_xL_z)_j = 0,$
  $(S_xL_zL_y)_i(S_xL_xL_z)_j + (S_yL_zL_x)_i(S_yL_yL_z)_j = 0.$

- Finally

$$\left.\begin{aligned}(S_zL_xL_z)_i(S_zL_zL_y)_j &= \tfrac{-c_1^2s_0^2}{2}(u_x + iv_x)_i(u_y - iv_y)_j,\\ (S_zL_yL_z)_i(S_zL_zL_x)_j &= \tfrac{-c_1^2s_0^2}{2}(u_y + iv_y)_i(u_x - iv_x)_j,\\ (S_zL_zL_x)_i(S_zL_yL_z)_j &= \tfrac{-c_1^2s_0^2}{2}(u_x - iv_x)_i(u_y + iv_y)_j,\\ (S_zL_zL_y)_i(S_zL_xL_z)_j &= \tfrac{-c_1^2s_0^2}{2}(u_y - iv_y)_i(u_x + iv_x)_j.\end{aligned}\right\} =$$
$$= -c_1^2s_0^2\big[(u_xu_y + u_yu_x)_{ij} + (v_xv_y + v_yv_x)_{ij}\big].$$

Summarizing, one gets the tt'-contribution

$$\begin{aligned}\mathcal{H}(tt') = 2\Big((c_0s_1 - \tfrac{c_1s_0}{\sqrt{2}})^2 - c_1^2s_0^2\Big)(u_xu_y + u_yu_x)_{ij} + 2\Big((c_0s_1 + \tfrac{c_1s_0}{\sqrt{2}})^2 \\ - c_1^2s_0^2\Big)(v_xv_y + v_yv_x)_{ij} = 2c_0s_1(c_0s_1 + \sqrt{2}s_0c_1)(v_xv_y + v_yv_x)_{ij} \\ + 2c_0s_1(c_0s_1 - \sqrt{2}s_0c_1)(u_xu_y + u_yu_x)_{ij}.\end{aligned}$$

The resulting effective Hamiltonian reads as

$$\mathcal{H}_{\text{eff}} = \mathcal{H}_{\text{SO}} + \mathcal{H}_{\text{CF}} + \mathcal{H}^{(a)} + \mathcal{H}^{(b)} + \mathcal{H}^{(c)},$$

$$\mathcal{H}_{\text{SO}} = \lambda \sum_i \Big\{ (2\sqrt{2}c_0 s_0 + s_0^2 - 2c_1 s_1) n_i + (2c_1 s_1 - 1) n_i^z \Big\},$$

$$\mathcal{H}_{\text{CF}} = \Delta \sum_i \Big\{ (s_1^2 - s_0^2) n_i + c_1^2 n_i^z + s_0^2 - \frac{2}{3} \Big\},$$

$$\begin{aligned}\mathcal{H}^{(c)} = \frac{1}{U} \sum_{\langle ij \rangle} \Big[& t^2 \big\{ (2\sqrt{2}c_0 c_1 + s_0 s_1)^2 (v_x v_x + v_y v_y)_{ij} - (s_0 s_1)^2 (u_x u_x + u_y u_y)_{ij} \big\} \\ & - 2c_0 s_1 t t' \big\{ (c_0 s_1 + \sqrt{2} s_0 c_1)(v_x v_y + v_y v_x)_{ij} + (c_0 s_1 - \sqrt{2} s_0 c_1)(u_x u_y + u_y u_x)_{ij} \big\} \\ & + t'^2 \big\{ 2(s_0 s_1)^2 (v_x v_x + v_y v_y)_{ij} + 4 s_0^2 v_z^i v_z^j \big\} \Big]\end{aligned}$$

B.3 Tables of projections

Operator	Projection	Operator	Projection
S_x	$i\sqrt{\frac{2}{3}}(T_x - T_x^\dagger)$	$S_xL_y^2$	$\frac{i}{\sqrt{6}}(T_x^\dagger - T_x)$
S_y	$i\sqrt{\frac{2}{3}}(T_y - T_y^\dagger)$	$S_yL_y^2$	$i\sqrt{\frac{2}{3}}(T_y^\dagger - T_y)$
S_z	$i\sqrt{\frac{2}{3}}(T_z - T_z^\dagger)$	$S_zL_y^2$	$\frac{i}{\sqrt{6}}(T_z^\dagger - T_z)$
L_x	$-i\sqrt{\frac{2}{3}}(T_x - T_x^\dagger)$	$S_xL_z^2$	$\frac{i}{\sqrt{6}}(T_x^\dagger - T_x)$
L_y	$-i\sqrt{\frac{2}{3}}(T_y - T_y^\dagger)$	$S_yL_z^2$	$\frac{i}{\sqrt{6}}(T_y^\dagger - T_y)$
L_z	$-i\sqrt{\frac{2}{3}}(T_z - T_z^\dagger)$	$S_zL_z^2$	$i\sqrt{\frac{2}{3}}(T_z^\dagger - T_z)$
L_x^2	$\frac{2}{3}s^\dagger s + t_x^\dagger t_x + \frac{1}{2}(t_y^\dagger t_y + t_z^\dagger t_z)$	$S_xL_xL_y$	$-\frac{i}{\sqrt{6}}T_y^\dagger$
L_y^2	$\frac{2}{3}s^\dagger s + t_y^\dagger t_y + \frac{1}{2}(t_x^\dagger t_x + t_z^\dagger t_z)$	$S_yL_xL_y$	$\frac{i}{\sqrt{6}}T_x$
L_z^2	$\frac{2}{3}s^\dagger s + \frac{1}{2}(t_x^\dagger t_x + t_y^\dagger t_y) + t_z^\dagger t_z$	$S_zL_xL_y$	$-\frac{i}{3}s^\dagger s$
L_xL_y	$\frac{1}{\sqrt{6}}(T_z^\dagger - T_z)$	$S_xL_xL_z$	$\frac{i}{\sqrt{2}}T_z^\dagger$
L_xL_z	$\frac{1}{\sqrt{6}}(T_y^\dagger - T_y)$	$S_yL_xL_z$	$\frac{i}{3}s^\dagger s$
L_yL_z	$\frac{1}{\sqrt{6}}(T_x^\dagger - T_x)$	$S_zL_xL_z$	$-\frac{i}{\sqrt{6}}T_x$
$S_xL_x^2$	$i\sqrt{\frac{2}{3}}(T_x^\dagger - T_x)$	$S_xL_yL_z$	$-\frac{i}{3}s^\dagger s$
$S_yL_x^2$	$\frac{i}{\sqrt{6}}(T_y^\dagger - T_y)$	$S_yL_yL_z$	$\frac{i}{\sqrt{6}}T_z^\dagger$
$S_zL_x^2$	$\frac{i}{\sqrt{6}}(T_z^\dagger - T_z)$	$S_zL_yL_z$	$\frac{i}{\sqrt{6}}T_y$

Table B.1.: Projections of elementary entries of the superexchange Hamiltonian up to the terms linear in triplons.

Operator	Projection	Operator	Projection
S_x	$\frac{i}{\sqrt{2}}(c_0c_1\sqrt{2}+s_1s_0)(T_x-T_x^\dagger)$	$S_xL_y^2$	$ic_0c_1(T_x^\dagger-T_x)$
S_y	$\frac{i}{\sqrt{2}}(c_0c_1\sqrt{2}+s_1s_0)(T_y-T_y^\dagger)$	$S_yL_y^2$	$\frac{i}{\sqrt{2}}(c_0c_1\sqrt{2}+s_1s_0)(T_y^\dagger-T_y)$
S_z	$is_0(T_z-T_z^\dagger)$	$S_zL_y^2$	$\frac{is_0}{2}(T_z^\dagger-T_z)$
L_x	$\frac{-i}{\sqrt{2}}(s_1c_0\sqrt{2}+s_0c_1)(T_x-T_x^\dagger)$	$S_xL_z^2$	$\frac{i}{\sqrt{2}}s_1s_0(T_x^\dagger-T_x)$
L_y	$\frac{-i}{\sqrt{2}}(s_1c_0\sqrt{2}+s_0c_1)(T_y-T_y^\dagger)$	$S_yL_z^2$	$\frac{i}{\sqrt{2}}s_1s_0(T_y^\dagger-T_y)$
L_z	$-is_0(T_z-T_z^\dagger)$	$S_zL_z^2$	$is_0^2(T_z^\dagger-T_z)$
L_x^2	$\frac{1}{2}\left(c_0^2+1\right)s^\dagger s+t_x^\dagger t_x+c_1^2t_y^\dagger t_y+\frac{1}{2}t_z^\dagger t_z$	$S_xL_xL_y$	$\frac{-i}{\sqrt{2}}s_1s_0T_y^\dagger$
L_y^2	$\frac{1}{2}\left(c_0^2+1\right)s^\dagger s+c_1^2t_x^\dagger t_x+t_y^\dagger t_y+\frac{1}{2}t_z^\dagger t_z$	$S_yL_xL_y$	$\frac{i}{\sqrt{2}}s_1s_0T_x$
L_z^2	$s_0^2s^\dagger s+s_1^2(t_x^\dagger t_x+t_y^\dagger t_y)+t_z^\dagger t_z$	$S_zL_xL_y$	$\frac{-is_0^2}{2}s^\dagger s$
L_xL_y	$\frac{s_0}{2}(T_z^\dagger-T_z)$	$S_xL_xL_z$	$\frac{i}{\sqrt{2}}c_0T_z^\dagger$
L_xL_z	$c_0s_1T_y^\dagger-\frac{c_1s_0}{\sqrt{2}}T_y$	$S_yL_xL_z$	$\frac{i}{\sqrt{2}}c_0s_0s^\dagger s$
L_yL_z	$c_0s_1T_x^\dagger-\frac{c_1s_0}{\sqrt{2}}T_x$	$S_zL_xL_z$	$\frac{-i}{\sqrt{2}}c_1s_0T_x$
$S_xL_x^2$	$\frac{i}{\sqrt{2}}(c_0c_1\sqrt{2}+s_1s_0)(T_x^\dagger-T_x)$	$S_xL_yL_z$	$\frac{-i}{\sqrt{2}}s_0c_0s^\dagger s$
$S_yL_x^2$	$ic_0c_1(T_y^\dagger-T_y)$	$S_yL_yL_z$	$\frac{i}{\sqrt{2}}c_0T_z^\dagger$
$S_zL_x^2$	$\frac{is_0}{2}(T_z^\dagger-T_z)$	$S_zL_yL_z$	$\frac{i}{\sqrt{2}}s_0c_1T_y$

Table B.2.: Projections of elementary entries of the superexchange Hamiltonian up to the terms linear in triplons with tetragonal crystal field included.

C

Uniform distribution in a ball

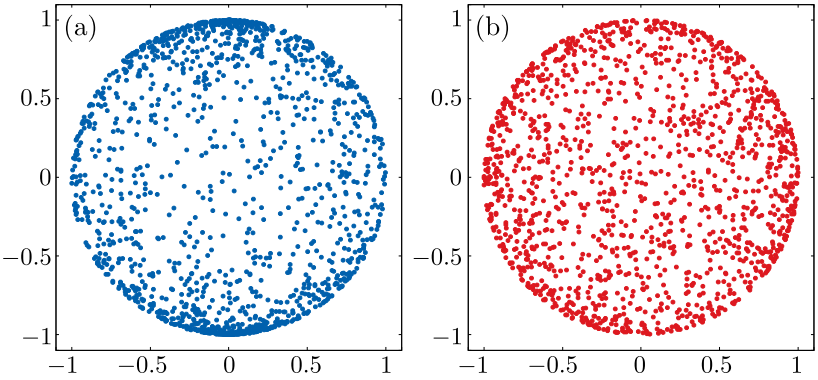

Figure C.1.: Examples of a distribution of 1000 points on a sphere projected onto the XZ plane. (a) Incorrect. Displays the result of $r = \text{rand}[0, 1]$, $\phi = \text{rand}[0, 2\pi]$, $\theta = \text{rand}[-\pi, \pi]$. (b) Correct.

We consider a unit sphere. An infinitesimal solid angle $d\Omega = \sin\theta \, d\theta d\varphi$ explicitly depends on θ, thus if we take the angles from uniform distributions $\theta = \pi u$, $\phi = 2\pi v$, with $u, v = \text{rand}[0, 1]$, and pick a random

point, we obtain an incorrect result. Indeed, after n iterations the resulting points gather around the poles (see Fig. C.1(a)). Our goal is to find such functions $f(\theta)$ and $g(\varphi)$ that

$$\begin{cases} d\Omega = \text{const} \cdot df(\theta) dg(\varphi), \\ \forall\theta \in [0,\pi] \quad \exists f^{-1}(\theta), \qquad \forall\varphi \in [0,2\pi] \quad \exists g^{-1}(\varphi) \end{cases} \tag{C.1}$$

At first glance an obvious solution $d\Omega = \sin\theta\, d\theta d\varphi = -d\cos\theta\, d\varphi$ fulfils (C.1) but $\cos\theta$ does not have an inverse function for $\theta \in [0,\pi]$. However, with help of well known relations

$$\sin 2x = 2\sin x\cos x, \qquad d\cos^2 x = -2\cos x \sin x\, dx, \tag{C.2}$$

we propose the following function

$$d\cos^2\frac{\theta}{2} = -\cos\frac{\theta}{2}\sin\frac{\theta}{2}d\theta = -\frac{1}{2}\sin\theta d\theta \quad \Rightarrow \quad d\Omega = -2\, d\cos^2\frac{\theta}{2} d\varphi.$$

Therefore, instead of θ we uniformly distribute $\cos^2\frac{\theta}{2}$. Using

$$\cos^2\frac{\theta}{2} = \frac{\cos\theta + 1}{2}, \tag{C.3}$$

we finally conclude that a uniform sphere covering is provided by

$$\begin{cases} \theta = \arccos\Big(2u-1\Big), \\ \phi = 2\pi v, \end{cases} \qquad u, v = \text{rand}[0,1]. \tag{C.4}$$

The same holds for a ball but substituting

$$d\Omega \;\to\; dV = r^2 \sin\theta\, dr d\theta d\varphi = \frac{1}{3} dr^3 d\cos^2\frac{\theta}{2} d\varphi, \tag{C.5}$$

and thus

$$\begin{cases} r = \sqrt[3]{3w}, \\ \theta = \arccos\Big(2u-1\Big), \\ \phi = 2\pi v. \end{cases} \qquad u, v, w = \text{rand}[0,1]. \tag{C.6}$$

D

Comments on the Linear Spin-Wave Theory

D.1 Bogolyubov Transformation of the excitonic model

We consider the excitonic Hamiltonian on the honeycomb lattice (its z-part)

$$\begin{aligned} H^z_{\text{eff}} =& \lambda \sum_i z_i^\dagger z_i + \lambda \sum_i \tilde{z}_i^\dagger \tilde{z}_i + \frac{A}{4} \cos\alpha \sum_{\langle ij \rangle} \left(z_i^\dagger \tilde{z}_j + \tilde{z}_j^\dagger z_i - z_i \tilde{z}_j - z_i^\dagger \tilde{z}_j^\dagger \right) \\ &+ \frac{A}{4} \sin\alpha \sum_{\langle ij \rangle_c} \left(z_i^\dagger \tilde{z}_j + \tilde{z}_j^\dagger z_i - z_i \tilde{z}_j - z_i^\dagger \tilde{z}_j^\dagger \right), \end{aligned} \tag{D.1}$$

We keep the prefactor $1/4$ in front of the couplings, since it allows us to make a straightforward comparison to the classical analysis results from Chapter 4. We go to momentum space using standard 2D Fourier transformation (in what follows we label $\mathbf{k}$ vectors simply with k)

$$z_i = \frac{1}{\sqrt{N}} \sum_k z_k e^{-ikr}, \qquad \text{etc.} \tag{D.2}$$

and get

$$\mathcal{H}_{\rm eff}(k) = \sum_k \Big[\lambda(z_k^\dagger z_k + \tilde{z}_k^\dagger \tilde{z}_k) + \gamma_k \tilde{z}_k^\dagger z_k + \gamma_k^* z_k^\dagger \tilde{z}_k - \gamma_k^* z_k \tilde{z}_{-k} - \gamma_k z_k^\dagger \tilde{z}_{-k}^\dagger\Big],$$

where

$$\gamma_k = \frac{3A}{4}\phi_k, \tag{D.3}$$
$$\phi_k = \frac{1}{3}(e^{-ik_a} + e^{-ik_b} + e^{-ik_c})\cos\alpha + \frac{1}{3}e^{-ik_c}\sin\alpha,$$
$$k_a = -\frac{1}{2}k_x - \frac{\sqrt{3}}{2}k_y, \qquad k_b = -\frac{1}{2}k_x + \frac{\sqrt{3}}{2}k_y \qquad \text{and} \qquad k_c = k_x.$$

Now we introduce a generalized Bogoliubov transformation [145]

$$\begin{cases} \alpha_k = u_1 z_k + u_2 \tilde{z}_k + v_1 z_{-k}^\dagger + v_2 \tilde{z}_{-k}^\dagger, & u_1 \equiv u_{1,k}, \quad etc. \\ \beta_k = \bar{u}_1 z_k + \bar{u}_2 \tilde{z}_k + \bar{v}_1 z_{-k}^\dagger + \bar{v}_2 \tilde{z}_{-k}^\dagger, \\ \alpha_{-k}^\dagger = u_1 z_{-k}^\dagger + u_2 \tilde{z}_{-k}^\dagger + v_1 z_k + v_2 \tilde{z}_k, \\ \beta_{-k}^\dagger = \bar{u}_1 z_{-k}^\dagger + \bar{u}_2 \tilde{z}_{-k}^\dagger + \bar{v}_1 z_k + \bar{v}_2 \tilde{z}_k, \end{cases} \tag{D.4}$$

Since the Bogoliubov transformation is canonical, i.e. new operators obey the same commutation relations, following constraints should hold

$$\begin{aligned} &[\alpha_k, \alpha_{k'}^\dagger] = \delta_{k,k'}, \quad \Rightarrow \quad u_1^2 + u_2^2 - v_1^2 - v_2^2 = 1, \\ &[\beta_k, \beta_{k'}^\dagger] = \delta_{k,k'}, \quad \Rightarrow \quad \bar{u}_1^2 + \bar{u}_2^2 - \bar{v}_1^2 - \bar{v}_2^2 = 1, \\ &[\alpha_k, \beta_{k'}^\dagger] = 0, \quad \Rightarrow \quad u_1\bar{u}_1 + u_2\bar{u}_2 - v_1\bar{v}_1 - v_2\bar{v}_2 = 0. \end{aligned}$$

The transformed Hamiltonian takes the diagonal form [145]

$$\mathcal{H}_{\rm eff}^{diag} = \sum_k \Big[\omega_{1,k}\alpha_k^\dagger\alpha_k + \omega_{2,k}\beta_k^\dagger\beta_k\Big] + \text{const},$$

and resulting equations of motion are

$$\begin{cases} i\dot{\alpha}_k = [\alpha_k, \mathcal{H}_{\rm eff}^{diag}(k')] = \omega_{1,k}\alpha_{k'}\delta_{k,k'}, \\ i\dot{\alpha}_k = [\alpha_k, \mathcal{H}_{\rm eff}(k')], \end{cases} \qquad \Rightarrow \quad [\alpha_k, \mathcal{H}_{\rm eff}(k')] = \omega_{1,k}\alpha_{k'}\delta_{k,k'}.$$

Calculating $[\alpha_k, \mathcal{H}_{\text{eff}}(k')]$ and collecting corresponding coefficients one obtains a system of linear equations

$$\begin{cases} (\lambda-\omega)u_1 + \gamma_k^* u_2 + 0\cdot v_1 + \gamma_k v_2 = 0, \\ \gamma_k u_1 + (\lambda-\omega)u_2 + \gamma_k v_1 + 0\cdot v_2 = 0, \\ 0\cdot u_1 + \gamma_k^* u_2 + (\lambda+\omega)v_1 + \gamma_k v_2 = 0, \\ \gamma_k^* u_1 + 0\cdot u_2 + \gamma_k^* v_1 + (\lambda+\omega)v_2 = 0. \end{cases}$$

This system is solvable if and only if

$$\det \begin{pmatrix} \lambda-\omega & \gamma_k^* & 0 & \gamma_k \\ \gamma_k & \lambda-\omega & \gamma_k & 0 \\ 0 & \gamma_k^* & \lambda+\omega & \gamma_k \\ \gamma_k^* & 0 & \gamma_k^* & \lambda+\omega \end{pmatrix} = 0, \tag{D.5}$$

which gives

$$\omega_k = \sqrt{\lambda^2 \pm 2\lambda|\gamma_k|}, \tag{D.6}$$

and thus the dispersion relation of the z-triplon reads as

$$\omega_k(A,\alpha) = \lambda\sqrt{1 - \frac{3A|\phi_k(\alpha)|}{2\lambda}}. \tag{D.7}$$

Alternatively, one obtains (D.7) by solving the eigenproblem of the matrix

$$P(k) = \begin{pmatrix} \lambda & \gamma_k^* & 0 & \gamma_k \\ \gamma_k & \lambda & \gamma_k & 0 \\ 0 & -\gamma_k^* & -\lambda & -\gamma_k \\ -\gamma_k^* & 0 & -\gamma_k^* & -\lambda \end{pmatrix}. \tag{D.8}$$

This approach is especially useful if roots of the characteristic polynomial cannot be found analytically (e.g. if we include Γ-terms) and a numerical treatment is required.

D.2 Excitations in a condensed phase

As soon as a magnetic phase transition occurs and, for example, the t_z boson condenses, it mixes up coherently with the singlet s. Therefore, we introduce new operators φ and $\tilde{t}$ (in following we omit the z-index) and consider the ferromagnetic case, which does not require any sublattice transformation to be done, e.g. in the antiferromagnetic regime it is $T_A \to iT$, $T_B \to -iT$ [21]. Using techniques similar to a linear combination of atomic orbitals (LCAO) [99], we perform a basis transformation

$$\begin{cases} s = \alpha\varphi + i\beta\tilde{t}, \\ t = i\beta\varphi + \alpha\tilde{t}. \end{cases} \qquad \begin{cases} s^\dagger = \alpha\varphi^\dagger - i\beta\tilde{t}^\dagger, \\ t^\dagger = -i\beta\varphi^\dagger + \alpha\tilde{t}^\dagger, \end{cases} \tag{D.9}$$

so that new φ boson condenses, while $\tilde{t}$ remains fluctuating[1]. The hard-core constraint $s^\dagger s + t^\dagger t = 1$ takes the form

$$\begin{aligned} s^\dagger s &= \alpha^2\varphi^\dagger\varphi - i\alpha\beta(\tilde{t}^\dagger\varphi - \varphi^\dagger\tilde{t}) + \beta^2\tilde{t}^\dagger\tilde{t}, \\ t^\dagger t &= \beta^2\varphi^\dagger\varphi + i\alpha\beta(\tilde{t}^\dagger\varphi - \varphi^\dagger\tilde{t}) + \alpha^2\tilde{t}^\dagger\tilde{t}, \\ s^\dagger s + t^\dagger t &= 1 = (\alpha^2+\beta^2)\varphi^\dagger\varphi + (\alpha^2+\beta^2)\tilde{t}^\dagger\tilde{t}. \end{aligned} \tag{D.10}$$

Hence, a logical parametrization of the transformation coefficients preserving the hard-core constraint, is

$$\begin{cases} \alpha = \cos\theta \equiv c_\theta, \\ \beta = \sin\theta \equiv s_\theta. \end{cases} \tag{D.11}$$

Our goal is to show that after the transformation (D.9) φ condenses and $\tilde{t}$ fluctuations determine the amplitude (Higgs) mode, while other two components t_x and t_y become transverse Goldstone magnons. The

[1] In general, the coefficients α and β can be taken as arbitrary complex numbers but we choose the most illustrative representation.

simplest way to demonstrate this is to take the quadratic Hamiltonian in the **v**-representation (with $v \equiv v^z$):

$$H^2(v) = \lambda \sum_i n_i + J \sum_{\langle ij \rangle} v_i v_j + K \sum_{\langle ij \rangle_c} v_i v_j. \tag{D.12}$$

We introduce

$$\tilde{T}_i \equiv \varphi_i^\dagger \tilde{t}_i, \qquad \tilde{v}_i \equiv -i(\tilde{T}_i - \tilde{T}_i^\dagger)/2, \qquad \tilde{n}_i = \tilde{t}_i^\dagger \tilde{t}_i,$$
$$c_{2\theta} \equiv \cos 2\theta = \cos^2\theta - \sin^2\theta, \qquad s_{2\theta} \equiv \sin 2\theta = 2\sin\theta\cos\theta.$$

Now step by step we transform all entries of (D.12).

- The number operator

$$n = t^\dagger t = s_\theta^2 \varphi^\dagger \varphi + c_\theta^2 \tilde{t}^\dagger \tilde{t} - ics(\tilde{T} - \tilde{T}^\dagger) = s_\theta^2 + c_{2\theta}\tilde{n} + s_{2\theta}\tilde{v}. \tag{D.13}$$

- The transition operators

$$T = \varphi^\dagger \tilde{t} = ic_\theta s_\theta(\varphi^\dagger\varphi - \tilde{t}^\dagger\tilde{t}) + c_\theta^2\tilde{T} + s_\theta^2\tilde{T}^\dagger = ic_\theta s_\theta(1-2\tilde{n}) + c_\theta^2\tilde{T} + s_\theta^2\tilde{T}^\dagger$$
$$T^\dagger = -ic_\theta s_\theta(1-2\tilde{n}) + c_\theta^2\tilde{T} + s_\theta^2\tilde{T}^\dagger. \tag{D.14}$$

- The dipole and quadrupole moments

$$v = \frac{1}{2i}\big(is_{2\theta}(1-2\tilde{n}) + c_\theta^2(\tilde{T} - \tilde{T}^\dagger) - s_\theta^2(\tilde{T} - \tilde{T}^\dagger)\big) = \frac{1}{2}s_{2\theta}(1-2\tilde{n}) + c_{2\theta}\tilde{v},$$
$$u = \frac{1}{2}(c_\theta^2 + s_\theta^2)(\tilde{T} + \tilde{T}^\dagger) = \tilde{u}. \tag{D.15}$$

- And the product

$$v_i v_j = \Big(\frac{1}{2}s_{2\theta}(1-2\tilde{n}) + c_{2\theta}\tilde{v}\Big)_i \Big(\frac{1}{2}s_{2\theta}(1-2\tilde{n}) + c_{2\theta}\tilde{v}\Big)_j \tag{D.16}$$
$$= \frac{1}{4}s_{2\theta}^2 - \frac{1}{2}s_{2\theta}^2(\tilde{n}_i + \tilde{n}_j) + s_{2\theta}^2\tilde{n}_i\tilde{n}_j + \frac{1}{2}s_{2\theta}c_{2\theta}(\tilde{v}_i + \tilde{v}_j)$$
$$- s_{2\theta}c_{2\theta}(\tilde{n}_i\tilde{v}_j + \tilde{n}_j\tilde{v}_i) + c_{2\theta}^2\tilde{v}_i\tilde{v}_j.$$

We plug in the above expressions into (D.12) and collect all the resulting terms with respect to powers of $\tilde{t}$ (up to the quadratic terms):

$$H^2(v) \simeq H^0(\tilde{v}) + H^1(\tilde{v}) + H^2(\tilde{v}). \tag{D.17}$$

1. The condensate energy per bond ($H^0(\tilde{v})$) reads as

$$\begin{aligned} H^0(\tilde{v}) \equiv E_{\rm cond} &= 2\lambda s_\theta^2 + J\frac{s_{2\theta}^2}{4} + J\frac{s_{2\theta}^2}{4} + (J+K)\frac{s_{2\theta}^2}{4} \\ &= 2\lambda s_\theta^2 + (3J+K)s_\theta^2(1-s_\theta^2), \end{aligned} \tag{D.18}$$

where we used $s_{2\theta}^2 = 4s_\theta^2 c_\theta^2 = 4s_\theta^2(1-s_\theta^2)$. Then this energy per site is given by

$$E_{\rm cond}^{\rm site} = \lambda s_\theta^2 + \frac{1}{2}(3J+K)s_\theta^2(1-s_\theta^2). \tag{D.19}$$

Comparing this energy with the previous classical result (4.10) (with $a_J = 3$ and $a_K = 1$ for the ferromagnetic case), we conclude that

$$s_\theta = \sqrt{\rho}, \qquad c_\theta = \sqrt{1-\rho}. \tag{D.20}$$

Minimization of the condensate energy with respect to ρ yields

$$E'_\rho = 0 \qquad \Rightarrow \qquad \rho = \frac{1}{2}\Big(1 + \frac{1}{\tau}\Big), \tag{D.21}$$

where $\tau = (3J+K)/2\lambda$ and we impose $\tau < 0$ in order to fulfil $\rho \leq 1/2$. For the further steps we provide several simple expressions connecting the trigonometrical functions with ρ and τ:

$$2\rho = 1 + \frac{1}{\tau}, \tag{D.22}$$

$$c_{2\theta} = 1 - 2\rho = -\frac{1}{\tau}, \tag{D.23}$$

$$s_{2\theta}^2 = 4\rho(1-\rho) = 1 - \frac{1}{\tau^2}, \tag{D.24}$$

$$2\lambda\tau = 3J + K, \tag{D.25}$$

$$c_{2\theta} - \tau s_{2\theta}^2 = -\frac{1}{\tau} - \tau\Big(1 - \frac{1}{\tau^2}\Big) = -\frac{1}{\tau} - \tau + \frac{1}{\tau} = -\tau. \quad \text{(D.26)}$$

One can define a chemical potential as well

$$E_{\rm cond} = -\mu\rho, \quad \Rightarrow \quad \mu = -\lambda\Big(1 + \frac{\tau - 1}{2}\Big). \quad \text{(D.27)}$$

2. Linear terms drop out:

$$\begin{aligned} H^1(\tilde{v}) &= \sum_i \lambda s_{2\theta}\tilde{v}_i + \frac{J}{2}\sum_{\langle ij\rangle} s_{2\theta}c_{2\theta}(\tilde{v}_i + \tilde{v}_j) + \frac{K}{2}\sum_{\langle ij\rangle_c} s_{2\theta}c_{2\theta}(\tilde{v}_i + \tilde{v}_j) \\ &= \sum_i \Big[\lambda s_{2\theta} + \frac{3J}{2}s_{2\theta}c_{2\theta} + \frac{K}{2}s_{2\theta}c_{2\theta}\Big]\tilde{v}_i \quad \text{(D.28)} \\ &= \frac{s_{2\theta}}{2}\sum_i \Big[2\lambda + (3J+K)c_{2\theta}\Big]\tilde{v}_i = \frac{s_{2\theta}}{2}\sum_i \Big[2\lambda + 2\lambda\tau\frac{-1}{\tau}\Big]\tilde{v}_i = 0, \end{aligned}$$

where we used expressions (D.23), (D.25) and

$$\sum_{\langle ij\rangle}(\tilde{v}_i + \tilde{v}_j) = \sum_{\gamma=a,b,c}\sum_{\langle ij\rangle\gamma}(\tilde{v}_i + \tilde{v}_j) = 3\sum_i \tilde{v}_i. \quad \text{(D.29)}$$

3. Quadratic terms

$$\begin{aligned} &H^2(\tilde{v}) = \lambda\sum_i c_{2\theta}\tilde{n}_i + J\sum_{\langle ij\rangle}\Big[c_{2\theta}^2\tilde{v}_i^z\tilde{v}_j^z - \frac{s_{2\theta}^2}{2}(\tilde{n}_i + \tilde{n}_j)\Big] \\ &+ K\sum_{\langle ij\rangle_c}\Big[c_{2\theta}^2\tilde{v}_i^z\tilde{v}_j^z - \frac{s_{2\theta}^2}{2}(\tilde{n}_i + \tilde{n}_j)\Big] = \sum_i\Big[\lambda c_{2\theta} - \frac{s_{2\theta}^2}{2}(3J+K)\Big]\tilde{n}_i \\ &+ \frac{J}{\tau^2}\sum_{\langle ij\rangle}\tilde{v}_i^z\tilde{v}_j^z + \frac{K}{\tau^2}\sum_{\langle ij\rangle_c}\tilde{v}_i^z\tilde{v}_j^z = \sum_i\Big[\lambda c_{2\theta} - \lambda\tau s_{2\theta}^2\Big]\tilde{n}_i \quad \text{(D.30)} \\ &+ \frac{J}{\tau^2}\sum_{\langle ij\rangle}\tilde{v}_i^z\tilde{v}_j^z + \frac{K}{\tau^2}\sum_{\langle ij\rangle_c}\tilde{v}_i^z\tilde{v}_j^z = -\lambda\tau\sum_i\tilde{n}_i + \frac{J}{\tau^2}\sum_{\langle ij\rangle}\tilde{v}_i^z\tilde{v}_j^z + \frac{K}{\tau^2}\sum_{\langle ij\rangle_c}\tilde{v}_i^z\tilde{v}_j^z, \end{aligned}$$

where we used expressions (D.23), (D.25), (D.26) and (D.29), substituting $\tilde{v}_{i/j}$ with $\tilde{n}_{i/j}$.

One can see that the transformation (D.9) preserves the form of the quadratic Hamiltonian. Thus, renormalizing coupling constants

$$\tilde{\lambda} = -\lambda\tau, \qquad \tilde{A} = \frac{A}{\tau^2}, \qquad \tilde{J} = \tilde{A}\cos\alpha, \qquad \tilde{K} = \tilde{A}\sin\alpha, \tag{D.31}$$

and reproducing the calculations from Appendix D.1 one obtains the excitation spectra

$$\omega(k) = \sqrt{\tilde{\lambda}^2 \pm 2\tilde{\lambda}|\tilde{\gamma}_k(\alpha)|} = \lambda\sqrt{\tau^2 \pm |\phi(k,\alpha)|}, \tag{D.32}$$

where

$$\tilde{\gamma}_k(\alpha) = \frac{3\tilde{A}}{4}\phi(k,\alpha), \tag{D.33}$$

$$\phi(k,\alpha) = \frac{1}{3}(e^{-ik_a} + e^{-ik_b} + e^{-ik_c})\cos\alpha + \frac{1}{3}e^{-ik_c}\sin\alpha, \qquad |\phi(k,\alpha)| \leq 1$$

We provide the simplest example revealing this mechanism – the pure Heisenberg regime $\alpha = 180°$. According to (D.19) and (D.21) one gets $\tau = -3J/2\lambda$ and

$$\omega_z(k) = \sqrt{\tilde{\lambda}^2 \pm \tilde{\lambda}\frac{3\tilde{J}}{2}|\phi_k|} = \sqrt{\lambda^2\tau^2 \pm \lambda\tau\frac{3J|\phi_k|}{2\tau^2}} = \lambda\sqrt{\tau^2 \pm |\phi_k|}, \tag{D.34}$$

where we used $3J/2\tau = \lambda$. This result reproduces that of [20]. One can easily see that the dispersion (D.32) is gapped with the gap $\Delta = \sqrt{\tau^2 - 1}$, which represents *the amplitude Higgs mode* (5.19).

The remaining two components get the chemical energy shift $-\mu$, while their hoppings acquire a prefactor $1 - \rho$, i.e. $v_{x/y} \to \varphi\, v_{x/y} = \sqrt{1-\rho}\, v_{x/y}$. Therefore, for the x-component one finds

$$H_{ij}^{\gamma,x} = \tilde{\lambda}_x\tilde{n}_x + \tilde{J}_x v_{i,x}v_{j,x} + \tilde{K}_x v_{i,x}^{\gamma}v_{j,x}^{\gamma} \tag{D.35}$$

$$\text{with} \qquad \tilde{\lambda}_x = \lambda + \mu = \frac{1-\tau}{2}, \qquad \tilde{J}_x = J\frac{\tau - 1}{2\tau}.$$

The x-boson dispersion reads as

$$\begin{aligned}\omega_x(k) &= \sqrt{\lambda^2\Big(\frac{1-\tau}{2}\Big)^2 \pm \lambda\Big(\frac{1-\tau}{2}\Big)\Big(\frac{\tau-1}{2}\Big)\Big(\frac{A}{\tau}\Big)|\phi_k|} \\ &= \lambda\Big|\frac{1-\tau}{2}\Big|\sqrt{1\pm|\phi_k|},\end{aligned} \tag{D.36}$$

which corresponds to a gapless Goldstone magnon mode (5.20).

E

Simplifications made in Chapter 7

E.1 On the pair terms contribution

Preserving pair terms yields the Hamiltonian

$$
\begin{aligned}
H = \lambda \sum_i \{ & n_i^x + n_i^y + n_i^z + \tilde{n}_i^x + \tilde{n}_i^y + \tilde{n}_i^z \} \qquad \text{(E.1)} \\
& + J \sum_{\langle ij \rangle} \{ x_i^\dagger \tilde{x}_j + y_i^\dagger \tilde{y}_j + z_i^\dagger \tilde{z}_j - x_i^\dagger \tilde{x}_j^\dagger - y_i^\dagger \tilde{y}_j^\dagger - z_i^\dagger \tilde{z}_j^\dagger + \text{h.c.} \} \\
& + K \Big[\sum_{\langle ij \rangle a} \{ x_i^\dagger \tilde{x}_j - x_i^\dagger \tilde{x}_j^\dagger \} + \sum_{\langle ij \rangle b} \{ y_i^\dagger \tilde{y}_j - y_i^\dagger \tilde{y}_j^\dagger \} + \sum_{\langle ij \rangle c} \{ z_i^\dagger \tilde{z}_j - z_i^\dagger \tilde{z}_j^\dagger \} + \text{h.c.} \Big] \\
& + \Gamma \Big[\sum_{\langle ij \rangle a} \{ y_i^\dagger \tilde{z}_j + z_i^\dagger \tilde{y}_j \} + \sum_{\langle ij \rangle a} \{ y_i^\dagger \tilde{z}_j + z_i^\dagger \tilde{y}_j \} + \sum_{\langle ij \rangle a} \{ y_i^\dagger \tilde{z}_j + z_i^\dagger \tilde{y}_j \} + \text{h.c.} \Big] \\
& - \Gamma \Big[\sum_{\langle ij \rangle a} \{ y_i^\dagger \tilde{z}_j^\dagger + z_i^\dagger \tilde{y}_j^\dagger \} + \sum_{\langle ij \rangle a} \{ y_i^\dagger \tilde{z}_j^\dagger + z_i^\dagger \tilde{y}_j^\dagger \} + \sum_{\langle ij \rangle a} \{ y_i^\dagger \tilde{z}_j^\dagger + z_i^\dagger \tilde{y}_j^\dagger \} + \text{h.c.} \Big] \\
& + g \mu_B \frac{i}{2} \sum_i \Big[\tilde{h}_x (y_i^\dagger z_i - z_i^\dagger y_i + \tilde{y}_i^\dagger \tilde{z}_i - \tilde{z}_i^\dagger \tilde{y}_i) + \tilde{h}_y (z_i^\dagger x_i - x_i^\dagger z_i + \tilde{z}_i^\dagger \tilde{x}_i - \tilde{x}_i^\dagger \tilde{z}_i) \\
& + \tilde{h}_z (x_i^\dagger y_i - y_i^\dagger x_i + \tilde{x}_i^\dagger \tilde{y}_i - \tilde{y}_i^\dagger \tilde{x}_i) \Big].
\end{aligned}
$$

Extending the Bogolyubov transformation (D.4) up to 12 components, we end up with a system of 12 equations and construct the corresponding P-matrix (D.8)

$$P(\mathbf{k}) = \begin{pmatrix} A & B(\mathbf{k}) & \mathcal{O} & B(\mathbf{k})^\dagger \\ B(\mathbf{k})^\dagger & A & B(\mathbf{k})^\dagger & \mathcal{O} \\ \mathcal{O} & -B(\mathbf{k}) & -A & -B(\mathbf{k})^\dagger \\ -B(\mathbf{k}) & \mathcal{O} & -B(\mathbf{k}) & -A \end{pmatrix} \tag{E.2}$$

where $\mathcal{O}$ refers to a 3×3 zero matrix and

$$A = \begin{pmatrix} \lambda & -ih_z & ih_y \\ ih_z & \lambda & -ih_x \\ -ih_y & ih_x & \lambda \end{pmatrix}, \tag{E.3}$$

$$B(\mathbf{k}) = \begin{pmatrix} J\gamma + Ke^{ik_a} & \Gamma & \Gamma e^{ik_b} \\ \Gamma & J\gamma + Ke^{ik_b} & \Gamma e^{ik_a} \\ \Gamma e^{ik_b} & \Gamma e^{ik_a} & J\gamma + K \end{pmatrix}.$$

Using the ZGEEVX LAPACK routine and calculating 12 corresponding Chern numbers one proves the assumption that for $\lambda \gg 1$ pair terms $T^\dagger_{\gamma,i} T^\dagger_{\gamma,j}$ do not affect the results, given in Chapter 7.

E.2 Terms linear in triplons

We consider the generalized projection of the magnetic moment operator (3.29) onto the low-energy subspace:

$$\mathbf{M}_j = i\alpha(\mathbf{T}_j - \mathbf{T}_j^\dagger) + i\beta(\mathbf{T}^\dagger \times \mathbf{T})_j, \tag{E.4}$$

and in terms of $(s, \mathbf{t})$ operators for the on-site part of the Hamiltonian we find (for the magnetic field $h \parallel (1,1,1)$)

$$H = \sum_j \Big[\lambda n_j^t + \mathbf{h}\cdot\mathbf{M}_j\Big] \tag{E.5}$$

$$\begin{aligned}
=&\sum_j \Big\{\lambda(t_x^\dagger t_x + t_y^\dagger t_y + t_z^\dagger t_z)_j + i\alpha h(T_x - T_x^\dagger)_j + i\alpha h(T_y - T_y^\dagger)_j + i\alpha h(T_z - T_z^\dagger)_j \\
&+ i\beta h(T_y^\dagger T_z - T_z^\dagger T_y)_j + i\beta h(T_z^\dagger T_x - T_x^\dagger T_z)_j + i\beta h(T_x^\dagger T_y - T_y^\dagger T_x)_j\Big\} \\
=&\sum_j \Big\{\lambda(t_x^\dagger t_x + t_y^\dagger t_y + t_z^\dagger t_z)_j + i\alpha h(s^\dagger t_x - t_x^\dagger s)_j + i\alpha h(s^\dagger t_y - t_y^\dagger s)_j \\
&+ i\alpha h(s^\dagger t_z - t_z^\dagger s)_j + i\beta h(t_y^\dagger t_z - t_z^\dagger t_y)_j + i\beta h(t_z^\dagger t_x - t_x^\dagger t_z)_j + i\beta h(t_x^\dagger t_y - t_y^\dagger t_x)_j\Big\} \\
=&\sum_j \begin{pmatrix} s^\dagger & t_x^\dagger & t_y^\dagger & t_z^\dagger \end{pmatrix}_j \begin{pmatrix} 0 & i\alpha h & i\alpha h & i\alpha h \\ -i\alpha h & \lambda & i\beta h & -i\beta h \\ -i\alpha h & -i\beta h & \lambda & i\beta h \\ -i\alpha h & i\beta h & -i\beta h & \lambda \end{pmatrix} \begin{pmatrix} s \\ t_x \\ t_y \\ t_z \end{pmatrix}_j,
\end{aligned}$$

where we used $T_{\gamma,j}^\dagger T_{\gamma,j} = t_{\gamma,j}^\dagger t_{\gamma,j}$. The eigenvalues of this matrix provide energy corrections

$$\epsilon_{1,2} = \lambda \pm \beta\sqrt{3}\, h, \tag{E.6}$$

$$\epsilon_{3,4} = \frac{\lambda}{2}\Big(1 \pm \sqrt{1 + \frac{12\alpha^2 h^2}{\lambda^2}}\,\Big). \tag{E.7}$$

Therefore, the linear terms enter $\sim 1/\lambda$. We take some typical values used in our simulations (ignoring units), for example $\lambda = 50$, $\alpha = -\sqrt{6}$, $\beta = -1/2$, $\mathbf{h} = (0.2, 0.2, 0.2)$, and get

$$\epsilon_{1,2} = 50 \pm \frac{\sqrt{3}}{2}\cdot 0.2 \simeq 50 \pm 0.173$$

$$\epsilon_{3,4} = 25\Big(1 \pm \sqrt{1 + \frac{12\cdot 6\cdot 0.04}{2500}}\,\Big) \simeq 25(1 \pm 1.0006)$$

The first two corrections are ca. $0,4\%$ of λ, whereas the linear terms contribution is 0.03%.

F

On the real units in our simulations

We consider the thermal Hall conductivity

$$\kappa^{xy} = -\frac{k_B^2 T}{(2\pi)^2 \hbar} \sum_n \int_{BZ} c_2[\rho_i] \Omega_i^z(\mathbf{k}) d^2k \equiv -\frac{\xi(T)}{(2\pi)^2} \sum_n \int_{BZ} c_2[\rho_i] \Omega_i^z(\mathbf{k}) d^2k, \tag{F.1}$$

where

$$\begin{aligned} &k_{\mathrm{B}} \simeq 8.617 \cdot 10^{-5} \ \frac{\mathrm{eV}}{\mathrm{K}} = 8.617 \cdot 10^{-2} \ \frac{\mathrm{meV}}{\mathrm{K}}, \\ &\hbar \simeq 6.582 \cdot 10^{-16} \, \mathrm{eV} \cdot \mathrm{s} = 6.582 \cdot 10^{-13} \, \mathrm{meV} \cdot \mathrm{s}, \\ &1 \, \mathrm{meV} \simeq 1.602 \cdot 10^{-22} \ \mathrm{W} \cdot s. \end{aligned}$$

Therefore, $\xi(T)$ becomes (with units written explicitly)

$$\xi(T) = T \, \mathrm{K} \frac{(8.617)^2 \cdot 10^{-4} \ \mathrm{meV}^2}{\mathrm{K}^2 \cdot 6.582 \cdot 10^{-13} \ \mathrm{meV} \cdot \mathrm{s}} = T \cdot \frac{(8.617)^2}{6.582} \cdot 10^9 \ \frac{\mathrm{meV}}{\mathrm{K} \cdot \mathrm{s}} \tag{F.2}$$

$$= T \cdot \frac{(8.617)^2}{6.582} \cdot 1.602 \cdot 10^{-13} \ \frac{\mathrm{W}}{\mathrm{K}} \simeq T \cdot 1.807 \cdot 10^{-12} \ \frac{\mathrm{W}}{\mathrm{K}}. \tag{F.3}$$

The conductivity κ^{xy} is often expressed in W/Km. Dividing by the standard interionic lattice scale Å one obtains

$$\xi(T) \simeq T \cdot 1.807 \cdot 10^{-12} \cdot 10^{10} \ \frac{\mathrm{W}}{\mathrm{Km}} = T \cdot 0.018 \ \frac{\mathrm{W}}{\mathrm{Km}}. \tag{F.4}$$

One can express the couplings λ, J, K, Γ in meV and calculate the thermal conductivity according to (F.1). In order to get the W/Km units, this result should be multiplied by (F.4) for the given temperature T.

Now we provide estimations for the couplings using the data from [20], namely $\lambda \sim 50-200\,\mathrm{meV}$, $4t^2/U \sim 50-100\,\mathrm{meV}$. Introducing $\eta = t/t'$, we have

$$J = \frac{1}{4}J_v = \frac{1}{4}\Big(\frac{3t^2}{U} + \frac{2t'^2}{3U}\Big) = \frac{1}{16}\Big(3 + \frac{2}{3\eta^2}\Big)\frac{4t^2}{U}, \tag{F.5}$$

$$K = \frac{1}{4}K_v = \frac{1}{4}\Big(-\frac{3t^2}{U} + \frac{2t'^2}{U}\Big) = \frac{1}{16}\Big(-3 + \frac{2}{\eta^2}\Big)\frac{4t^2}{U}, \tag{F.6}$$

$$\Gamma = \frac{1}{4}\Gamma_v = \frac{1}{16\eta}\frac{4t^2}{U}. \tag{F.7}$$

The magnetic field enters the Hamiltonian as follows

$$H_{\mathrm{mag}} = -g\mu_B \mathbf{h} \sum_i \mathbf{M}_i, \tag{F.8}$$

with

$$\mu_{\mathrm{B}} \simeq 5.788 \cdot 10^{-5}\ \frac{\mathrm{eV}}{\mathrm{T}} = 5.788 \cdot 10^{-2}\ \frac{\mathrm{meV}}{\mathrm{T}}. \tag{F.9}$$

With $g = 1/2$ the magnetic field of the magnitude 1 T corresponds to ~ 0.03.

If we define $4t^2/U \simeq 50$ meV then the couplings read as (in meV)

$$\frac{t'}{t} = 0, \qquad J = 9.375, \qquad K = -9.375, \qquad \Gamma = 0, \tag{F.10}$$

$$\frac{t'}{t} = 0.1, \qquad J = 9.396, \qquad K = -9.313, \qquad \Gamma = 0.313, \tag{F.11}$$

$$\frac{t'}{t} = 0.2, \qquad J = 9.458, \qquad K = -9.125, \qquad \Gamma = 0.625, \tag{F.12}$$

$$\frac{t'}{t} = 0.3, \qquad J = 9.606, \qquad K = -8.681, \qquad \Gamma = 1.042, \tag{F.13}$$

$$\frac{t'}{t} = 1, \qquad J = 11.458, \qquad K = -3.125, \qquad \Gamma = 3.125. \tag{F.14}$$

Bibliography

[1] N. F. Mott, Proceedings of the Physical Society. Section A **62**, 416 (1949).

[2] G. Khaliullin, Physical Review B **64**, 212405 (2001).

[3] G. Khaliullin, Progress of Theoretical Physics Supplement **160**, 155 (2005).

[4] G. Jackeli and G. Khaliullin, Physical Review Letters **102**, 017205 (2009).

[5] J. Chaloupka, G. Jackeli, and G. Khaliullin, Physical Review Letters **105**, 027204 (2010).

[6] H.-C. Jiang, Z.-C. Gu, X.-L. Qi, and S. Trebst, Physical Review B **83**, 245104 (2011).

[7] J. Reuther, R. Thomale, and S. Trebst, Physical Review B **84**, 100406(R) (2011).

[8] F. Trousselet, G. Khaliullin, and P. Horsch, Physical Review B **84**, 054409 (2011).

[9] R. Schaffer, S. Bhattacharjee, and Y. B. Kim, Physical Review B **86**, 224417 (2012).

[10] C. C. Price and N. B. Perkins, Physical Review Letters **109**, 187201 (2012).

[11] C. Price and N. B. Perkins, Physical Review B **88**, 024410 (2013).

[12] J. Chaloupka, G. Jackeli, and G. Khaliullin, Physical Review Letters **110**, 097204 (2013).

[13] S. Okamoto, Physical Review B **87**, 064508 (2013).

[14] F. Trousselet, P. Horsch, A. M. Oleś, and W.-L. You, Physical Review B **90**, 024404 (2014).

[15] J. G. Rau, E. K.-H. Lee, and H.-Y. Kee, Physical Review Letters **112**, 077204 (2014).

[16] J. G. Rau and H.-Y. Kee, arXiv:1408.4811 (2014).

[17] J. Chaloupka and G. Khaliullin, Physical Review B **92**, 024413 (2015).

[18] J. Chaloupka and G. Khaliullin, Physical Review B **94**, 064435 (2016).

[19] M. Gohlke, R. Verresen, R. Moessner, and F. Pollmann, Physical Review Letters **119**, 157203 (2017).

[20] G. Khaliullin, Physical Review Letters **111**, 197201 (2013).

[21] A. Akbari and G. Khaliullin, Physical Review B **90**, 035137 (2014).

[22] S. Nakatsuji, S. ichi Ikeda, and Y. Maeno, Journal of the Physical Society of Japan **66, 1868** (1997), 10.1143/jpsj.66.1868.

[23] T. Mizokawa, L. H. Tjeng, G. A. Sawatzky, G. Ghiringhelli, O. Tjernberg, N. B. Brookes, H. Fukazawa, S. Nakatsuji, and Y. Maeno, Physical Review Letters **87**, 077202 (2001).

[24] M. Braden, G. André, S. Nakatsuji, and Y. Maeno, Physical Review B **58, 847** (1998), 10.1103/physrevb.58.847.

[25] Y. Singh and P. Gegenwart, Physical Review B **82**, 064412 (2010).

[26] X. Liu, T. Berlijn, W.-G. Yin, W. Ku, A. Tsvelik, Y.-J. Kim, H. Gretarsson, Y. Singh, P. Gegenwart, and J. P. Hill, Physical Review B **83**, 220403(R) (2011).

[27] Y. Singh, S. Manni, J. Reuther, T. Berlijn, R. Thomale, W. Ku, S. Trebst, and P. Gegenwart, Physical Review Letters **108**, 127203 (2012).

[28] R. Comin, G. Levy, B. Ludbrook, Z.-H. Zhu, C. N. Veenstra, J. A. Rosen, Y. Singh, P. Gegenwart, D. Stricker, J. N. Hancock, D. van der Marel, I. S. Elfimov, and A. Damascelli, Physical Review Letters **109**, 266406 (2012).

[29] H. Gretarsson, J. P. Clancy, X. Liu, J. P. Hill, E. Bozin, Y. Singh, S. Manni, P. Gegenwart, J. Kim, A. H. Said, D. Casa, T. Gog, M. H. Upton, H.-S. Kim, J. Yu, V. M. Katukuri, L. Hozoi, J. van den Brink, and Y.-J. Kim, Physical Review Letters **110**, 076402 (2013).

[30] J. P. Clancy, N. Chen, C. Y. Kim, W. F. Chen, K. W. Plumb, B. C. Jeon, T. W. Noh, and Y.-J. Kim, Physical Review B **86, 195131** (2012), 10.1103/physrevb.86.195131.

[31] F. Ye, S. Chi, H. Cao, B. C. Chakoumakos, J. A. Fernandez-Baca, R. Custelcean, T. F. Qi, O. B. Korneta, and G. Cao, Physical Review B **85**, 180403(R) (2012).

[32] S. K. Choi, R. Coldea, A. N. Kolmogorov, T. Lancaster, I. I. Mazin, S. J. Blundell, P. G. Radaelli, Y. Singh, P. Gegenwart, K. R. Choi, S.-W. Cheong, P. J. Baker, C. Stock, and J. Taylor, Physical Review Letters **108**, 127204 (2012).

[33] H. Gretarsson, J. P. Clancy, Y. Singh, P. Gegenwart, J. P. Hill, J. Kim, M. H. Upton, A. H. Said, D. Casa, T. Gog, and Y.-J. Kim, Physical Review B **87**, 220407 (2013).

[34] A. Jain, M. Krautloher, J. Porras, G. H. Ryu, D. P. Chen, D. L. Abernathy, J. T. Park, A. Ivanov, J. Chaloupka, G. Khaliullin, B. Keimer, and B. J. Kim, Nature Physics **13, 633** (2017), 10.1038/nphys4077.

[35] A. Kitaev, Annals of Physics **321**, 2 (2006).

[36] A. Kitaev, Annals of Physics **303**, 2 (2003).

[37] S. M. Winter, A. A. Tsirlin, M. Daghofer, J. van den Brink, Y. Singh, P. Gegenwart, and R. Valentí, Journal of Physics: Condensed Matter **29**, 493002 (2017).

[38] J. c. v. Chaloupka and G. Khaliullin, Phys. Rev. Lett. **116**, 017203 (2016).

[39] N. F. Mott, Philosophical Magazine **6**, 287 (1961).

[40] R. Knox, Solid State Phys. Suppl **5, 100** (1963).

[41] D. Jérome, T. M. Rice, and W. Kohn, Physical Review **158**, 462 (1967).

[42] B. I. Halperin and T. M. Rice, Reviews of Modern Physics **40**, 755 (1968).

[43] A. V. Chubukov and D. K. Morr, Physical Review B **52**, 3521 (1995).

[44] B. Normand and T. M. Rice, Physical Review B **56**, 8760 (1997).

[45] M. Vojta and K. W. Becker, Physical Review B **60**, 15201 (1999).

[46] L. Balents, Physical Review B **62**, 2346 (2000).

[47] C. D. Batista, Physical Review Letters **89**, 166403 (2002).

[48] S. Mase and T. Sakai, Journal of the Physical Society of Japan **31**, 730 (1971).

[49] H. Fukuyama and T. Nagai, Journal of the Physical Society of Japan **31**, 812 (1971).

[50] Y. Kuramoto and M. Morimoto, Journal of the Physical Society of Japan **44**, 1759 (1978).

[51] J. Kuneš, Journal of Physics: Condensed Matter **27**, 333201 (2015).

[52] W. Witczak-Krempa, G. Chen, Y. B. Kim, and L. Balents, Annual Review of Condensed Matter Physics **5**, 57 (2014).

[53] D. Pekker and C. Varma, Annual Review of Condensed Matter Physics **6**, 269 (2015).

[54] S. Raghu and F. D. M. Haldane, Physical Review A **78** (2008), 10.1103/physreva.78.033834.

[55] A. Petrescu, A. A. Houck, and K. L. Hur, Physical Review A **86** (2012), 10.1103/physreva.86.053804.

[56] M. C. Rechtsman, J. M. Zeuner, Y. Plotnik, Y. Lumer, D. Podolsky, F. Dreisow, S. Nolte, M. Segev, and A. Szameit, Nature **496**, 196 (2013).

[57] M. Hafezi, S. Mittal, J. Fan, A. Migdall, and J. M. Taylor, Nature Photonics **7**, 1001 (2013).

[58] X. Zhou, X. Ling, Z. Zhang, H. Luo, and S. Wen, Scientific Reports **4** (2014), 10.1038/srep07388.

[59] P. Ben-Abdallah, Physical Review Letters **116** (2016), 10.1103/physrevlett.116.084301.

[60] D. Jahani, A. A. Ghatar, L. Abaspour, and T. Jahani, Journal of Applied Physics **124**, 043104 (2018).

[61] L. Zhang, J. Ren, J.-S. Wang, and B. Li, Physical Review Letters **105** (2010), 10.1103/physrevlett.105.225901.

[62] L. Zhang, J. Ren, J.-S. Wang, and B. Li, Journal of Physics: Condensed Matter **23**, 305402 (2011).

[63] T. Qin, J. Zhou, and J. Shi, Physical Review B **86** (2012), 10.1103/physrevb.86.104305.

[64] Y. Onose, T. Ideue, H. Katsura, Y. Shiomi, N. Nagaosa, and Y. Tokura, Science **329**, 297 (2010).

[65] T. Ideue, Y. Onose, H. Katsura, Y. Shiomi, S. Ishiwata, N. Nagaosa, and Y. Tokura, Physical Review B **85** (2012), 10.1103/physrevb.85.134411.

[66] P. Laurell and G. A. Fiete, Physical Review Letters **118** (2017), 10.1103/physrevlett.118.177201.

[67] H. Katsura, N. Nagaosa, and P. A. Lee, Physical Review Letters **104** (2010), 10.1103/physrevlett.104.066403.

[68] T. Ideue, Y. Onose, H. Katsura, Y. Shiomi, S. Ishiwata, N. Nagaosa, and Y. Tokura, Physical Review B **85** (2012), 10.1103/physrevb.85.134411.

[69] A. Mook, J. Henk, and I. Mertig, Physical Review B **89** (2014), 10.1103/physrevb.89.134409.

[70] R. Chisnell, J. Helton, D. Freedman, D. Singh, R. Bewley, D. Nocera, and Y. Lee, Physical Review Letters **115** (2015), 10.1103/physrevlett.115.147201.

[71] M. Hirschberger, R. Chisnell, Y. S. Lee, and N. Ong, Physical Review Letters **115** (2015), 10.1103/physrevlett.115.106603.

[72] H. Lee, J. H. Han, and P. A. Lee, Physical Review B **91** (2015), 10.1103/physrevb.91.125413.

[73] S. A. Owerre, Physical Review B **95** (2017), 10.1103/physrevb.95.014422.

[74] S. A. Owerre, EPL (Europhysics Letters) **117**, 37006 (2017).

[75] S. A. Owerre, Journal of Physics Communications **1**, 021001 (2017).

[76] P. Laurell and G. A. Fiete, http://arxiv.org/abs/1804.09783v1 .

[77] S. A. Owerre, Journal of Physics: Condensed Matter **28**, 47LT02 (2016).

[78] S. A. Owerre, Journal of Physics: Condensed Matter **28**, 386001 (2016).

[79] S. A. Owerre, Physical Review B **94**, 094405 (2016).

[80] S. A. Owerre, Journal of Physics: Condensed Matter **29**, 03LT01 (2016).

[81] S. A. Owerre, Journal of Applied Physics **120**, 043903 (2016).

[82] S. A. Owerre, Journal of Physics Communications **1**, 021002 (2017).

[83] S. A. Owerre, Journal of Physics Communications **1**, 025007 (2017).

[84] S. A. Owerre and J. Nsofini, Journal of Physics: Condensed Matter **29**, 455802 (2017).

[85] S. A. Owerre, Journal of Applied Physics **121**, 223904 (2017).

[86] S. A. Owerre, arXiv:1802.04268 .

[87] D. G. Joshi, Physical Review B **98** (2018), 10.1103/physrevb.98.060405.

[88] J. Romhányi, K. Penc, and R. Ganesh, Nature Communications **6** (2015), 10.1038/ncomms7805.

[89] M. Malki and K. P. Schmidt, Physical Review B **95** (2017), 10.1103/physrevb.95.195137.

[90] P. A. McClarty, F. Krüger, T. Guidi, S. F. Parker, K. Refson, A. W. Parker, D. Prabhakaran, and R. Coldea, Nature Physics **13**, 736 (2017).

[91] B. S. Shastry and B. Sutherland, Physica B+C **108**, 1069 (1981).

[92] I. Dzyaloshinsky, Journal of Physics and Chemistry of Solids **4**, 241 (1958).

[93] T. Moriya, Physical Review **120**, 91 (1960).

[94] S. Murakami and A. Okamoto, Journal of the Physical Society of Japan **86**, 011010 (2017).

[95] G. Sundaram and Q. Niu, Physical Review B **59**, 14915 (1999).

[96] I. B. Bersuker, *Structure and Properties of Transition Metal Compounds: Introduction to the Theory* (Nauka, 1971).

[97] A. Zvezdin, V. M. Matveev, A. Mukhin, and A. I. Popov, *Moscow Izdatel Nauka*, Vol. -1 (Nauka, 1985).

[98] S. A. Al'tshuler and B. M. Kozyrev, *Electron Paramagnetic Resonance* (Elsevier Science, 2013).

[99] B. A. Averill, *Chemistry: Principles, Patterns, and Applications with Student Access Kit for Mastering General Chemistry* (Prentice Hall, 2007).

[100] D. I. Khomskii, *Transition Metal Compounds* (Cambridge University Press, 2009).

[101] C. J. Bradley and A. Cracknell, *The Mathematical Theory of Symmetry in Solids: Representation Theory for Point Groups and Space Groups* (Oxford Univer Pr, 2010).

[102] A. Abragam and B. Bleaney, *Electron Paramagnetic Resonance of Transition Ions* (Oxford Univer Pr, 2012).

[103] F. H. L. Essler, H. Frahm, F. Göhmann, A. Klümper, and V. E. Korepin, *The One-Dimensional Hubbard Model* (Cambridge University Press, 2005).

[104] P. A. Lee, N. Nagaosa, and X.-G. Wen, Reviews of Modern Physics **78**, 17 (2006).

[105] J. Hubbard, Proceedings of the Royal Society A: Mathematical, Physical and Engineering Sciences **285**, 542 (1965).

[106] J. Hubbard, Proceedings of the Royal Society A: Mathematical, Physical and Engineering Sciences **296**, 82 (1967).

[107] Y. A. Izyumov, Physics-Uspekhi **40**, 445 (1997).

[108] A. Auerbach, *Interacting Electrons and Quantum Magnetism* (Springer New York, 1994).

[109] P. C. Hohenberg, Physical Review **158**, 383 (1967).

[110] A. V. Chubukov, Phys. Rev. B **43**, 3337 (1991).

[111] S. K. Yip, Phys. Rev. Lett. **90**, 250402 (2003).

[112] I. B. Bersuker, *The Jahn-Teller Effect and Vibronic Interactions in Modern Chemistry* (Springer US, 1984).

[113] K. I. Kugel and D. I. Khomskiĭ, Soviet Physics Uspekhi **25**, 231 (1982).

[114] K. Kugel and D. Khomskii, Sov. Phys. Solid State **17**, 285 (1975).

[115] K. Kugel and D. I. Khomskii, Zh. Eksp. Teor. Fiz. **64**, 1429 (1973).

[116] A. M. Oleś, http://arxiv.org/abs/1708.07183v1 .

[117] R. J. Elliott and M. F. Thorpe, Journal of Applied Physics **39**, 802 (1968).

[118] G. Khaliullin, W. Koshibae, and S. Maekawa, Phys. Rev. Lett. **93**, 176401 (2004).

[119] D. Khomskii and G. Sawatzky, Solid State Communications **102**, 87 (1997).

[120] S. V. Streltsov and D. I. Khomskii, Uspekhi Fizicheskih Nauk **187**, 1205 (2017).

[121] L. Balents, Nature **464**, 199 (2010).

[122] L. Savary and L. Balents, Reports on Progress in Physics **80**, 016502 (2016).

[123] P. Anderson, Materials Research Bulletin **8**, 153 (1973).

[124] P. W. Anderson, Science **235**, 1196 (1987).

[125] Z. Nussinov and J. van den Brink, Reviews of Modern Physics **87**, 1 (2015).

[126] S. Weinberg, *The Quantum Theory of Fields* (Cambridge University Press, 2005).

[127] S. Trebst, arXiv:1701.07056 (2017).

[128] I. I. Mazin, H. O. Jeschke, K. Foyevtsova, R. Valentí, and D. I. Khomskii, Physical Review Letters **109**, 197201 (2012).

[129] S. Sugano, *Multiplets of Transition-Metal Ions in Crystals* (Elsevier Science, 2012).

[130] J. C. Slater and G. F. Koster, Phys. Rev. **94**, 1498 (1954).

[131] D. Litvin, Physica **77**, 205 (1974).

[132] L. K. Aminov and M. A. Teplov, Soviet Physics Uspekhi **28**, 762 (1985).

[133] S. Sachdev and R. N. Bhatt, Physical Review B **41**, 9323 (1990).

[134] B. A. Ivanov and A. K. Kolezhuk, Physical Review B **68**, 052401 (2003).

[135] A. Läuchli, F. Mila, and K. Penc, Physical Review Letters **97**, 087205 (2006).

[136] J. Chaloupka and G. Khaliullin, Physical Review Letters **110**, 207205 (2013).

[137] T. Sommer, M. Vojta, and K. Becker, The European Physical Journal B **23, 329** (2001), 10.1007/s100510170052.

[138] M. Matsumoto, B. Normand, T. M. Rice, and M. Sigrist, Physical Review B **69**, 054423 (2004).

[139] T. Giamarchi, C. Rüegg, and O. Tchernyshyov, Nature Physics **4, 198** (2008), 10.1038/nphys893.

[140] S. Kunkemöller, D. Khomskii, P. Steffens, A. Piovano, A. Nugroho, and M. Braden, Physical Review Letters **115**, 247201 (2015).

[141] S. Kunkemöller, E. Komleva, S. V. Streltsov, S. Hoffmann, D. I. Khomskii, P. Steffens, Y. Sidis, K. Schmalzl, and M. Braden, Physical Review B **95**, 214408 (2017).

[142] D. Gotfryd, J. Rusnačko, K. Wohlfeld, G. Jackeli, J. Chaloupka, and A. M. Oleś, Physical Review B **95**, 024426 (2017).

[143] D. Aldous and J. A. Fill, "Reversible Markov Chains and Random Walks on Graphs," (2002), unfinished monograph, recompiled 2014.

[144] S. Chib and E. Greenberg, The American Statistician **49**, 327 (1995), https://www.tandfonline.com/doi/pdf/10.1080/00031305.1995.10476177 .

[145] N. N. Bogolubov, *Introduction to Quantum Statistical Mechanics* (World Scientific Publishing Company, 2009).

[146] S. Pissanetzky, *Sparse Matrix Technology* (Elsevier Science, 2014).

[147] C. Lanczos, Journal of Research of the National Bureau of Standards **45**, 255 (1950).

[148] D. G. Pettifor and D. L. Weaire, eds., *The Recursion Method and Its Applications* (Springer Berlin Heidelberg, 1987).

[149] E. Dagotto, Reviews of Modern Physics **66**, 763 (1994).

[150] J. A. Riera, Physical Review B **43**, 3681 (1991).

[151] D. Poilblanc, Physical Review B **44**, 9562 (1991).

[152] C. Gros, Zeitschrift für Physik B Condensed Matter **86**, 359 (1992).

[153] C. Gros, Physical Review B **53**, 6865 (1996).

[154] M. Thesberg and E. S. Sørensen, Physical Review B **90**, 115117 (2014).

[155] A. Yuste, D. Castells-Graells, and A. Sanpera, arXiv:1806.06542 (2018).

[156] J. Villain, R. Bidaux, J.-P. Carton, and R. Conte, Journal de Physique **41**, 1263 (1980).

[157] K. v. Klitzing, G. Dorda, and M. Pepper, Physical Review Letters **45**, 494 (1980).

[158] D. J. Thouless, M. Kohmoto, M. P. Nightingale, and M. den Nijs, Physical Review Letters **49**, 405 (1982).

[159] M. V. Berry, Proceedings of the Royal Society A: Mathematical, Physical and Engineering Sciences **392**, 45 (1984).

[160] B. A. Bernevig, *Topological Insulators and Topological Superconductors* (Princeton University Press, 2013).

[161] E. J. Weinberg, *Classical Solutions in Quantum Field Theory* (Cambridge University Press, 2012).

[162] G. Giachetta, *Geometric And Algebraic Topological Methods In Quantum Mechanics* (World Scientific Pub Co Inc, 2005).

[163] R. Matsumoto and S. Murakami, Physical Review Letters **106** (2011), 10.1103/physrevlett.106.197202.

[164] R. Matsumoto and S. Murakami, Physical Review B **84** (2011), 10.1103/physrevb.84.184406.

[165] R. Morris, Mathematics of Computation **33**, 778 (1979).

[166] G. E. Volovik, *The Universe in a Helium Droplet* (Oxford University Press, 2009).

[167] Y. Hatsugai, Phys. Rev. Lett. **71**, 3697 (1993).

[168] K. Nawa, K. Tanaka, N. Kurita, T. J. Sato, H. Sugiyama, H. Uekusa, S. Ohira-Kawamura, K. Nakajima, and H. Tanaka, arXiv:1810.08931 .

[169] D. G. Joshi, A. P. Schnyder, and S. Takei, Physical Review B **98** (2018), 10.1103/physrevb.98.064401.

[170] G. van Miert, C. Ortix, and C. M. Smith, 2D Materials **4**, 015023 (2017).

[171] A. Rüegg, J. Wen, and G. A. Fiete, Phys. Rev. B **81**, 205115 (2010).

[172] F. Aust, "Personal Communication," .

[173] R. M. White, *Quantum Theory of Magnetism* (Springer Berlin Heidelberg, 2007).

Danksagung

Mein besonderer Dank gilt meiner Betreuerin und Hauptberichterin Frau Prof. Dr. Daghofer dafür, dass sie mir die Promotion ermöglicht hat und mich stets in allem unterstützt und begleitet hat.

Darüber hinaus möchte ich Friedemann Aust meinen Dank aussprechen: für seinen Eifer an der Forschung, seine Einsatzbereitschaft und ständige Mithilfe.

Ich danke Teresa Feldmaier, die mir bei den Erledigungen meiner sprachlichen Angelegenheiten viel geholfen hat.

Die letzten vier Jahre waren reich an guten Ereignissen und Veränderungen. Für die Unterstützung in diesen turbulenten Zeiten möchte ich mich bei allen Kollegen des FMQ bedanken.

От чистого сердца хочу поблагодарить всех моих близких. Посредством этой работы закрывается одна из важнейших вех в моей жизни. Оттого и отсылаю я не к минувшим четырём годам, но к куда более обширной временной перспективе.

Спасибо моим Родителям за детство, которое было счастливым, невзирая на окружающий хаос тех лет, за прекрасное образование, что дало мне возможность провести вышеизложенные научные изыскания, написать квалификационную работу и получить учёную степень. Балашовым, которые всю мою жизнь были рядом, сопутствовали во всех начинаниях и всячески поддерживали; в особенности я признателен Саше Балашову, чей пытливый ум и твёрдый характер всегда служили для меня примером. Полагаю, нечто подобное испытывает и Лёша, тем самым стимулируя меня „держать планку“, за что тебе, Алексей, отдельное спасибо.

Я безгранично благодарен своей супруге Алёне; ты была и остаёшься рядом, на тебя я могу рассчитывать всегда и во всём. Спасибо и твоим родителям за всю оказанную нам помощь, особенно во время поиска данной позиции.

Спасибо друзьям, которые сквозь года и расстояния остаются со мной. Оказанное вами на меня влияние трудно переоценить, а столь необходимую взаимовыручку и полезные советы невозможно не упомянуть. Ваши дружеские напутствия не дают мне падать духом и мотивируют к дальнейшим свершениям. Особую благодарность выражаю Левону и Алисе за выявление многочисленных ошибок в написанных мной английских текстах.

Отдельное спасибо Саше Киселеву, который на протяжении всего моего пребывания в Германии многократно выручал меня из, казалось бы, безвыходных ситуаций.

Спасибо Гинияту Халиуллину за тёплые и исчерпывающе полные консультации, без которых представленные в данной работе результаты навряд ли увидели бы свет.

Помимо всего прочего, я благодарю мироздание за предоставленые загадки и тайны, что не прекращают будоражить фантазию и побуждают к движению вперёд.

Спасибо!

Ehrenwörtliche Erklärung

Ich erkläre, dass ich diese Dissertation, abgesehen von den ausdrücklich bezeichneten Hilfsmitteln, selbständig verfasst habe.

Stuttgart, den 1. Februar 2019 *Pavel Anisimov*